Models of Tsunamigenic Earthquake Rupture Along the West Coast of North America

By

Matthew Sypus
B.Sc., University of Victoria, 2016

A Thesis Submitted in Partial Fulfillment
of the Requirements for the Degree of

MASTER OF SCIENCE

in the School of Earth and Ocean Sciences

Supervisory Committee

Models of Tsunamigenic Earthquake Rupture Along the West Coast of North America

By

Matthew Sypus
B.Sc., University of Victoria, 2016

Supervisory Committee

Dr. Kelin Wang (School of Earth and Ocean Sciences)
Co-Supervisor

Dr. Stan Dosso (School of Earth and Ocean Sciences)
Co-Supervisor

Dr. Edwin Nissen (School of Earth and Ocean Sciences)
Departmental Member

Abstract

Supervisory Committee
Dr. Kelin Wang (School of Earth and Ocean Sciences)
Co-Supervisor
Dr. Stan Dosso (School of Earth and Ocean Sciences)
Co-Supervisor
Dr. Edwin Nissen (School of Earth and Ocean Sciences)
Departmental Member

The west coast of North America faces the risk of tsunamis generated by seismic rupture in three regions, namely, the Cascadia subduction zone extending from southwestern British Columbia to northern California, the southern Queen Charlotte margin in the Haida Gwaii area, and the Winona Basin just northeast of Vancouver Island. In this thesis, I construct tsunamigenic rupture models with a 3-D elastic half-space dislocation model for these three regions. The tsunami risk is the highest along the Cascadia coast, and many tsunami source models have been developed and used in the past. In efforts to improve the Cascadia tsunami hazard assessment, I use an updated Cascadia fault geometry to create 9 tsunami source models which include buried, splay-faulting, and trench-breaching rupture. Incorporated in these scenarios is a newly-proposed splay fault based on minor evidence found in seismic reflection images off Vancouver Island. To better understand potential rupture boundaries of the Cascadia megathrust rupture, I also model deformation caused by the 1700 C.E. great Cascadia earthquake that fit updated microfossil-based paleoseismic coastal subsidence estimates. These estimates validate the well-accepted along-strike heterogenic rupture of the 1700 earthquake but suggest greater variations in subsidence along the coast. It is recognized that the Winona Basin area just north of the Cascadia subduction zone may have the potential to host a tsunamigenic thrust earthquake, but it has not been formally included in tsunami hazard assessments. There is a high degree of uncertainty in the tectonics of the area, the presence of a subduction “megathrust”, fault geometry, and rupture

boundaries. Assuming worst-case scenarios and considering the uncertainties, I construct a fault geometry using seismic images and generate six tsunami sources with buried and trench-breaching rupture in which downdip rupture extent is varied. The *Mw* 7.8 2012 Haida Gwaii earthquake and its large tsunami demonstrated the presence of a subduction megathrust and its capacity of hosting tsunamigenic rupture, but little has been done to include future potential thrust earthquakes in the Haida Gwaii region in tsunami hazard assessment. To fill this knowledge gap, I construct a new megathrust geometry using seismic reflection images and receiver-function results and produce nine tsunami sources for Haida Gwaii, which include buried and trench-breaching ruptures. In the strike direction, the scenarios include long ruptures from mid-way between Haida Gwaii and Vancouver Island to mid-way between Haida Gwaii and the southern tip of Alaskan Panhandle, and shorter rupture scenarios north and south of the main rupture of the 2012 earthquake. For all the tsunami source and paleoseismic scenarios, I also calculate stress drop along the fault. Comparison of the stress drop results with those of real megathrust earthquakes worldwide indicates that these models are mechanically realistic.

Table of Contents

List of Tables

List of Figures

Acknowledgements

I am very grateful for all those who helped make this research possible. Special thanks goes to my supervisor, **Kelin Wang**, who actively supported me throughout.

I would like to thank **Tania Lado Insua** and **Kelin Wang** for making this research possible by securing funding through Ocean Networks Canada and Natural Resources Canada.

I would like to offer special thanks to my supervising committee members, **Kelin Wang**, **Stan Dosso**, and **Edwin Nissen**.

I would like to thank **Taimi Mulder** for donating her time and efforts as my external examiner.

I wish to acknowledge the valuable assistance provided by many of the scientists and staff members at the Pacific Geoscience Centre (PGC), Geological Survey of Canada. **Kristin M.M. Rohr**, **Earl E. Davis**, and **Michael Riedel** for their help with interpreting seismic images, **Jiangheng He** for his computer expertise, and **Roy Hyndman**, **Honn Kao**, **Garry Rogers**, **John F. Cassidy**, **Randy Enkin**, **Ramin Mohammad Hosseini Dokht**, and **Ryan Visser** for their useful discussions and suggestions.

I would like to thank **Jason Padgett**, **Simon E. Engelhart**, and **Andrea D. Hawkes** for sharing in the beauty of Washington coastal marshes while collecting tsunami deposit samples.

I would also like to thank previous graduate students who studied under **Kelin Wang**'s supervision for sharing their models and wisdom. **Dawei Gao** for sharing his Cascadia tsunami source models, **Peiling Wang** for sharing her 1700 Cascadia earthquake models, and **Tianhaozhe Sun** for sharing his various megathrust rupture models.

I would also like to thank many of my other friends and colleagues including, **Haipeng Luo**, **Yuji Itoh**, **Yijie Zhu**, **Fengzhou Tan**, **Sarah Maleska,** and **Catherine England** for their support and helpful advice throughout my research.

Finally, I would like to dedicate this thesis to my family for their endless support and encouragement. Especially my loving wife, **Lingran Zhou**.

Chapter 1. Introduction

1.1. Background

Tsunamis pose considerable risk to coastal populations worldwide. Tsunamis can be caused by various sources including earthquakes, landslides, and meteorological conditions, but the most devastating tsunamis are caused by megathrust earthquakes along subduction zones. The grim consequences of such events in causing loss of life and property damage are most tragically displayed by recent events such as the *Mw* 9.2 2004 Sumatra earthquake (Lay et al., 2015), the *Mw* 8.8 2010 Maule, Chile, earthquake (Cárdenas-Jirón, 2013), and the *Mw* 9.0 2011 Tohoku-oki, Japan, earthquake (Lay, 2018). Tsunamis generated by such earthquakes can propagate across the ocean and cause damage in remote coastal areas, but the most severe impact is usually on the nearby coast in the same subduction zone. Defining such "local" tsunami sources for the west coast of North America from Haida Gwaii to northern California (Figure 1.1) due to subduction-type faulting directly offshore is the focus of this thesis.

Subduction zone earthquakes have a variety of rupture modes to generate tsunamis (Figure 1.2). In the simplest mode, called the buried rupture, the rupture remains on the megathrust without breaching the trench (Figure 1.2a), due to the shallow portion of the megathrust exhibiting a velocity-strengthening behaviour prohibiting cosesimic rupture. The shallow megathrust does not participate in coseismic slip but slips aseismically as shallow afterslip. The *Mw* 8.7 2005 Nias earthquake off Sumatra ruptured in such a manner, as confirmed by GPS measurements indicating little shallow coseismic slip followed by a substantial amount of shallow aseismic slip (Briggs et al., 2006; Hsu et al., 2006). There is indirect evidence and speculations that in some subduction zone earthquakes, the coseismic slip is diverted from the megathrust to a splay fault, greatly enhancing seafloor uplift and hence tsunami generation

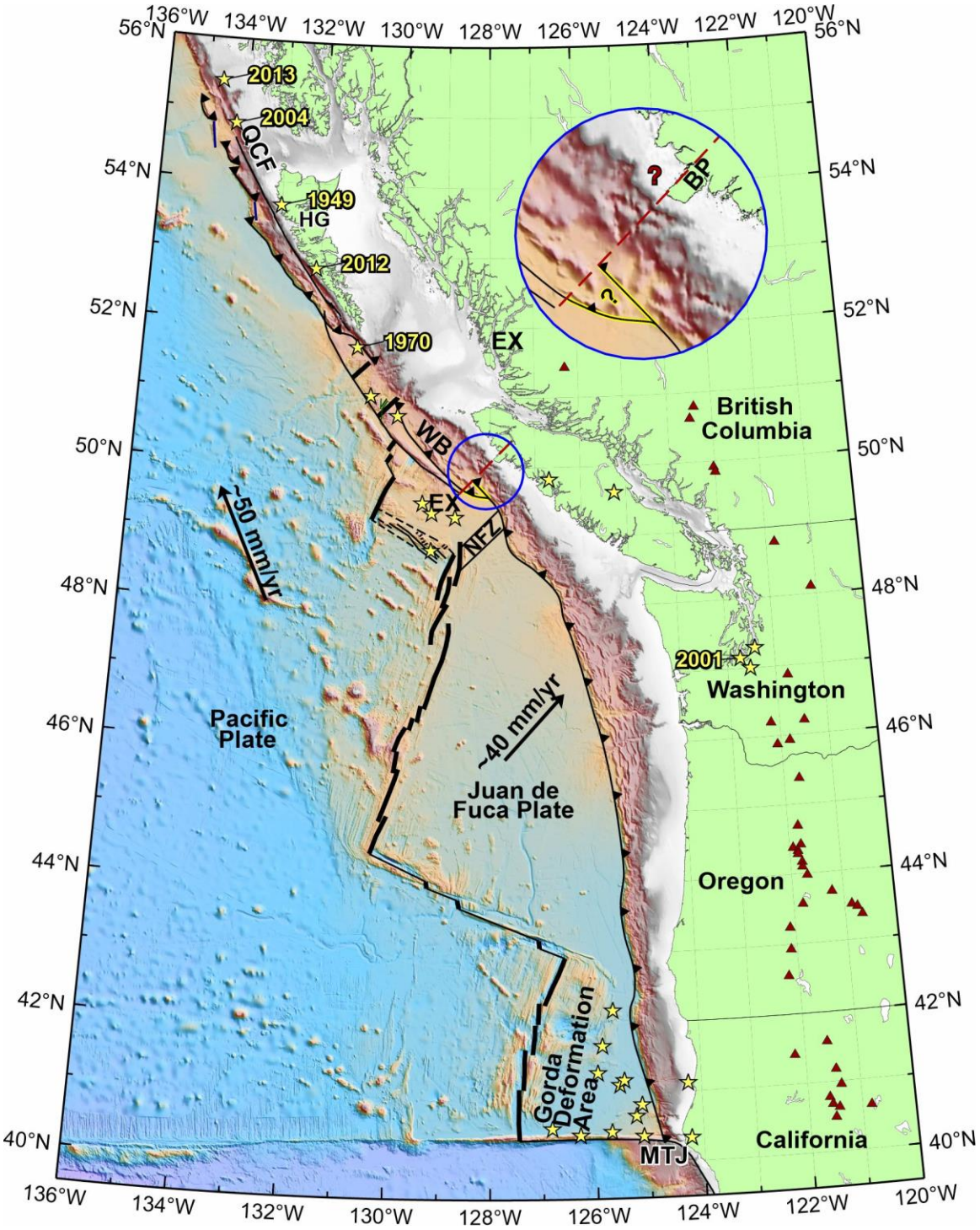

Figure 1.1. West coast of North America general tectonic setting. Inset shows uncertainty in the active deformation front SW of Brooks Peninsula. WB: Winona Basin. EX: Explorer plate. QCF: Queen Charlotte fault. NFZ: Nootka fault zone. BP: Brooks Peninsula. HG: Haida Gwaii. NFZ: Nootka fault zone. MTJ: Mendocino triple junction. Earthquakes shown (stars) are *Mw* 6.7+ events from the Advanced National Seismic System (ANSS)Catalog, with years labelled for large Queen Charlotte margin earthquakes and the *Mw* 6.8 2001 Nisqually earthquake near Seattle. Plate motions relative to North America are derived from DeMets et al. (2010).

(Figure 1.2b). A possible example is the *Mw* 8.1 1946 SW Japan earthquake (Baba et al., 2006). More recently, it has been increasingly recognized that some megathrust earthquakes can have a large amount of coseismic slip breaching the seafloor trench (Figure 1.2c), as seen for the *Mw* 9 2011 Japan earthquake (Fujiwara et al., 2011; Kodaira et al., 2012; Sun et al., 2017b). Some subduction zones hold a very large amount of trench sediment that masks the buried basement topography making it difficult to determine the megathrust structure and dynamics, although some seafloor bathymetric features reveal how the shallowest portion of the megathrust may rupture. Wang and Tréhu (2016) hypothesized that the Cascadia subduction zone has a complex frontal structure based off bathymetric features and seismic data (Figure 1.2d).

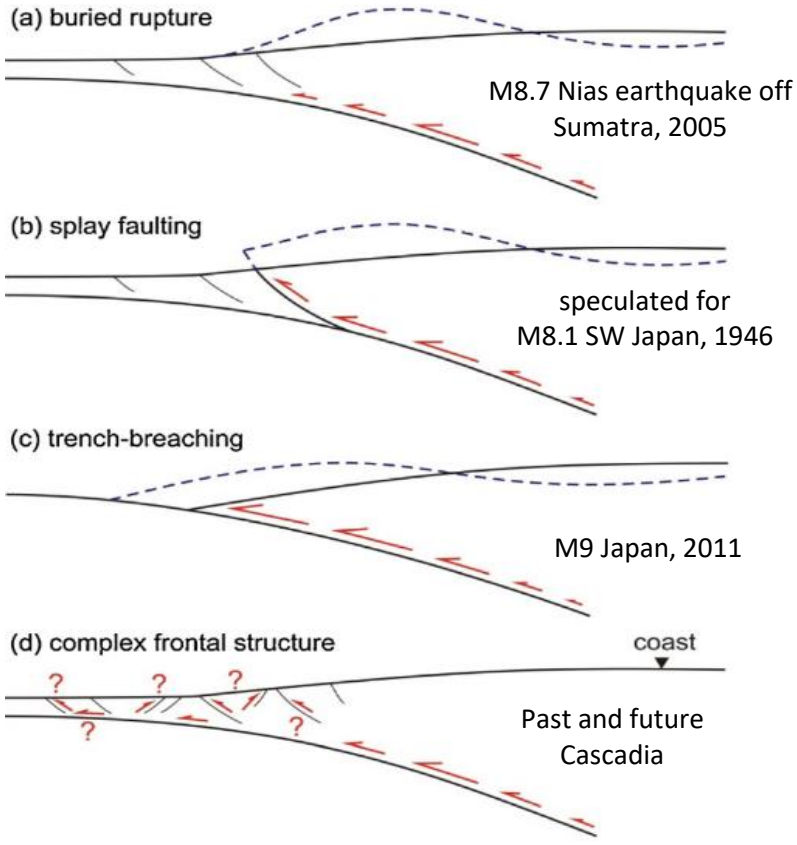

Figure 1.2. Range of megathrust rupture scenarios (Wang and Tréhu, 2016). For figures (a) to (c) the pre- and post-seismic bathymetry are shown as solid and dashed lines, respectively, for the three main rupture types.

The main tsunami threat for the west coast of North America is from the Cascadia

subduction zone, which extends from the Mendocino Triple Junction in the south, to the north bound of where there is evident subduction of the Explorer Plate (Figure 1.1). The Cascadia subduction zone has been extensively studied with many geophysical and geological methods, and its tectonic and geodynamic processes are reasonably well understood. The last large megathrust earthquake is estimated to be a *Mw* ~ 9 event that occurred on 26 January 1700 and resulted in a large tsunami that caused damage as far away as Japan across the Pacific (Satake et al., 2003). There are other large earthquakes that occur within the overriding North America (NA) plate or the JDF slab before and after subduction (Figure 1.1), but these events have not been known to generate considerable tsunamis (e.g. *Mw* 6.8 2001 Nisqually earthquake near Seattle (Figure 1.1)).

The Winona Basin area north of the Cascadia subduction zone (Figure 1.1) is much less well understood, and there are competing tectonic models. In one of these models, the Winona block, a piece of the oceanic lithosphere recently broken off the Explorer plate, is subducting beneath NA, potentially producing tsunamigenic thrust earthquakes. Further north, the subduction zone transitions to the transpressive Queen Charlotte margin through an area of complex geological structures and processes. North of ~50°N there have been several low magnitude earthquakes with primarily strike-slip mechanisms indicating the region is under transpression, but these strike-slip events are not expected to be common major tsunami sources. No significant thrust earthquakes have been observed within the Winona Basin. If there is a major thrust interface above the Winona block, it has been silent in the recent past, either fully locked or creeping aseismically.

Haida Gwaii is located in the southernmost part of the Queen Charlotte margin (Figure 1.1), where the motion of the Pacific (PA) plate with respect to the NA plate is predominantly

margin-parallel but with a small convergence component. The convergence angle is about 21º at Haida Gwaii but gradually decreases to zero some distance north of Haida Gwaii. There are competing tectonic models to explain how the convergence component is accommodated, but the occurrence of the *Mw* 7.8 low-angle thrust earthquake off Haida Gwaii in 2012 and its ensuing large tsunami strongly support the model in which the convergence takes place in the form of the PA plate subducting beneath the NA plate. Other significant large earthquakes along the Queen Charlotte margin include the 1949 *Ms* 8.1, 1970 *Ms* 7.4, 1972 *Ms* 7.6 and 2013 *Mw* 7.5 strike-slip earthquakes (Figure 1.1). There are reports that a significant tsunami run-up was observed from some of these earthquakes, such as 3 m run-up from the 1949 Queen Charlotte Islands earthquake (Prince Rupert Daily News of August 27, 1949), but these waves were localized in limited areas and most likely were the result of triggered submarine landslides. As for the most recent large strike-slip earthquake, the *Mw* 7.5 2013 Craig earthquake, some coastal communities reported wave heights up to 2.5 cm. Strike-slip underwater earthquakes may cause large tsunamis under very special circumstances by triggering submarine landslides, such as the recent *Mw* 7.5 2018 Palu earthquake (Carvajal et al., 2019). In this thesis, I do not further discuss strike-slip events but focus on thrust earthquakes that are much more potent in generating tsunamis.

This work is focused on modelling the tsunami sources needed by the hazard assessment, not on the assessment itself. It contributes to the national effort to assess the tsunami hazard of the west coast of Canada, which is of great importance for coastal Canadian communities (i.e. Cities of Victoria, Vancouver, Port Alberni, Tofino, Ucluelet, Port Renfrew and many Indigenous communities). A preliminary tsunami hazard assessment for the entire Canadian coastline was completed by Leonard et al. (2012; 2014) and provides guidance for future more-detailed analyses.

1.2. Previous Work on Tsunamigenic Rupture Models

For the three areas studied in this work, a varying amount of previous research has gone into estimating tsunami sources associated with earthquakes. Of the three, Cascadia by far has attracted the greatest attention, and a number of source scenarios have been proposed (Satake et al., 2003; Cherniawsky et al., 2007; Priest et al., 2010; Witter et al., 2013; Gao, 2017; Gao et al., 2018). A potential Winona megathrust rupture has never been considered in hazard assessments. Haida Gwaii has been included in tsunami hazard assessments (Leonard et al., 2012; 2014), but the assumed source models were largely qualitative.

Cascadia tsunami source scenarios have developed through time as our understanding of what types of rupture are possible for the Cascadia subduction zone expanded. Various buried rupture scenarios created by Satake et al. (2003) were able to approximately fit the 26 January 1700 tsunami wave heights recorded at seven locations along Japan's coastline. Since then, there has been a great deal of effort to understand tsunami impact along the west coast of North America for various potential future megathrust rupture scenarios (Cherniawsky et al., 2007; Priest et al., 2010; Witter et al., 2013; Gao, 2016; Gao et al., 2018). Earlier models of Cascadia tsunamigenic megathrust rupture assumed uniform slip of a shallow segment of the megathrust which linearly tapers to zero at a greater depth (Satake, 2003; Cherniawsky et al., 2007). Such a rupture pattern was based on the interseismic locking pattern crudely inferred from thermal modelling and the then limited geodetic constraints (e.g., Hyndman and Wang, 1993, 1995). Satake et al. (2003) also tested a highly simplified splay-faulting scenario for the 1700 earthquake but found that it did not make a significant difference to tsunami impact on the Japanese coast. Priest et al. (2010), in constructing models for tsunami hazard assessment along the Oregon coast, began to include smoothly distributed slip distribution along the megathrust.

As will be detailed in section 2.4, their model of downdip distribution of coseismic slip is still used in the current research. Priest et al. (2010) also considered splay-faulting tsunami source scenarios for Cascadia. In contrast with the trans-Pacific tsunami modelled by Satake et al., (2003), Priest et al. (2010) found that splay faulting, which results in more uplift closer to shore, can generate much larger tsunamis on the local coast than does the buried rupture with a similar moment magnitude. Further development of the suite of buried rupture and splay faulting scenarios for Oregon was then provided by Witter et al. (2013). After the 2011 *Mw* 9 Tohoku-oki earthquake and tsunami, the potential of trench-breaching megathrust rupture (Figure 1.2c) gained greater attention. Trench-breaching scenarios were then added to the suite of scenarios by Gao (2016). The suite of 15 northern Cascadia megathrust rupture scenarios in Gao et al. (2018) was created by applying some minor modifications to fault geometries to a subset of the Gao (2016) scenario suite. Interestingly, Gao et al. (2018) found that the trench-breaching scenarios do not generate greater tsunamis at the coast compared to the buried rupture for the same peak slip and similar slip distribution, mainly because of the gentle topographic gradient of the continental slope at northern Cascadia as compared to that of the Japan Trench.

No tsunami hazard assessment has ever included Winona tsunami source scenarios, since the tectonics of the Winona area are poorly understood. However, Gao (2016) determined that the proposed megathrust at the Winona Basin appears to have suitable thermal conditions to host thrust earthquakes and thus potentially generate tsunamis.

The current tsunami hazard assessment for the Canadian coast includes the potential rupture of the Haida Gwaii megathrust, which utilizes a simplified rectangular fault and empirical scaling relationships for various parameters (Leonard et al., 2012; 2014). After the *Mw* 7.8 2012 Haida Gwaii earthquake, various studies have used the seismologically and/or

geodetically determined rupture models for this event to simulate its tsunami impact on Haida Gwaii and other coastlines (Shao and Ji, 2013; Lay et al., 2013; Nykolaishen et al., 2015; Fine et al., 2015). Since then, further efforts have gone into understanding the fault geometry and potential rupture dynamics, but little has been done to include future potential thrust earthquakes along the same margin but beyond the 2012 rupture zone.

1.3. Objectives of the Thesis Research

The overall objective of this research is to construct or refine tsunami source scenarios for Cascadia, Winona, and Haida Gwaii to the best of our knowledge of the regional tectonics, fault behaviour, and tsunami generation processes. This work will contribute to determining the tsunami hazard along the west coast of North America. The source scenarios generated in this work can be used as inputs for engineers running tsunami simulations, which will be utilized eventually in a weighted hazard assessment of the west coast of North America. This thesis research is also part of the Canadian Safety and Security Program (CSSP) supported by Natural Resources Canada and a Tsunami Early Warning Initiative led by Ocean Networks Canada.

After the completion of a MSc thesis by Gao (2016), I improved the accuracy of the Cascadia megathrust geometry used for modelling, especially for the splay-faulting and trench-breaching models, as part of my MSc research. In the previous versions of interpolated splay and trench breach geometries, a shallow segment of the megathrust was deeper than the corresponding buried fault geometry due to the interpolation algorithm used to generate a continuous fault surface from few depth contours. The improved geometry was employed by the recently published tsunami source study by Gao et al. (2018) for northern Cascadia. Some of the details of that effort is documented in this thesis. I have made additional adjustments to the megathrust geometry in southern Cascadia by utilizing new depth estimates from Hayes et al.

(2018), which are physically more reasonable compared to the previously used McCrory et al. (2012) depth estimates. Due to a change in the southern Cascadia fault geometry, I modified the location of the downdip rupture boundary (to be further discussed in section 3.3). To improve our understanding of the tsunamigenic earthquake threat, research into determining rupture characteristics of ancient events, such as the 1700 Cascadia megathrust earthquake, is also important. I have created rupture scenarios for the 1700 earthquake based on newly available paleoseismic data (Kemp et al., 2018; Padgett, 2019).

Even though it is not certain whether the Winona block is underthrusting NA, it is still important to construct a potential megathrust scenario for the sake of tsunami hazard assessment. In this work, I will make further effort to understand the Winona block geometry and rupture area, which I use to construct a suite of tsunami source scenarios for the hypothesized Winona block thrust fault. I anticipate that the weighting of such Winona tsunami source scenarios for the overall west coast tsunami hazard assessment will be low relative to Cascadia and Haida Gwaii sources.

The strike-slip Queen Charlotte Fault (QCF) is accompanied with a subduction megathrust (QCMT) off Haida Gwaii. From the *Mw* 7.8 2012 Haida Gwaii thrust earthquake, it is known that this megathrust is able to produce large thrust earthquakes, but less is known about the seismogenesis of the megathrust outside the 2012 earthquake region. For assessing hazard, it should be assumed that a megathrust rupture is possible as long as the convergent component of relative plate motion is not zero. As will be detailed in section 5.3, this means that the zone on the QCMT that is susceptible to tsunamigenic rupture extends far outside the rupture region of the 2012 earthquake. In this work, I propose a suite of megathrust rupture scenarios based on presently available data and their interpretations within the Haida Gwaii region.

Chapter 2. Modelling Method

2.1. 3-D Dislocation Model

To calculate the coseismic seafloor uplift and the fault surface stress changes for our rupture scenarios, I use a computer code named *Disl3d14*, written by Dr. Kelin Wang. *Disl3d14* numerically integrates point-source dislocation solutions (Green's functions) of Okada (1992) over a fault with realistic geometry in a uniform elastic half-space to produce displacement, strain, and stress values at observation points on the half-space surface, on the fault, or elsewhere within the half-space (Figure 2.1). The modelling process involves first constructing a 3-D fault mesh consisting of triangular integration elements, then assigning slip vectors to these elements, and finally calculating surface deformation and fault stress changes.

A simpler version of this modelling strategy was earlier applied to Cascadia megathrust modelling by Flück et al. (1997), Wang et al. (2003), and Satake et al. (2003). The three-dimensionally curved megathrust was approximated using several 2-D margin-normal profiles of arc shape, and slip (or slip deficit) were assigned to the fault in a simple manner. A major revision of the code took place in 2006, resulting in a version called *Disl3d06*, which introduced the ability to handle an arbitrarily curved megathrust geometry and complex slip (or slip deficit) distribution along the fault surface. With this version, Priest et al. (2010) and Witter et al. (2013) employed a realistic 3-D fault geometry without simplification. They also assumed a slip distribution in the dip direction with the slip tapering both updip and downdip from a peak value; the function they used will be detailed in section 2.4. To explain coastal subsidence estimates for the 1700 Cascadia megathrust earthquake based on micro-fossil analyses, Wang et al. (2013) created heterogeneous rupture models consisting of high-slip patches separated by low-slip areas. For the high-slip patches, the slip tapers in both the dip and strike directions. Another major

update took place in 2014 to enable the ability to calculate stress drop due to shear slip on the megathrust fault, resulting in the present version *Disl3d14*. Brown (2015) and Brown et al. (2015) used *Disl3d14* to calculate megathrust stress drop distribution in the 2011 *Mw* 9 Tohoku-oki earthquake based on 40 published coseismic slip models for this earthquake. Sun et al. (2017a) used the same version to calculate stress drop for the 2012 *Mw* 7.6 Costa Rica earthquake and its afterslip. Gao (2016) used *Disl3d06* for the 21 tsunami sources. When modifying the models of Gao (2016) to create the models in Gao et al. (2018), I used *Disl3d14*.

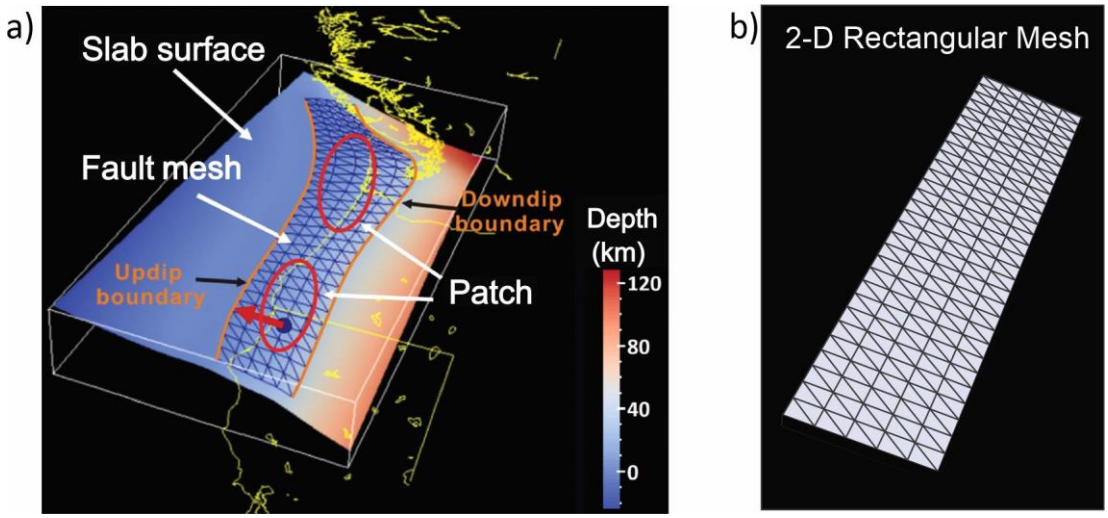

Figure 2.1. Schematic illustration of the dislocation model. (a) A 3-D perspective view for the Cascadia model, modified from Wang (2012) and Gao (2016). The triangular integration elements used in modelling are much smaller than shown here. (b) The 2-D rectangular mesh (discussed in section 2.3) before it is mapped to the 3-D fault surface.

2.2. Megathrust Geometry

To create a megathrust fault model of realistic geometry, I use control depths from published papers and interpretations from seismic or other types of geophysical imaging. I create a gridded smooth surface from these control depths with an interpolation algorithm such as those available in the Generic Mapping Tools (GMT) software (Wessel and Smith, 1998). In some cases, a gridded fault surface that is already provided by other researchers can be imported (e.g., Hayes et al., 2018), but it is often necessary to make refinements by fine-tuning different areas to

avoid anomalous uplift and stress change results. In that situation, it is often more convenient to extract depth contours from the imported gridded surfaces, fine-tune these contours, and regenerate the gridded surface from the improved contours.

Details of seafloor and coastal topography are important for modelling tsunami waves, but very long-wavelength topography is important for the modelling of coseismic deformation as tsunami sources. However, the dislocation model assumes an elastic half-space with a flat free surface and cannot incorporate the real long-wavelength topography of subduction zones. Therefore, I make an adjustment to the megathrust geometry as shown in Figure 2.2a, so that the fault depth below the flat surface in the model is similar to the fault depth below seafloor in reality. If the rupture breaches the trench, the geometrical adjustment shown in Figure 2.2a results in exaggerated coseismic uplift near the trench. However, this over-prediction happens to compensate for the missing effect of the seaward motion of the sloping seafloor as explained by Wang et al. (2018) and illustrated in Figure 2.2b. If α is the seafloor slope angle and β is the near-trench fault dip, the adjustment changes the fault dip to approximately $\alpha + \beta$. Without this adjustment, if the fault slip is s at the trench, the seafloor rise due to the rigid-body translation of the upper plate is $u = s\sin(\alpha + \beta)/\cos\alpha$. With the adjustment, the seafloor rise is $u' \approx s\sin(\alpha + \beta) = u\cos\alpha$. Because α is a small angle, $\cos\alpha \approx 1$, and hence $u \approx u'$.

There are further complications at Cascadia. Because of the thick sediment, trench-breaching rupture does not break the seafloor at the trench in the simple manner illustrated in Figure 1.2c. The geometrical adjustment illustrated in Figure 2.2a is appropriate for a subduction zone that has little or no trench sediment. The adjustment shown in Figure 2.2c is more appropriate for Cascadia where the megathrust is buried by 2 – 4 km of sediment at the deformation front (called trench here). After the geometrical adjustment, the fault at the trench is

still buried. Following Gao (2016) and Gao et al. (2018), I assume that the trench-breaching rupture breaks the seafloor by activating a frontal thrust, a hybrid of the situations illustrated in Figure 1.2c and 1.2d.

The frontal thrust curves down from the surface trace at some angle defined with seismic reflection images and merges with the megathrust (green line in Figure 2.2c). The splay-fault geometry is generated in the same fashion, except that the surface trace is located at a location landward of the deformation front, and it soles into the megathrust at a greater depth (not shown in Figure 2.2). Generally, I construct the frontal thrust (or splay-fault) geometry through the interpolation of the deformation front (or splay trace), a shallow depth contour which is a short distance landward of the seafloor trace that sets the shallow dip (e.g. 30° from model surface), and a large portion of the buried megathrust.

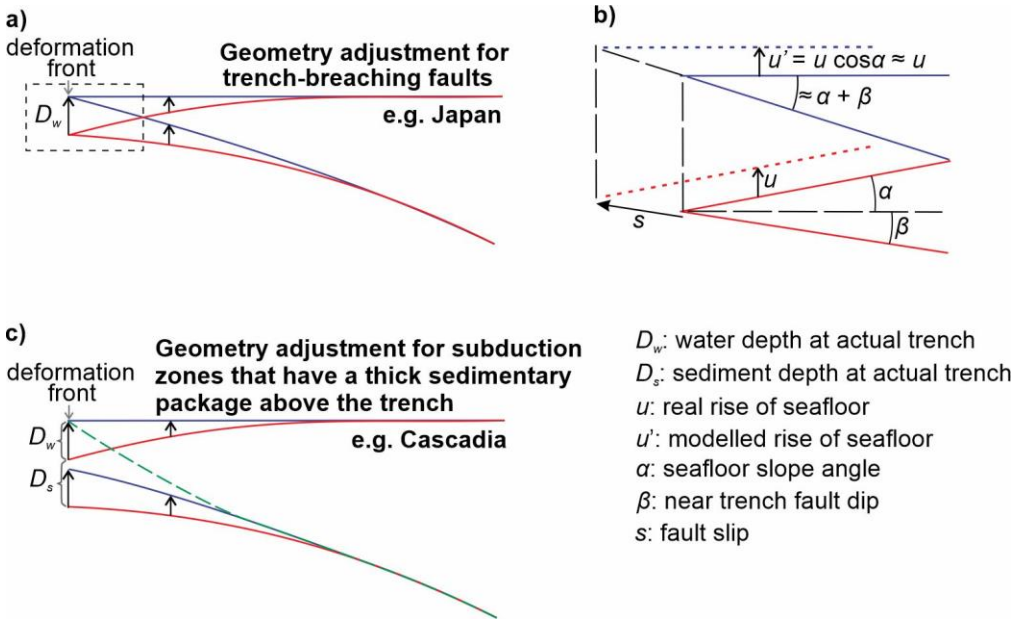

Figure 2.2. Fault geometry adjustment made to models using a flat-top (modified from Wang et al. (2018)). The megathrust fault and seafloor are shown for before (solid red line) and after (solid blue line) the adjustment. (a) Geometry adjustment for subduction zones that have little to no sediment covering the trench. (b) Schematic illustration to show how the fault geometry adjustment compensates for the neglected seafloor slope in the case trench-breaching rupture. (c) Geometry adjustment for subduction zones that have a significant sediment thickness burying the trench. Green dashed line is a frontal thrust that allows the sediment-buried megathrust (solid blue line) to have trench-breaching rupture.

2.3. Constructing 3-D Fault Mesh

A 2-D rectangular mesh containing linked triangular elements is first created in a Cartesian system (Figure 2.1b). By utilizing a 2-D rectangular mesh, we are able to simplify operations such as assigning slip distribution (section 2.4). The 2-D rectangular mesh is then mapped onto the 3-D fault in the geographic system in which the mesh has curved updip and downdip boundaries (Figure 2.1). To avoid badly distorted triangles, it is expedient to assign the 2-D rectangular mesh dimensions to be similar to the real fault dimensions. The updip mesh boundary is set to be along either the deformation front or the splay trace, and the downdip boundary is deep enough to accommodate any potential rupture distribution.

The size of an integration triangle is assigned by considering how far away from the point-source dislocation the deformation or stress calculation is to be calculated (called the observation point). If the observation point is near the fault, the triangles must be small. For example, for calculating seafloor (top model surface) deformation, coarse triangles (~3 km triangles or much larger) can be used in the deep part of the fault. However, if the fault breaches the seafloor, small triangles (~300 m triangles) are required on either side of the fault trace because these observations points are very close to the fault. Therefore, when calculating seafloor deformation, a mesh containing non-uniform triangular elements coarsening in the downdip direction can be used to save computing time.

2.4. Assigning Slip Distribution

Ideally, slip vector distribution can be assigned by sourcing independent studies, which is what was done for the earthquakes discussed in the appendix. However, in some cases, this is not possible due to the lack of data constraining previous events and/or there is a need to generate hypothetical future rupture scenarios, such as for the Cascadia, Haida Gwaii, and Winona cases.

For ruptures that have slip tapering to zero both updip and downdip, the slip magnitude in the dip direction is assigned by the 1-D slip function proposed by Wang and He (2008), with typographic errors corrected in Wang et al. (2013):

$$s(x') = s_o \delta\{1 + \sin[\pi \delta^b]\} \tag{2.1}$$

$$\delta(x') = \begin{cases} \dfrac{6}{q^3} x'^2 \left(\dfrac{q}{2} - \dfrac{x'}{3}\right) & 0 \le x' \le \mathrm{q} \\ \dfrac{6}{(1-q)^3}(1-x')^2 \left(\dfrac{1-q}{2} - \dfrac{1-x'}{3}\right) & q \le x' \le 1 \end{cases} \tag{2.2}$$

where $x' = x/w$ is the downdip distance x from the upper bound of the rupture zone normalized by the local downdip width w, q is a skewness parameter that ranges from 0 to 1, b is a broadness parameter that ranges from 0 to 0.3, and s_o is the peak slip along the given profile. The direction of the slip vector at each nodal point is assigned or calculated from relative plate motion Euler vectors as explained in Wang et al. (2003). For my buried rupture models, I use a symmetric bell-shaped slip distribution in the fault dip direction with b = 0.2 and q = 0.5 (Figure 2.3a).

With small modifications to this bell-shape distribution, the splay and trench-breaching distributions can be dervied. To assign slip magnitude for splay rupture scenarios, the bell-shaped slip of a corresponding buried rupture model is simply mapped onto the splay scenario's fault mesh, resulting in an abrupt termination of slip at the seafloor (Figure 2.3b). When assigning slip magnitude for trench-breaching scenarios, the bell-shaped distibution is used for the deeper half of the rupture, while for the shallower half the slip is assigned to taper down from the peak value to some lower value at the deformation front (Figure 2.3c). If needed, the along-strike slip magnitude is scaled with local relative patch width w as $(w/w_k)^n$, where $k = 1, 2$, $n \ge 0$. Here w_k is an unscaled, reference local width some distance from either terminus of the

rupture in the strike direction, and the scaling is between this location and the rupture terminus (Figure 2.4b). If $w_1 = w_2 =$ the unscaled local width at the centre of an elliptical slip patch, and $n = 2$, the scaling will result in a bell-shaped slip distribution along-strike as well as in the dip direction (Wang et al., 2013) (Figure 2.4a).

For all the seafloor breaching models, the updip rupture boundary is at the fault trace. For the buried rupture, the updip boundary is set to be directly below the deformation front. The downdip rupture limit can also be defined with thermal arguments with some simplifying assumptions (e.g., Hyndman Wang, 1993), but this cannot always be accomplished due to a lack of thermal data.

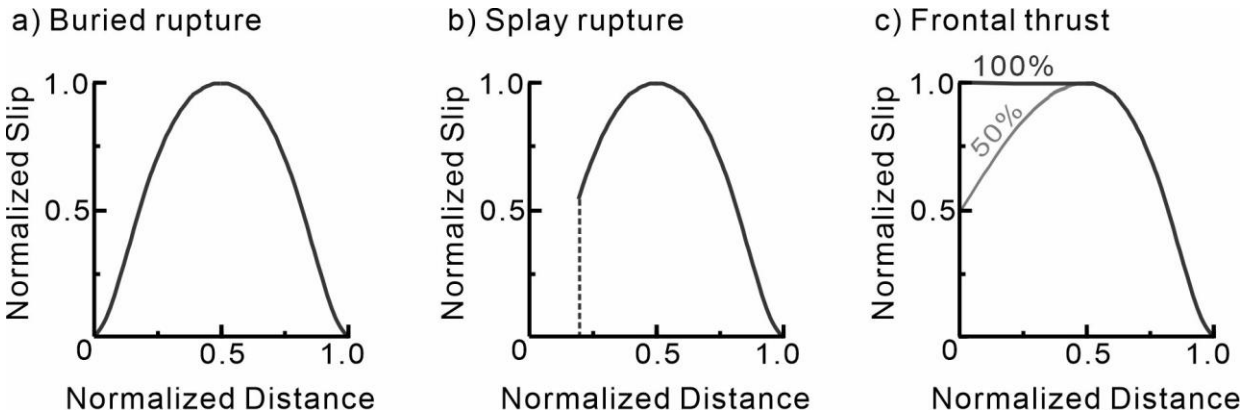

Figure 2.3. Normalized slip in the downdip direction used in this work (modified from Gao, 2016). (a) Buried rupture, featuring symmetric bell-shape slip distribution with $b = 0.2$ and $q = 0.5$. (b) Splay-faulting rupture. The distribution is simply the bell-shaped distribution in (a) truncated where the fault meets the splay trace at zero depth. (c) Trench-breaching rupture. The distribution is of the bell-shaped downdip of peak slip but tapers to a prescribed percentage of the peak slip.

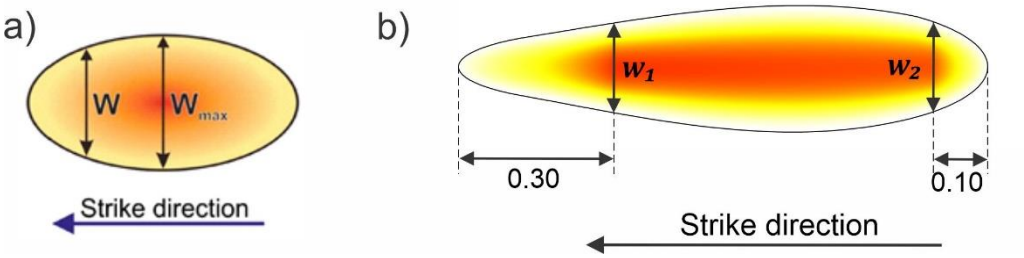

Figure 2.4. Illustrations showing how the along-strike slip scaling relationship is dependent on the slip patch width (w). (a) In Wang et al. (2013) slip is scaled by the local width (w) relative to the maximum width (w_{max}) by the relationship $(w/w_{max})^2$. Warmer colour means larger slip. (b) In this work slip is scaled by width (w) relative to some reference width (w_k, where $k = 1, 2$) defined at some distance from each terminus of a slip patch. The illustrated example (b) uses the along-strike scaling relationship $(w/w_k)^n$, where $n = 2$, to scale slip within 10% and 30% of the patch terminuses.

The amount of energy released during an earthquake is represented by the moment magnitude, which is based on seismic moment. The seismic moment (M_0) is defined by

$$M_0 = \mu A \bar{s} \tag{2.3}$$

where μ is the shear modulus, A is the rupture area, and $\bar{s}$ is the average slip. The definition of moment magnitude is (Hanks and Kanamori, 1979)

$$M_w = (\log_{10} M_0 - 9.1)/1.5 \tag{2.4}.$$

2.5. Calculating Stress Drop

Static shear stress change, or stress drop ($\Delta\sigma$), during an earthquake along the fault surface over the rupture zone is an important parameter in earthquake mechanics. Average static stress drop ($\overline{\Delta\sigma}$) for a planar fault with a simple slip distribution follows the scaling relationship (Scholz, 2002)

$$\overline{\Delta\sigma} = C\mu\frac{\bar{s}}{L} \tag{2.5}$$

where C is a constant that depends on the shape of the rupture zone, μ is shear modulus, $\bar{s}$ is average slip, and L is a characteristic rupture length. For megathrust earthquakes, L is typically the width of the rupture zone in the dip direction. With complex fault geometry and slip distribution, in particular for large earthquakes, estimating the average slip and characteristic rupture length can be challenging. Instead, I determine $\Delta\sigma$ values at all individual points of the rupture zone of known slip distribution and then take a spatial average.

Disl3d14 calculates $\Delta\sigma$ at any point by numerically integrating point-source dislocation solutions over the fault. This is accomplished by determining the internal deformation within the elastic half-space and using Hooke's Law to relate the associated strain to changes in stress. For this thesis, the calculation assumes a Poisson's ratio of 0.25 and shear modulus of 40 GPa. The average shear modulus appropriate for megathrust earthquakes depends on the depth of the rupture. Generally, the deeper the rupture, the higher the shear modulus should be. For most scenarios, a 40 GPa shear modulus is appropriate. However, for some cases like for the *Mw* 8.1 2003 Tokachi earthquake, the main rupture occurs very deep on the megathrust where the shear modulus is greater. The opposite is true for shallow rupture earthquakes such as for the *Mw* 8.3 2006 Kuril Island earthquake.

Stress drop cannot be mathematically derived directly on the fault, which is a displacement discontinuity, but can be accurately represented by values at a very short distance from the fault. The closer the $\Delta\sigma$ is calculated to the fault the more accurate it will be, but a large enough distance is required to help smooth out the effect of using a discrete mesh of integration triangles for the fault. For this work, I calculate $\Delta\sigma$ 2 km below the fault and assign the entire mesh to have triangles approximately half the size of the offset distance (i.e. 1 km). With smaller fault mesh triangles, $\Delta\sigma$ could be calculated even closer to the fault. However, given the large

wavelengths of the $\Delta\sigma$ distributions we consider, this would bring no improvement to the results.

Disl3d14 has been used by Brown et al. (2015) to calculate stress changes for 40 different *Mw* 9.0 2011 Tohoku-oki slip models to better understand $\overline{\Delta\sigma}$ of that event. In this work, $\Delta\sigma$ is calculated for all our Cascadia, Winona, and Haida Gwaii models (in their respective sections) as well as for 11 real megathrust events worldwide (appendix). The $\overline{\Delta\sigma}$ of these real earthquakes will be compared to $\overline{\Delta\sigma}$ of our hypothetical tsunami source and paleoseismic models.

Our west coast of North America megathrust rupture scenarios should be constrained by the knowledge of earthquake mechanics as well as observations. Observations that constrain Cascadia megathrust geometry include earthquake locations, seismic tomography, and seismic imaging with controlled sources. Observations that help constrain the rupture dimension include thermal data and paleoseismic observations of coseismic coastal subsidence. When investigating the $\Delta\sigma$ of our tsunami source models and paleoseismic models there are two main questions to address: (1) Is the average static stress drop, $\overline{\Delta\sigma}$, within a reasonable range as per other studies and the 11 real megathrust cases I calculate $\Delta\sigma$ for? (2) Is the distribution of the static stress drop, $\Delta\sigma$, physically reasonable?

Chapter 3. Cascadia Megathrust Paleoseismic and Tsunami Source Models

3.1. Cascadia Megathrust Geometry

For Cascadia, a gridded fault geometry is constructed in the same fashion as in Gao et al. (2018). Like in Gao (2016) and Gao et al. (2018), the contour depths from McCrory et al. (2004) and Gao et al. (2017) were used for mid- and northern Cascadia, respectively. However, unlike in Gao (2016) and Gao et al. (2018), the southern Cascadia contour depths are controlled by the Slab2 model (Hayes et al., 2018). The choice to use Slab2 contour values, instead of McCrory et al. (2012) contours, in southern Cascadia was due to its smoothness and simplistic trend along-strike. There are two interpolated regions smoothly connecting the three regions that are based on published geometry models (black lines, Figure 3.1d).

For the fault geometry adjustment (Figure 2.2), the exact shelf edge should not be where the model fault begins to be steeper than the real fault, as the resulting corrected slab surface would be very irregular. Instead, a line that generally follows the 15 km contour line is used as the starting point of the geometrical adjustment. Figure 3.2 shows examples of how the megathrust geometry is adjusted in three different places along the margin.

Seismic reflection images can help the construction of the frontal thrust and splay fault geometries. The frontal thrust and two of the three splay traces (splay A and B in Figure 3.1) used in this modelling are directly from Gao (2016) and Gao et al. (2018). The deformation front trace for the Explorer plate shows sudden orientations changes along-strike (Figure 1.1 inset), but not much is known about the tectonics transitioning from the Explorer plate to Winona block beneath the sediment cover, and for that reason I use the smoothed deformation front trace by Gao (2016) that does not follow the actual more complex deformation front. Upon further examining available northern Cascadia seismic reflection images, I found it necessary to

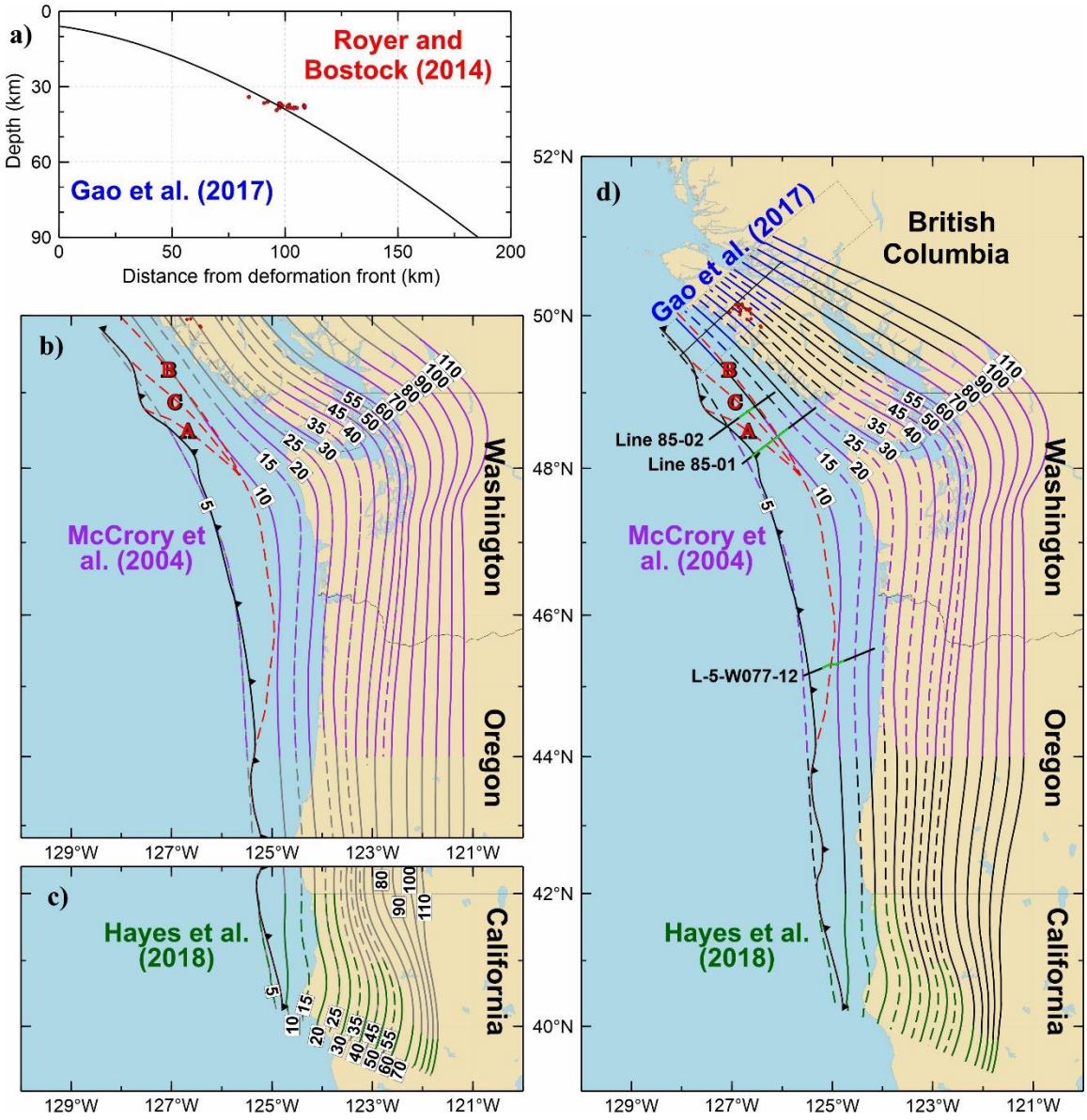

Figure 3.1. Slab surface depth for Cascadia. (a) Gao et al. (2017) model based on Royer and Bostock (2014) low frequency earthquakes (red circles). (b) Depth contours of McCrory et al. (2004). (c) Depth contours of Hayes et al. (2018). (d) Combined depth contours. The three published segments are smoothly connected by hand (black lines). The trench is shown as solid black line with triangles. Splay fault traces A, B, and C are labeled and drawn as dashed red lines. Light green lines show locations of seismic reflection images found in Figure 3.3.

introduce another hypothetical splay fault. The locations of two of the seismic reflection lines quoted by Gao (2016) are shown in Figure 3.1d, together with line L-5-W077-12 (Mann and Snavely, 1984; Priest et al., 2010), and all the three seismic images are shown in Figure 3.3. The resolution of the seismic reflection images from lines 85-01 and 85-02 (Yorath et al., 1988) is

low, but it appears that there could be minor splay fault offsets masked by the bottom simulating reflector (BSR) for splay C in Figure 3.3. There is also a distinct seafloor slope change at the indicated splay C locations along lines 85-01 and 85-02. Through observations of seismic reflection images for the Cascadia subduction zone, the dip of the shallowest portions of the frontal thrust fault and splay faults is ~30°. For simplicity this 30° dip is applied along the entire

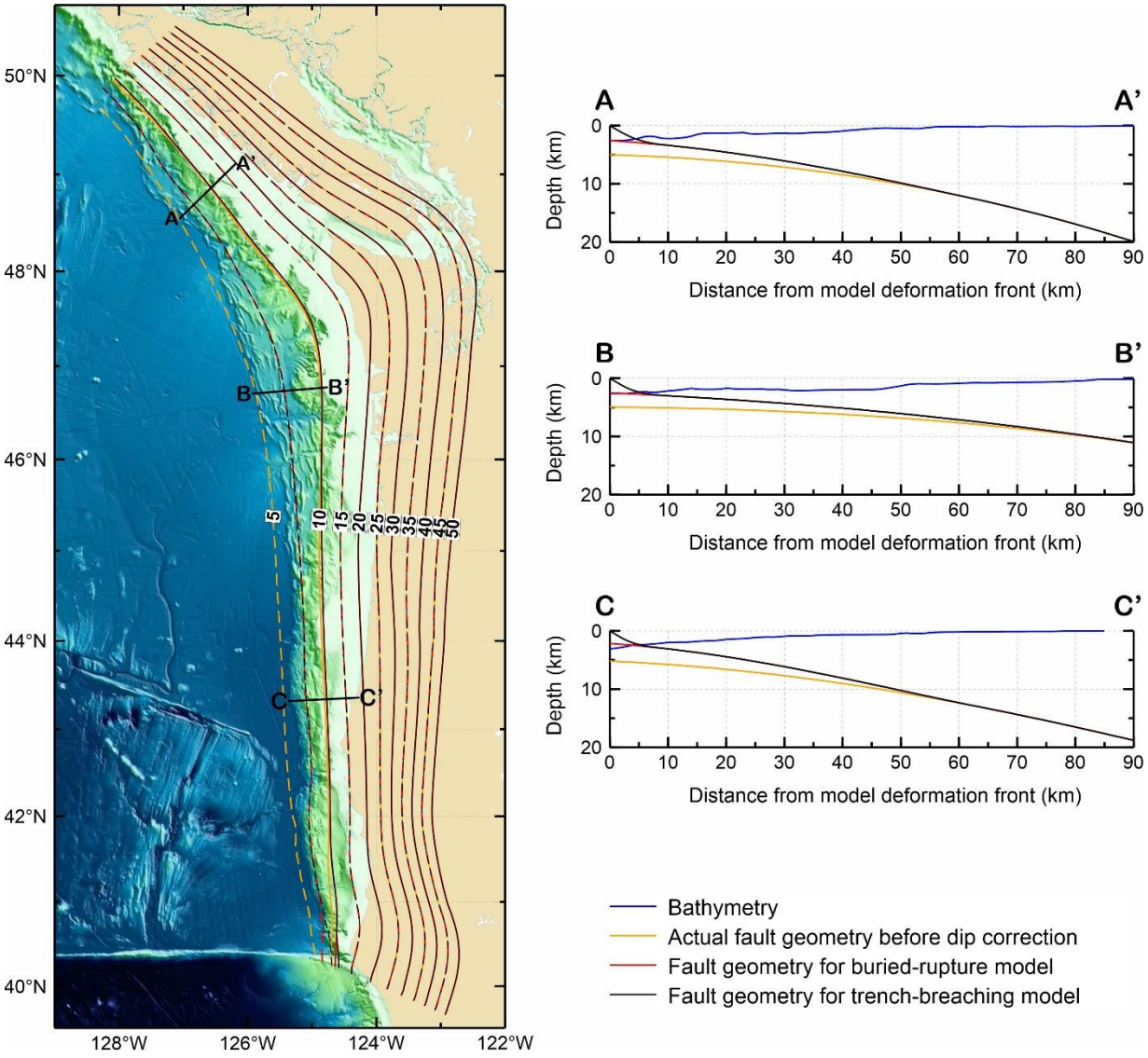

Figure 3.2. Megathrust geometry proposed in this work before the geometry adjustment described in section 2.2 (orange) and after the correction for both the buried (red) and the trench-breaching (black) rupture models. (Left) The 5 km (dashed) and 10 km (solid) depth contours before and after the geometrical adjustment. (Right) Selected profiles to show how the megathrust geometry is adjusted. Profile locations are shown on the map.

margin for the frontal thrust and splay geometries. To ensure the shallowest portions of the fault geometries have a 30° dip the procedure discribed in section 2.2 is carried out.

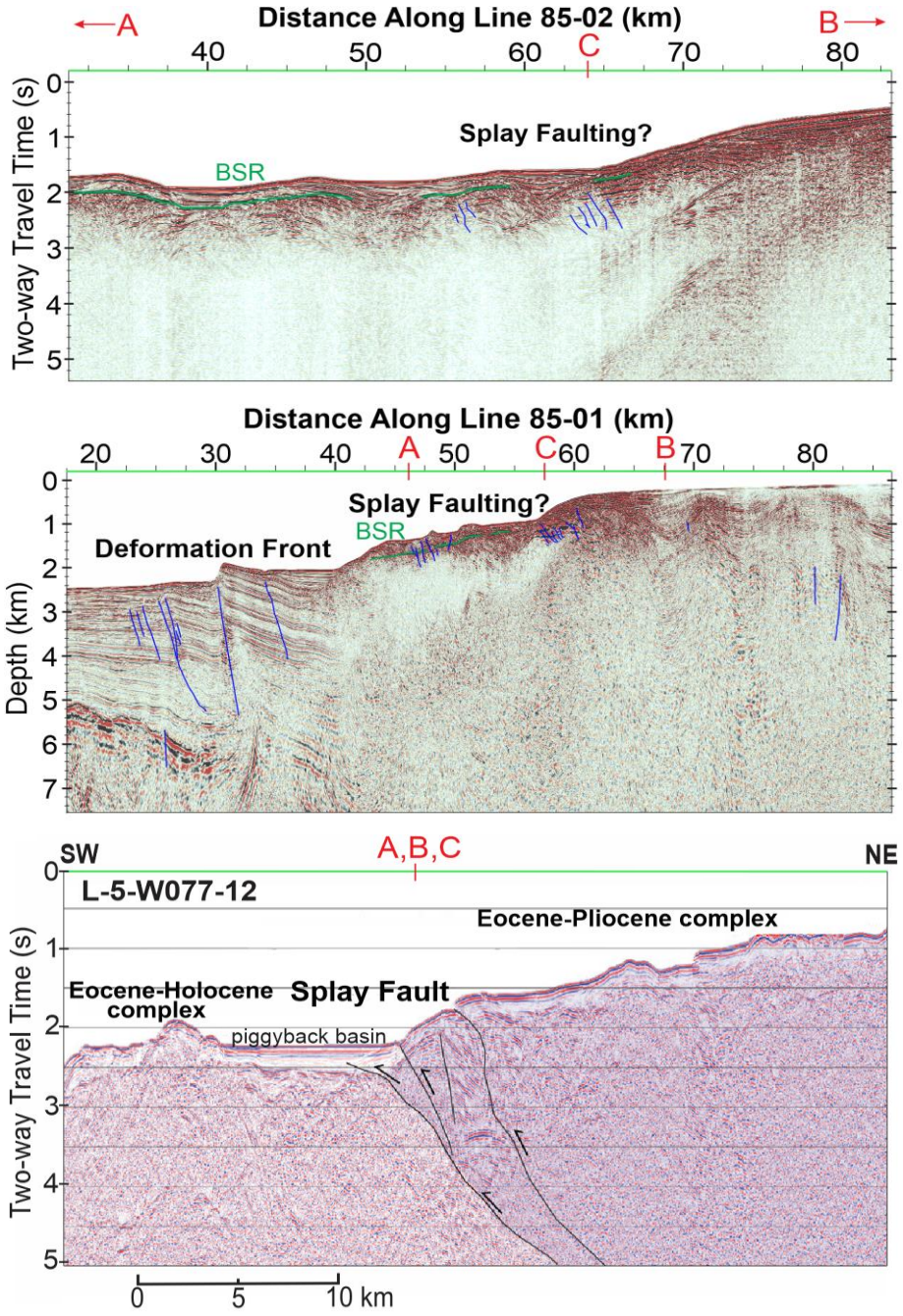

Figure 3.3. Identifying potential splay faults. Red lines show the locations where model splay A, B and C intersect these lines. Seismic images crossing the Cascadia deformation front (85-01) and potential areas of splay faulting in lines 85-01 (b), 85-02 (a) (Yorath et al., 1988), and L-5-W077-12 (Priest et al., 2010). The locations of these lines are shown in Figure 3.1d.

3.2. Cascadia 1700 Megathrust Earthquake Rupture Scenarios

3.2.1. Summary of Previous 1700 Dislocation Modelling

Through the analysis of microfossils found within coastal marshes, coastal subsidence can be estimated to provide information on the megathrust rupture that caused the subsidence. Coastal stratigraphy and foraminiferal assemblages record relative sea-level (RSL) rise due to coseismic subsidence along the Cascadia subduction zone. Sudden changes in RSL, assumed

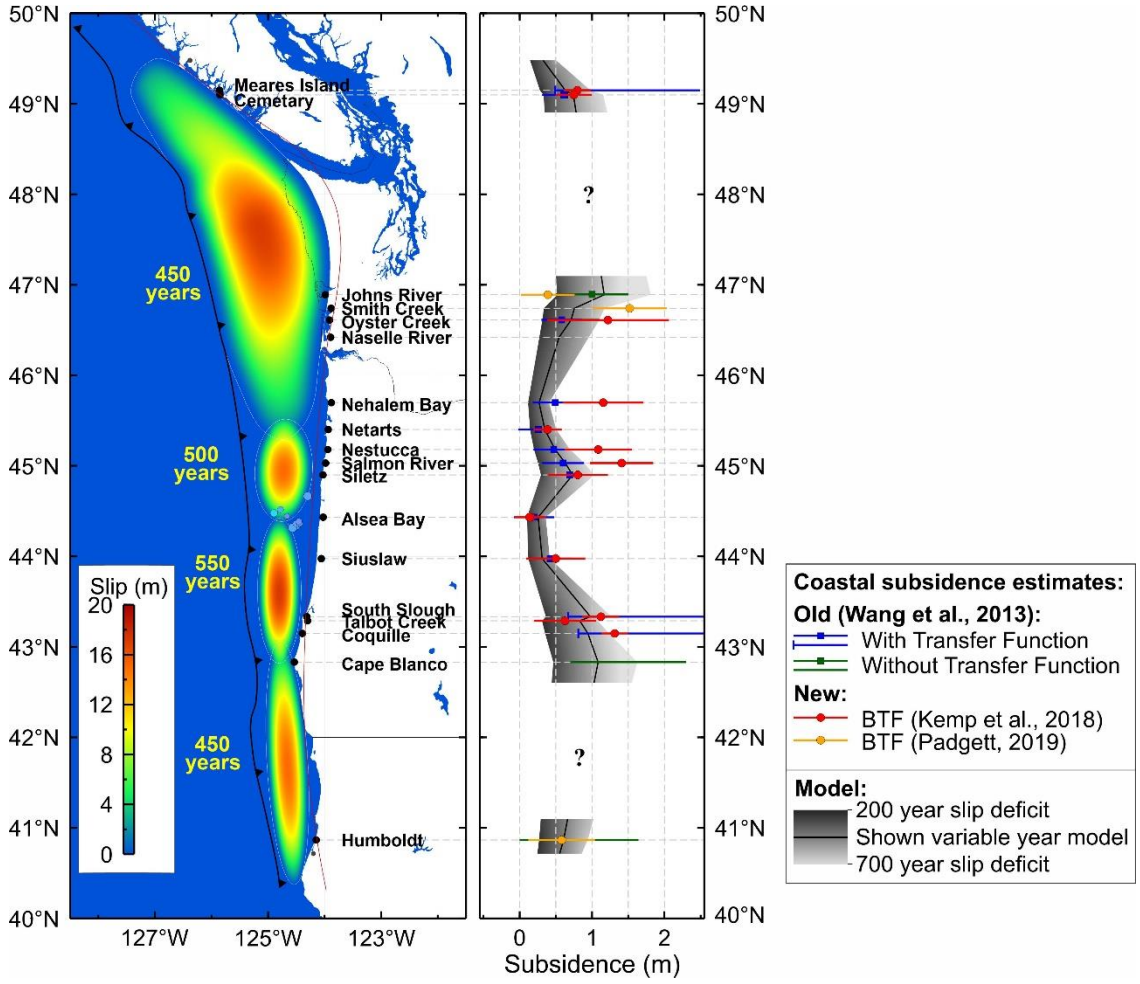

Figure 3.4. Preferred model of Wang et al. (2013) for the 1700 earthquake, with some slight modifications. Modifications include an improved megathrust geometry (Figure 3.2) and an updated deformation front trace, which slightly alters the northern patch shape. Light blue circles west of Alsea Bay are earthquakes *Mw* > 3 from ANSS that are suspected to have been caused by a subducting seamount. Grey shaded zone in the right panel shows the variability of coastal subsidence by changing the peak slip deficit recovered by the assumed rupture between 200-700 years. Yellow text: Peak slip deficit for each patch.

to reflect coseismic coastal subsidence, are estimated with transfer functions that have been calibrated using present day (surface) foraminifera and corresponding elevation measurements. Wang et al. (2013) provided a suite of scenarios that fit the then available microfossil-constrained coastal subsidence estimates. They found that along-strike heterogeneous rupture was required to explain the subsidence estimates (Figure 3.4). Since that time, new statistical techniques have been employed to better constrain the existing subsidence estimates, and additional estimates have been obtained at a few new locations by our collaborators, the research group at the University of Rhode Island.

3.2.2. Implications from the Revision of Coastal Subsidence Estimates

Through improvements in data processing and transfer function analysis, Kemp et al. (2018) provided a revision of the subsidence estimates that had been employed by Wang et al. (2013). These new results confirmed the along-strike variations in coastal subsidence as observed before. However, the along-strike variations have become much more pronounced. Further work with increased sampling between 46°N to 47°N revealed significant along-strike variations in estimated coseismic coastal subsidence during the 1700 earthquake (Padgett, 2019, personal communication).

For this study, 16 foraminiferal Bayesian transfer function (BTF) estimates are available, of which 13 are from Kemp et al. (2018) and three are prelimary estimates from Padgett (2019) (Table 3.1). Of the three sites that have new prelimary estimates from Pagett (2019), two have older published estimates which I also include in the dataset for easy comparison. Also, the old esimate from the Cape Blanco site (Sixes River) is used where no BTF-assisted foraminiferal analyses are presently available. Kelsey et al. (1998) estimated that due to observed changes in diatom assemblages the subsidence at the Sixes River site was at least 0.7 m and no more than

2.2 m.

Table 3.1. Paleoseismic estimates used in this study.

Site	Latitude (°N)	Longitude (°W)	Subsidence (m)	Standard deviation (m)	Method[a]	Reference[b]
Vancouver Island						
Meares Island	49.1489	-125.8591	0.798	± 0.186	BTF	Kemp et al. (2018)
Cemetery	49.0977	-125.8509	0.747	± 0.250		
Washington						
Johns River	46.89	-123.988	1.00	± 0.50	Microfossil without TF	Shennan et al. (1996)
Johns River	46.89	-123.988	0.39	± 0.37	BTF	preliminary estimate from Padgett (2019)
Smith Creek	46.74	-123.885	1.52	± 0.51		
Niawiakum/Oyster Creek	46.61	-123.912	1.220	± 0.841	BTF	Kemp et al. (2018)
Oregon						
Nehalem	45.6982	-123.8811	1.155	± 0.554	BTF	Kemp et al. (2018)
Netarts Bay	45.4010	-123.9366	0.386	± 0.195		
Nestucca	45.1799	-123.9429	1.085	± 0.462		
Salmon	45.0301	-123.9814	1.409	± 0.435		
Siletz	44.8989	-124.0302	0.803	± 0.416		
Alsea Bay	44.4325	-124.0267	0.136	± 0.207		
Siuslaw	43.9752	-124.0583	0.499	± 0.407		
South Slough	43.3326	-124.3150	1.122	± 0.254		
Talbot Creek	43.288	-124.30	0.628	± 0.426		
Coquille	43.1485	-124.3925	1.313	± 0.182		
Sixes River/Cape Blanco	42.8310	-124.5350	0.7-2.2	Not applicable	Diatoms without BTF	Kelsey et al. (1998)
California						
Humboldt Bay	40.8660	-124.1492	0-1.64	Not applicable	Diatoms without TF	Pritchard (2004)
Humboldt Bay	40.8660	-124.1492	0.58	± 0.46	BTF	preliminary estimate from Padgett (2019)

[a] BTF: foraminiferal Bayesian transfer function
[b] Reference provided is for the (re-)analysis of the data with the specified method. Please refer to these references to find the original data sources.

Countless 1700 rupture models of variable complexity can be created to fit the coastal subsidence data. Given the sparsity of the coastal subsidence data and having large errors, preference is given to simpler models. Here I present six different possible scenarios. Just like previous models provided by Wang et al (2013), a bell-shaped slip distribution is assigned in the margin-normal direction with equations 2.1 and 2.2 as discussed in section 2.4. In most of the slip patches of Wang et al. (2013), slip was scaled in the strike direction of elliptical patches by

assigning $w_1 = w_2$ as discussed in section 2.4. In this work, most of the patches are scaled in the same manner, but for some patches the slip is not scaled with width until closer to the patch termini.

For the simplest case, I slightly modify the four slip patches in Wang et al.'s (2013) preferred model to better fit the new subsidence estimate results (C-P-B-4b). The southern two patches are only slightly modified in their orientations and sizes, but the 45°N patch is significantly shortened in the strike direction and widened in the dip direction to have deeper slip. The peanut-shaped northern-most patch was modified to have more slip extend southward to produce a significant amount of subsidence at Nehalem Bay (~45.7°N) (Figure 3.5). The new subsidence estimate at this site provided by Kemp et al. (2018) is more than doubled from previous estimates used by Wang et al. (2013) (Figure 3.4).

To demonstrate that the shallow rupture style far offshore has very little effect on coastal subsidence, I created both splay faulting (C-P-Sb-4) and trench-breaching (C-P-T-4) rupture scenarios. Both of these models are designed in the same fashion as the splay faulting scenarios described in section 3.3.2. However, for the trench-breaching scenario the updip half of the assigned bell-shaped slip is stretched by a factor of two. With these modifications on rupture style, it is clear that the shallow megathrust rupture style plays an insignificant role in coastal subsidence (Figure 3.5).

In attempts to account for some along-strike variations in coastal subsidence between 46°N to 47°N determined by Padgett (2019) including a lesser amount of subsidence at Naselle River (46.42°N, -123.89°W) (J. Padgett, 2019, personal communication), I created a five-patch buried rupture model (C-P-B-5). For model testing purposes I created an unrealistic scenario where full-margin rupture with some along-strike variability in the deep downdip slip that can also fit the

coastal subsidence data (C-P-T-1) (Figure 3.6). A summary of the 1700 rupture models is given by Table 3.2.

Stress drop of each of the scenarios is calculated, and it is found that some of the small patches with high slip result in quite large $\overline{\Delta\sigma}$ values (Figure 3.5). Further discussion about these $\Delta\sigma$ results will be given in section 3.4.

Table 3.2. Summary of 1700 paleoseismic rupture scenarios.

Model	Figure	Peak Slip[a] (years)	Moment[b] (N·m)	*Mw*
~Wang et al. (2013) preferred (C-P-B-4a)	3.4	450,500,550,450	2.675e+22	8.88
Buried rupture four patch (C-P-B-4b)	3.5a	450,550,500,450	2.651e+22	8.88
Buried rupture five patch (C-P-B-5)	3.5b	450,550,550,500,450	2.405e+22	8.85
Splay faulting four patch (C-P-Sb-4)	3.5c	450,550,500,450	2.166e+22	8.82
Trench-breaching four patch (C-P-T-4)	3.5d	450,550,500,450	3.408e+22	8.96
Full-margin trench-breaching with varible downdip rupture (C-P-T-1)	3.6	500	5.196e+22	9.08

[a]Slip is measured in terms of recovered slip deficit accumulated over a time period. For multiple high-slip patches, the peak values are listed from north to south.
[b]Moment is calculated using a rigidity of 40 GPa.

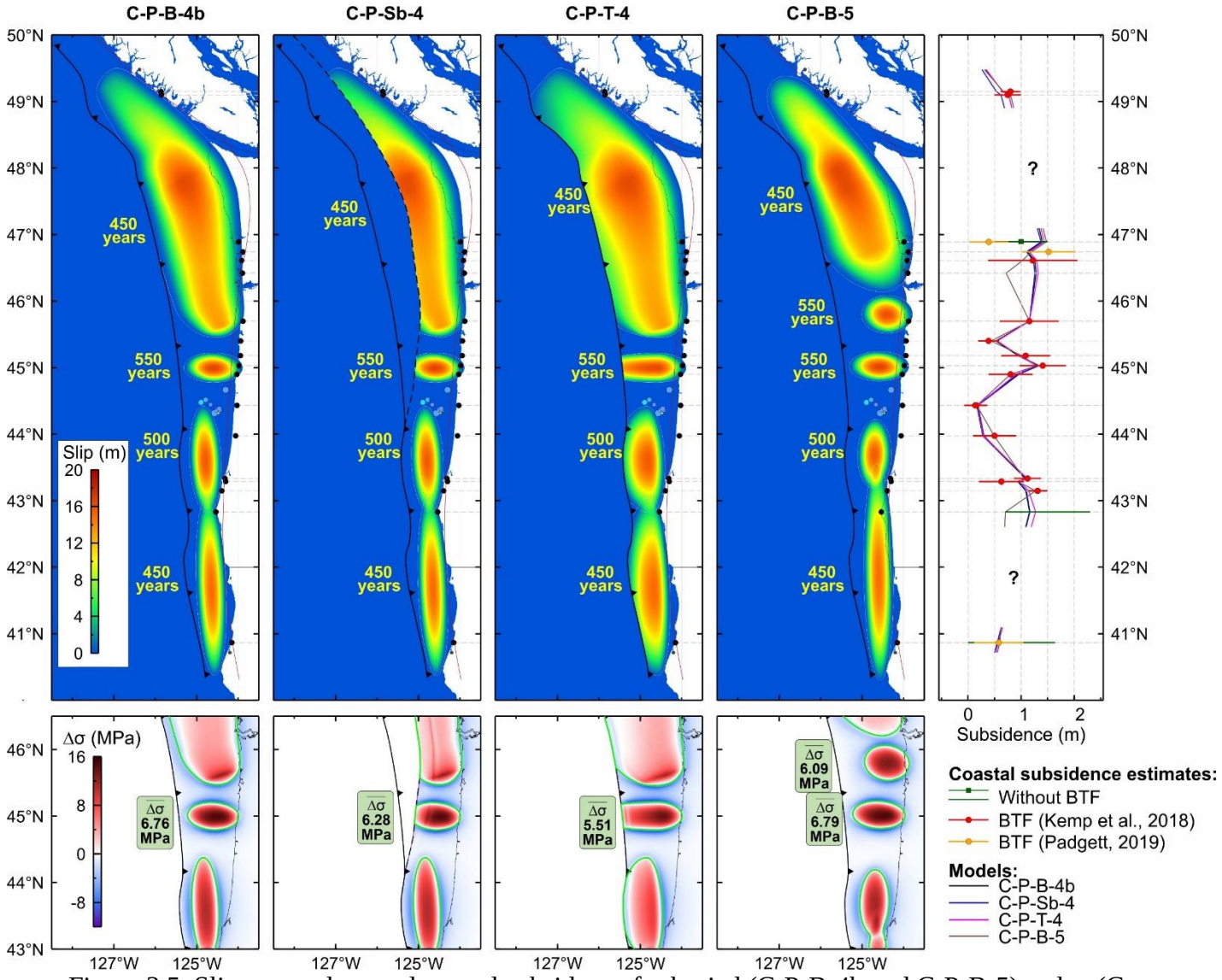

Figure 3.5. Slip, stress drop and coastal subsidence for buried (C-P-B-4b and C-P-B-5), splay (C-P-Sb-4), and trench-breaching (C-P-T-4) heterogeneous rupture scenarios that approximately fit the coastal subsidence estimates for the 1700 Cascadia earthquake. Stress drop (lower panels) was calculated with a rigidity of 40 GPa and the $\overline{\Delta\sigma}$ within the 10% of peak slip contour lines (green lines) is given for some of the small slip patches. Blue circles: Earthquakes *Mw* > 3 from ANSS between 44°N and 45°N. Green lines in stress drop figures show the 10% of peak slip contour that was used to caluclate $\overline{\Delta\sigma}$. Yellow text: Peak slip deficit for each patch. Black dots in slip distribution panels and grey dashed lines in all upper panels correspond to locations where uplift is calculated. These locations include all locations where a subsidence estimate is provided and the Naselle River site (~46.5°N).

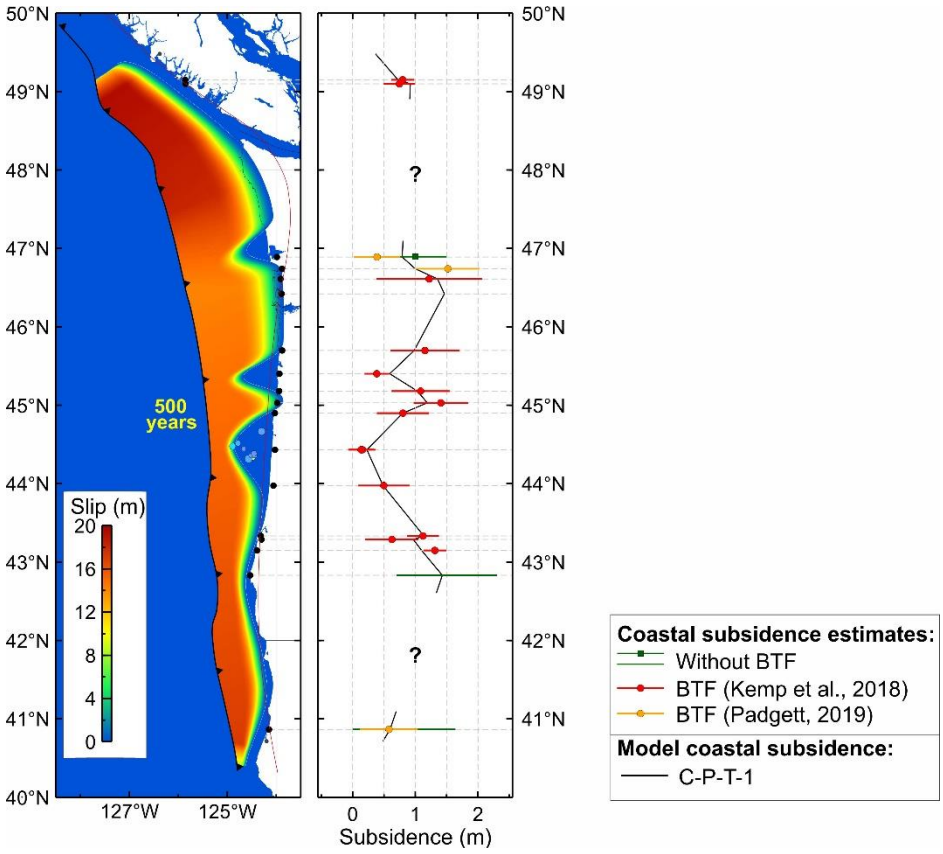

Figure 3.6. Slip and coastal subsidence for geologically unrealistic full-margin rupture that has downdip slip variability in the strike direction (C-P-T-1). A 500-year peak slip deficit is used in this model.

3.3. Cascadia Tsunami Source Scenarios

Types of tsunami sources considered for Cascadia include full-margin buried rupture, splay faulting rupture, and trench-breaching rupture (Figure 1.2). Because of the thick sediment on the incoming plate and the buried trench, the Cascadia trench-breaching rupture is assumed to break the seafloor by activating a frontal thrust (Figure 1.2c). Gao et al. (2018) focused on megathrust tsunami sources in northernmost Cascadia and did not scrutinize the published megathrust geometry in southern Cascadia. All the northern Cascadia models (with or without the Explorer segment) except for the newly added splay-fault C scenario (Figures 3.1 and 3.3) have already been published in Gao et al. (2018) and will not be repeated here. As explained in section 3.1 above, I have now updated the megathrust geometry in southern Cascadia. Therefore, in this

chapter I only present the updated full-margin rupture scenarios (Table 3.3) and the case of independent rupture of a short segment in southernmost Cascadia (section 3.3.4). The six full-margin scenarios summarized in Table 3.3 are constructed in the same manner as the full-margin rupture scenarios in Gao et al. (2018), except for the aforementioned modifications to the megathrust geometry and the slip distribution for the southernmost postion of Cascadia. For this work the downdip rupture bound for southern Cascadia is slightly different than that of Gao et al. (2018).

Table 3.3. Summary of full-margin Cascadia rupture scenarios for tsunami hazard assessment. Model names in parentheses show what the equivalent models would be called with the naming convention of Gao et al. (2018).

Full-Margin Cascadia Model	Figures	Moment[a] (N·m)	*Mw*	Average stress drop within 10% of peak slip contour (MPa)[a]
Buried Rupture C-B-F (B-Whole)	3.7 & 3.8	4.866E+22	9.06	3.23
Splay Faulting Rupture A C-Sa-F (S-A-Whole)	3.9a & 3.10	4.347E+22	9.03	3.36
Splay Faulting Rupture B C-Sb-F (S-B-Whole)	3.9c & 3.10	3.916E+22	8.99	3.27
Splay Faulting Rupture C C-Sc-F (S-C-Whole)	3.9b & 3.10	4.198E+22	9.02	3.35
Trench-breaching Rupture 50% C-T50-F (T-50-Whole)	3.11a & 3.12	5.723E+22	9.11	2.51
Trench-breaching Rupture 100% C-T100-F (T-100-Whole)	3.11b & 3.12	6.446E+22	9.14	2.41

[a]Moment and stress drop are calculated using a rigidity of 40 GPa.

For these Cascadia tsunami source scenarios, I use well-defined parameters to specify the rupture limits, convergence rate, and slip deficit. As in previous studies (Hyndman and Wang, 1995; Wang et al., 2003; Gao, 2016; Gao et al., 2018), the updip coseismic rupture limit is assigned to be along the deformation front. The downdip coseismic rupture limit for the Explorer plate segment of Cascadia is based on thermal modelling of Gao et al. (2017). For the rest of

Cascadia, coseismic rupture is allowed to extend halfway through the "effective transition zone" (ETZ) defined by Wang et al. (2003). Along-strike rupture bounds for full-margin rupture are defined by the Mendocino triple junction and Brooks Peninsula, which is believed to be the northern extent of Explorer plate subduction. Peak coseismic slip is assigned in the same fashion as for the interseismic megathrust locking model CAS3D-2 (Wang et al., 2003) but in the opposite direction. Wang et al. (2003) used PA-NA (DeMets and Dixon, 1999) and JDF-PA (DeMets et al., 1994) Euler poles to define a JDF-NA Euler pole for northern Cascadia. By taking into consideration the Oregon coastal block rotation relative to NA (forearc-NA) (Wells and Simpson, 2001), they defined a JDF-forearc Euler pole for southern Cascadia (south of 46.5°N). They assumed a linear transition between the northern and southern regions. For the results shown here, a peak slip recovering 500 years of slip deficit is used, given that the average reoccurrence interval for large Cascadia megathrust earthquakes is approximately 500 years (Goldfinger et al., 2012). Due to the usage of Euler poles, the slip direction varies along-strike. The slip distribution within the assumed rupture patch is then assigned by using the peak cosiemic slip with the slip shaping functions discussed in section 2.4. The deformation and stress results are proportional to slip; therefore, any of the scenarios presented in the following sections can be linearly scaled for any other slip deficits.

3.3.1. Cascadia Full-margin Buried Rupture Scenario

For Cascadia buried rupture scenarios, a symmetric bell-shaped slip distribution is assigned with equations 2.1 and 2.2. Recall the along-strike scaling relationship $(w/w_k)^2$, where w_k is an unscaled, reference local width at some distance from either slip patch terminus (north or south). This along-strike relationship is used to scale the slip within ~40 km of the northern and southern slip patch termini. Figures 3.7 and 3.8 show how the assigned bell-shaped slip distribution varies

with the width of the slip patch width along-strike and how peak slip changes along-strike.

The calculated uplift for the full-margin buried rupture scenario (Figure 3.7) shows a smooth distribution of coastal subsidence and seafloor uplift. The wavelength of the deformation variation in the margin-normal direction shortens with the narrowing of the rupture width. The amplitude of the vertical deformation scales with the magnitude of the slip. Profile 2 in Figure 3.8 shows how a lower peak slip results in a smaller uplift compared to profiles 1 and 3. Chapter 6 will provide an example of Cascadia tsunami generation by the buried rupture.

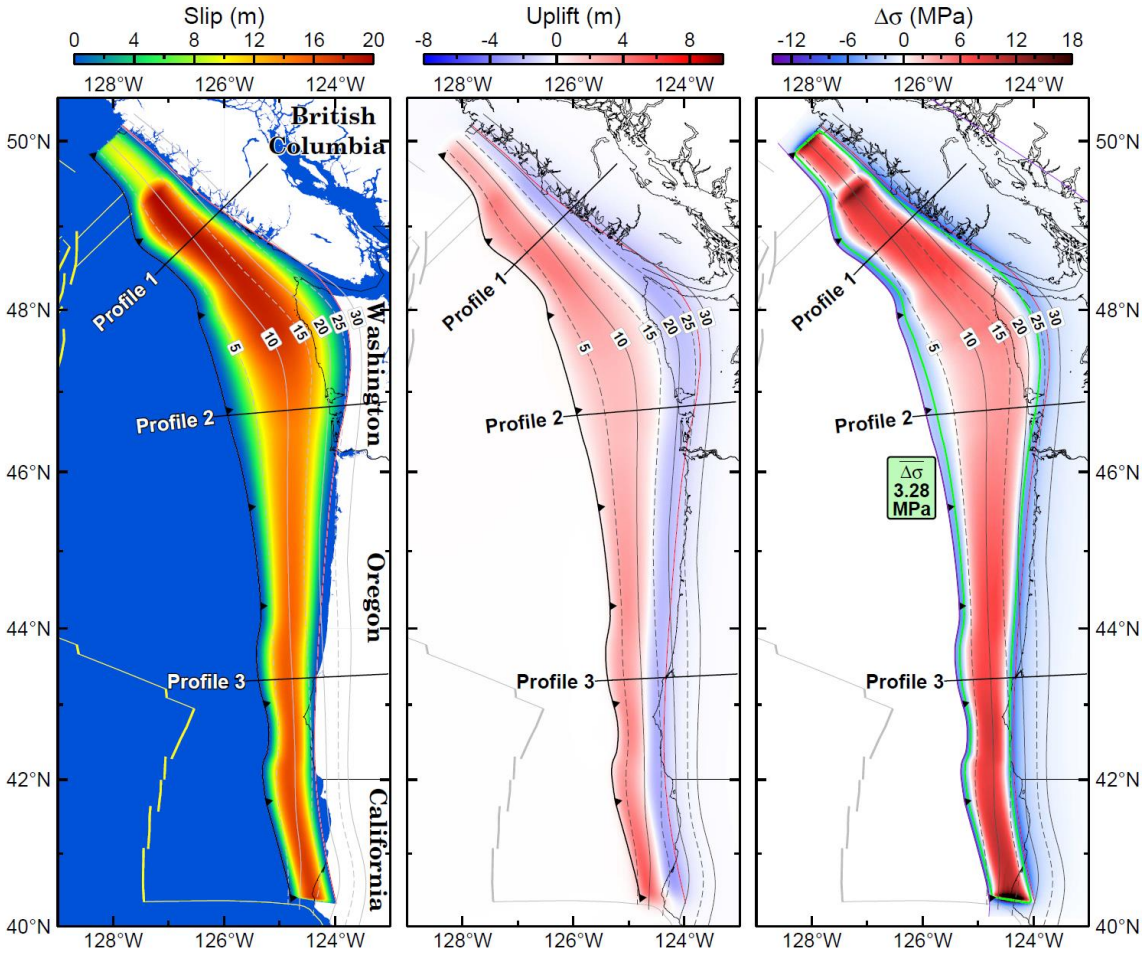

Figure 3.7. Full-margin Cascadia buried rupture model (C-B-F). From left to right: slip, uplift, and stress drop. Red line: Downdip rupture bound as defined in section 3.3. Green line in stress drop figure is the contour of 10% peak slip within which $\overline{\Delta\sigma}$ is calculated. Anomalously high $\Delta\sigma$ at ~40.4°N is the result of a sudden termination of slip and should be considered a model artefact. There is great uncertainty in how this slip will terminate in the south.

Fault stress drop ($\Delta\sigma$) changes with slip magnitude and slip gradient. Along a margin-normal profile, $\Delta\sigma$ fluctuates from a low near the deformation front, to a high where the peak slip occurs, and back to a low as the slip begins to taper to zero at a great depth (Figure 3.8). The symmetric slip distribution gives rise to an asymmetric $\Delta\sigma$ distribution, most pronounced for profile 2, because the shallower depth of the trench-ward half of the rupture zone and the resultant lower stiffness allows the same slip to occur with a smaller $\Delta\sigma$. Fluctuations in $\Delta\sigma$ are also observed along-strike at the Nootka fault and both northern and southern patch termini due to rapid changes in slip (Figure 3.7), some of which may be the artefact of too abrupt termination of the assigned slip. Further $\Delta\sigma$ discussion is found in section 3.4.

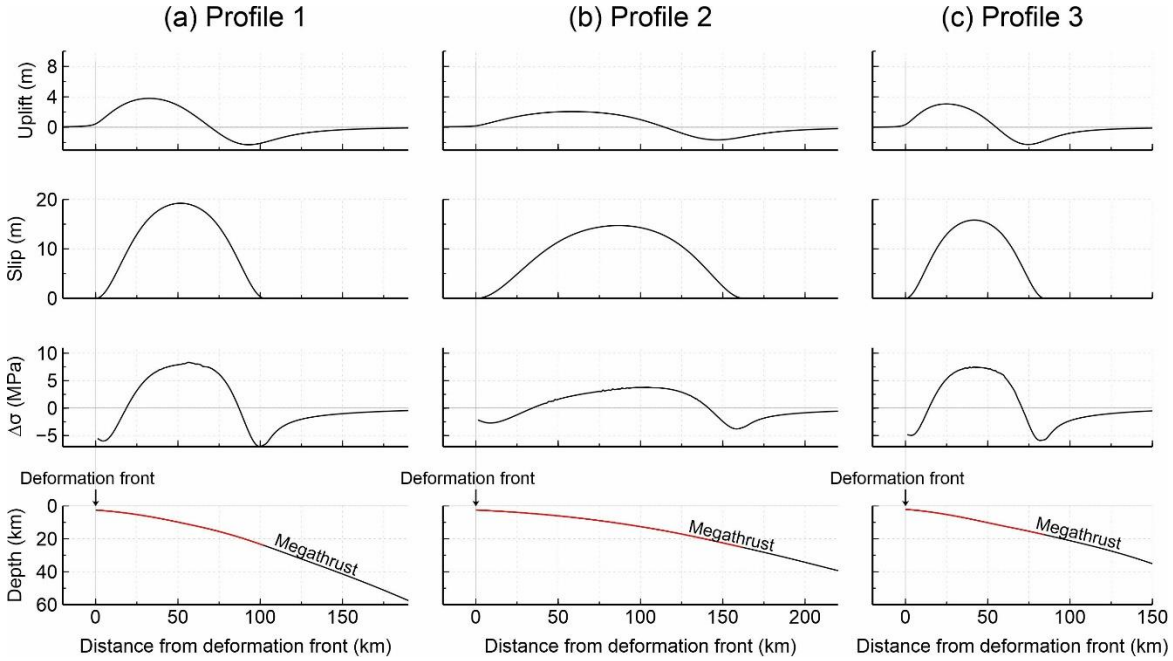

Figure 3.8. Fault slip, surface deformation, and stress drop on the megathrust along the three profiles shown in Figure 3.7. Cascadia full-margin buried rupture models (C-B-F) seafloor uplift, slip, stress drop on the fault and fault geometry shown for each profile from top panels to bottom panels, respectively. Red line in bottom panels shows the rupture zone.

3.3.2. Cascadia Full-margin Splay Faulting Rupture Scenarios

All three splay-fault scenarios are based on a northward extrapolation of the splay fault off the coast of Oregon proposed by Priest et al. (2010). Splay A and B extrapolations were proposed by Gao (2016) to be end-member scenarios for offshore Vancouver Island where splay B is simply extrapolated along the continental shelf edge, and splay A merges with the deformation front. As explained in section 3.1 above, the new splay C (Figure 3.3) lies between splays A and B. For simplicity, the buried rupture slip distribution is mapped onto, and truncated by the trace of the splay fault. This allows the slip to breach the seafloor east of the deformation front (Figures 3.9 and 3.10).

The resulting uplift shows the same distribution as the buried rupture in southern Cascadia where there is no splay fault, as well as for a small segment of northern Cascadia for C-Sa-F and C-Sc-F models since the splay fault trace in these scenarios joins the deformation front at ~48.7°N and ~49.4°N, respectively. Where the slip breaches the seafloor, the resulting uplift becomes much greater than the buried rupture case (Figures 3.9 and 3.10) and hence significantly amplifies the tsunami it can produce. A possible tsunami generated by rupture of this type is discussed in Chapter 6.

The $\Delta\sigma$ results are also similar to those of the buried rupture scenario for the southern part of the model. In the north, for the very shallow portion of the fault, $\Delta\sigma$ fluctuations occur due to changes in fault surface geometry (Figure 3.10). The splay fault peels off the megathrust relatively abruptly, and the geometrical irregularity results in stress increase or decrease along the fault. This should not necessarily be considered a model artefact because real splay faults may take off just as abruptly depending on the geological process leading to the formation of the splay. Further $\Delta\sigma$ discussion is found in section 3.4.

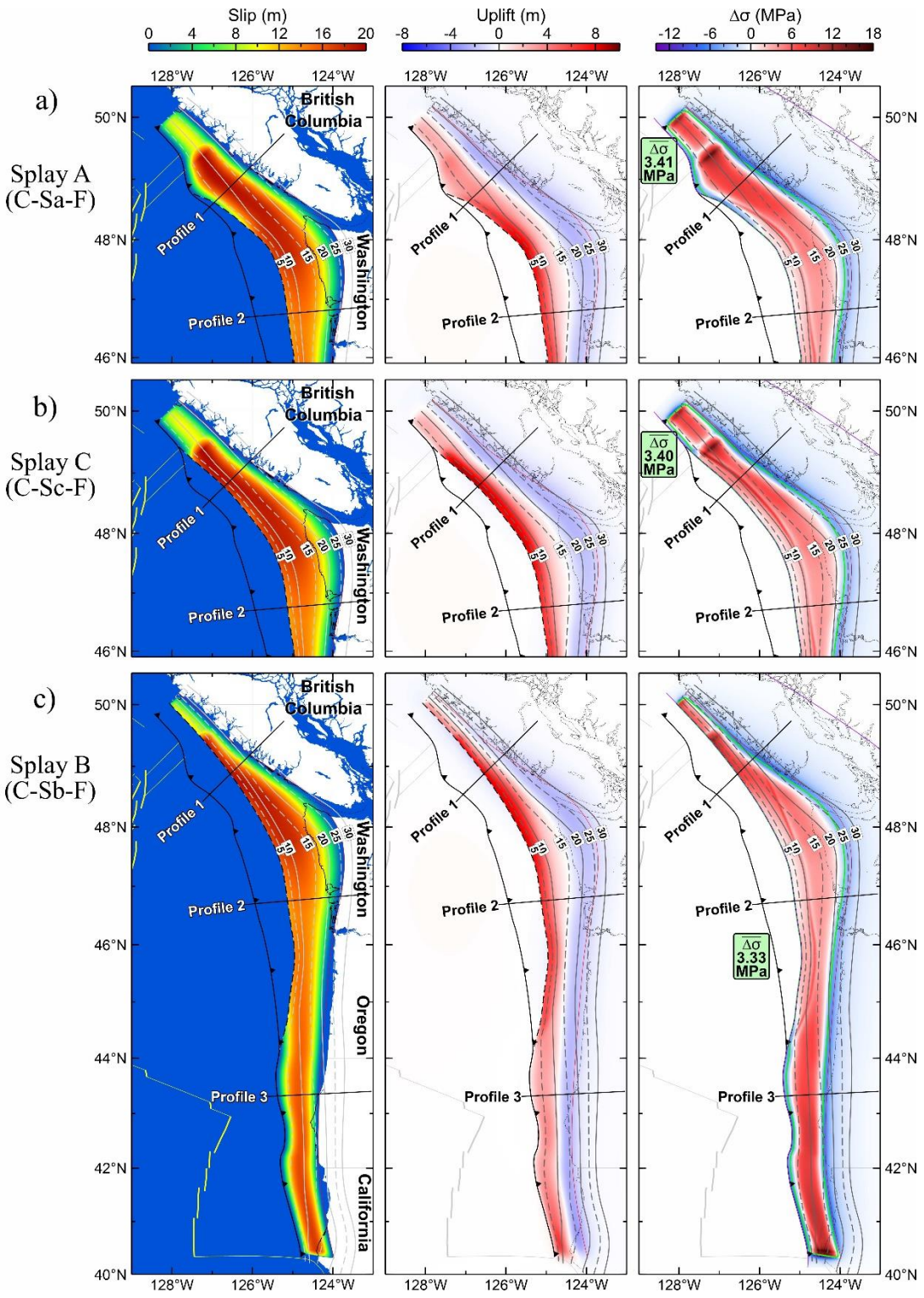

Figure 3.9. Full-margin Cascadia splay faulting rupture models (C-Sa-F, C-Sb-F, and C-Sc-F). From left to right in each row: slip, uplift, and stress drop. The three splay scenarios yield the same results for southern Cascadia, hence the truncated figures for Splay A and C. Red line: Downdip rupture bound as defined in section 3.3. Green line in stress drop figure is the contour of 10% peak slip within which $\overline{\Delta\sigma}$ is calculated. Anomalously high $\Delta\sigma$ at ~40.4°N is the result of a sudden termination of slip and should be considered a model artefact. There is great uncertainty in how this slip will terminate in the south.

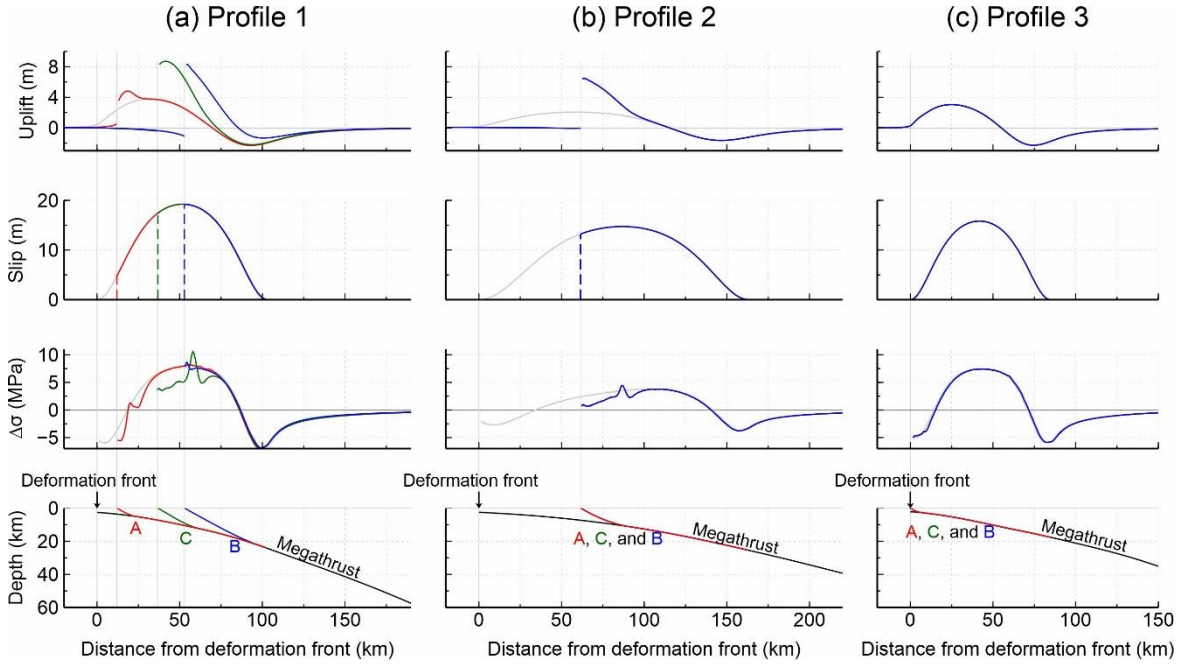

Figure 3.10. Fault slip, surface deformation, and stress drop on the megathrust along the three profiles shown in 3.9. Cascadia full-margin splay faulting models C-Sa-F (red), C-Sb-F (blue), and C-Sc-F (green) slip and rupture zones are shown in the second and bottom panel rows, respectively. Model calculated seafloor uplift and stress drop on the fault are shown in the top and third panel rows, respectively. Grey line in top three rows shows buried rupture (C-B-F) results from Figure 3.8.

3.3.3. Cascadia Full-margin Frontal-Thrust Rupture Scenarios

For Cascadia trench-breaching rupture scenarios, the fault slip downdip of the location of the peak slip has the same bell-shaped distribution as the buried and splay scenarios. In the updip portion, the slip is assigned to either maintain the peak slip to the deformation front (C-T100) or gradationally decrease to 50% of the peak slip at the deformation front (C-T50) (Section 2.4, Figure 2.3). These two contrasting scenarios are constructed in consideration of the uncertainties in the degree of coseismic strengthening (Hu and Wang, 2008; Wang and He, 2008) or dynamic weakening (Di Toro et al., 2011; Noda and Lapusta, 2013) of the shallow portion of the megathrust. More coseismic slip reaching the deformation front means a lower degree of coseismic strengthening to stop the rupture or a higher degree of dynamic weakening to facilitate rupture, and vice versa.

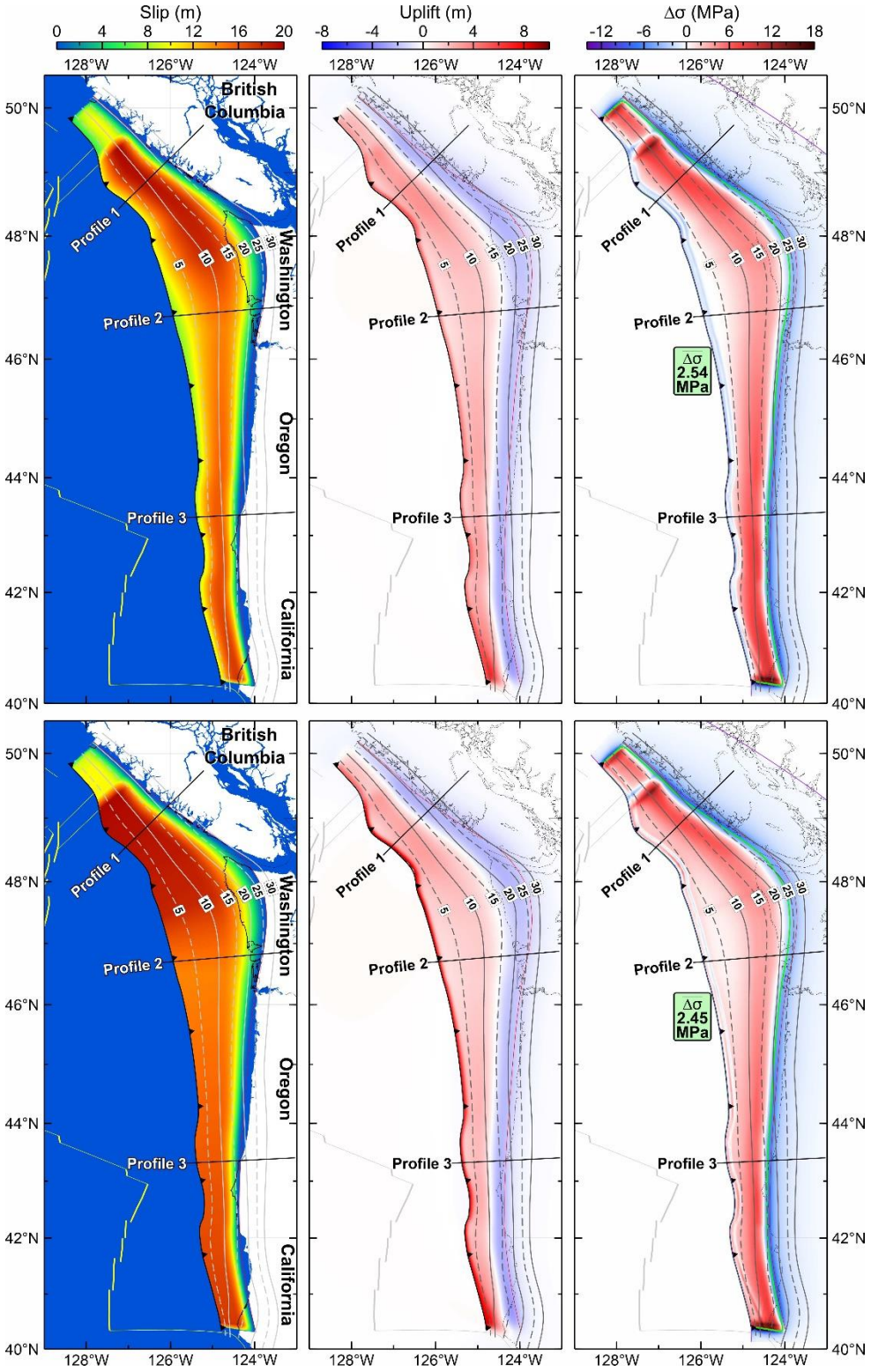

Figure 3.11. Full-margin Cascadia trench-breaching rupture models (C-T50-F and C-T100-F). From left to right in each row: slip, uplift, and stress drop. Red line: Downdip rupture bound as defined in section 3.3. Green line in stress drop figure is the contour of 10% peak slip within which $\overline{\Delta\sigma}$ is calculated. Anomalously high $\Delta\sigma$ at ~40.4°N is the result of a sudden termination of slip and should be considered a model artefact. There is great uncertainty in how this slip will terminate in the south.

Coastal subsidence is similar to that seen for buried and splay scenarios. Logically, uplift near the deformation front is magnified by the trench-breaching rupture where more slip occurs at shallow depths along a more steeply dipping fault (Figures 3.11 and 3.12). Just landward of this large amount of uplift at the frontal thrust, less uplift occurs compared to the buried rupture scenarios. A lesser decrease in slip from the peak slip to the deformation front results in less horizontal shortening of the upper plate material and hence less vertical expansion. The lesser uplift in this area effectively offsets the effect of the greater uplift at the deformation front in tsunami wave generation (as discussed in Chapter 6).

Understandably, the overall $\Delta\sigma$ distribution is less for the updip portion of the fault due to a lower margin-normal slip gradient compared to that of the buried rupture. Stress drop results show a lower peak $\Delta\sigma$ compared to that of the buried rupture (Figure 3.12). The oscillating $\Delta\sigma$

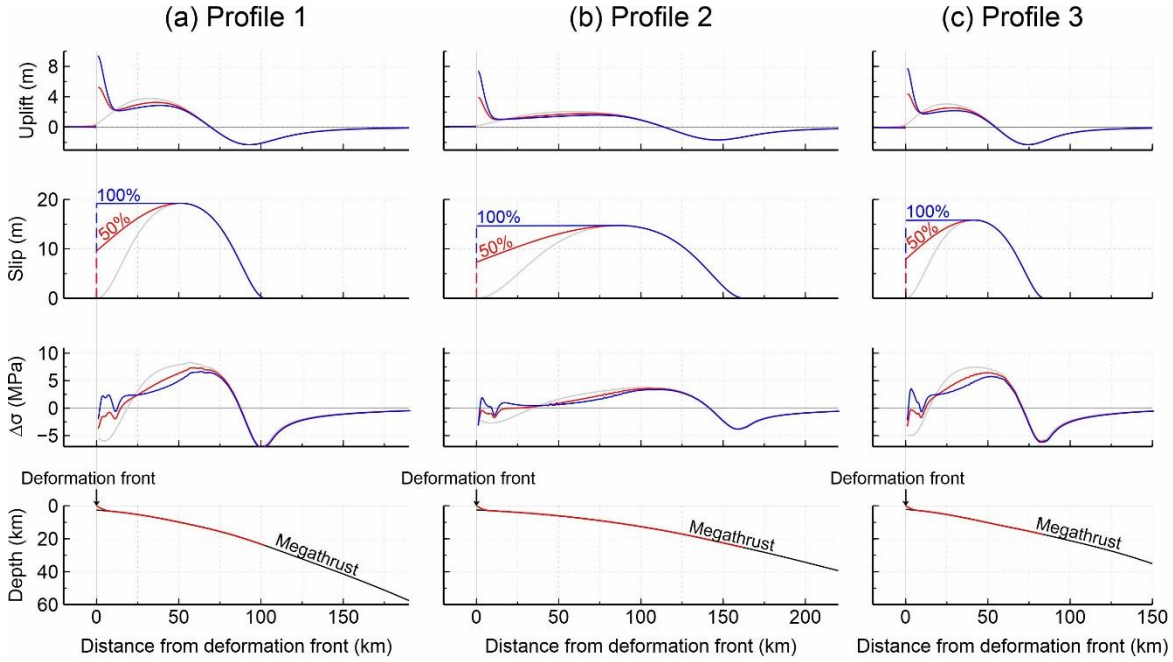

Figure 3.12. Fault slip, surface deformation, and stress drop on the megathrust along the three profiles shown in Figure 3.12. Cascadia full-margin trench-breaching models C-T50-F (red) and C-T100-F (blue) seafloor uplift, slip, stress drop on the fault, and fault geometry shown for each profile from top panels to bottom panels, respectively. Grey line in top three panel rows shows buried rupture (C-B-F) results from Figure 3.8. Red line in bottom panels shows the rupture zone for both trench-breaching scenarios.

feature discussed in the splay scenario section 3.2.2 caused by the fault geometry changes also occurs for these trench-breaching scenarios. Further $\Delta\sigma$ discussion is found in section 3.4.

3.3.4. The Case of a Shorter Rupture in Southern Cascadia

From observations of real earthquakes, it is apparent that segmented rupture is more likely to happen for certain subduction zones. For the Cascadia subduction zone, the most obvious candidate for a segmentation boundary is the Nootka fault (Figure 1.1). Gao et al. (2018) constructed various rupture scenarios based on whether or not the Explorer segment ruptured together with the rest of the Cascadia megathrust. In this work, I create rupture scenarios for a southern segment of Cascadia with the northern termination defined by suspected subducting seamounts offshore of Alsea Bay (~ 44.4°N) (Wang and Tréhu, 2016). This candidate

segmentation boundary is the next most obvious after the Nootka fault boundary. It correlates well with paleoseismic models generated to fit coastal subsidence data for the 1700 Cascadia megathrust earthquake (Figure 3.5), a latitudinal boundary of episodic tremor and slip (ETS) (Brudzinski and Allen, 2007), and one of the megathrust rupture termination boundaries proposed through turbidite analysis (northern boundary for segment C' rupture in Goldfinger et al. (2017)).

Turbidite studies (Goldfinger et al., 2012; 2017; Witter et al., 2012; Scholz, 2014) indicate there may be other boundaries along the Cascadia margin, with a tendency for more southerly segments to rupture more frequently but with smaller slip in each event. These other suspected rupture segmentation boundaries overall have a smaller amount of evidence compared to the two mentioned above that have either small earthquakes occurring on the décollement due to geometric irregularities (off Alsea Bay) or being associated with the extension of a very active transform fault (Nootka Fault). I have constructed three southern Cascadia rupture (SCR) scenarios including one buried rupture scenario and two trench-breaching scenarios (Table 3.4).

Table 3.4. Summary of southern Cascadia rupture scenarios for tsunami hazard assessment.

Southern Cascadia Model	Figure	Moment[a] (N·m)	*Mw*	Average stress drop within 10% of peak slip contour (MPa)[a]
Buried Rupture (C-B-S)	3.13a	1.253E+22	8.66	4.66
Trench-breaching Rupture 50% (C-T50-S)	3.13b	1.501E+22	8.72	3.68
Trench-breaching Rupture 100% (C-T100-S)	3.13c	1.697E+22	8.75	3.49

[a]Moment and $\Delta\sigma$ is calculated using a rigidity of 40 GPa.

The general differences between uplift patterns caused by buried and trench-breaching ruptures observed in northern Cascadia (Figures 3.8, 3.10, and 3.12) holds true also for SCR. For

the trench-breaching SCR, the seafloor uplift near the deformation front is significantly increased over that of the buried rupture just as seen in Northern Cascadia. For SCR, the buried rupture scenario yields a shorter wavelength uplift pattern compared to northern Cascadia due to the narrower fault width (Figure 3.8). Because the peak seafloor uplift is closer to the coast for SCR compared to the north, we could expect faster arrival of tsunami waves after the earthquake in the south.

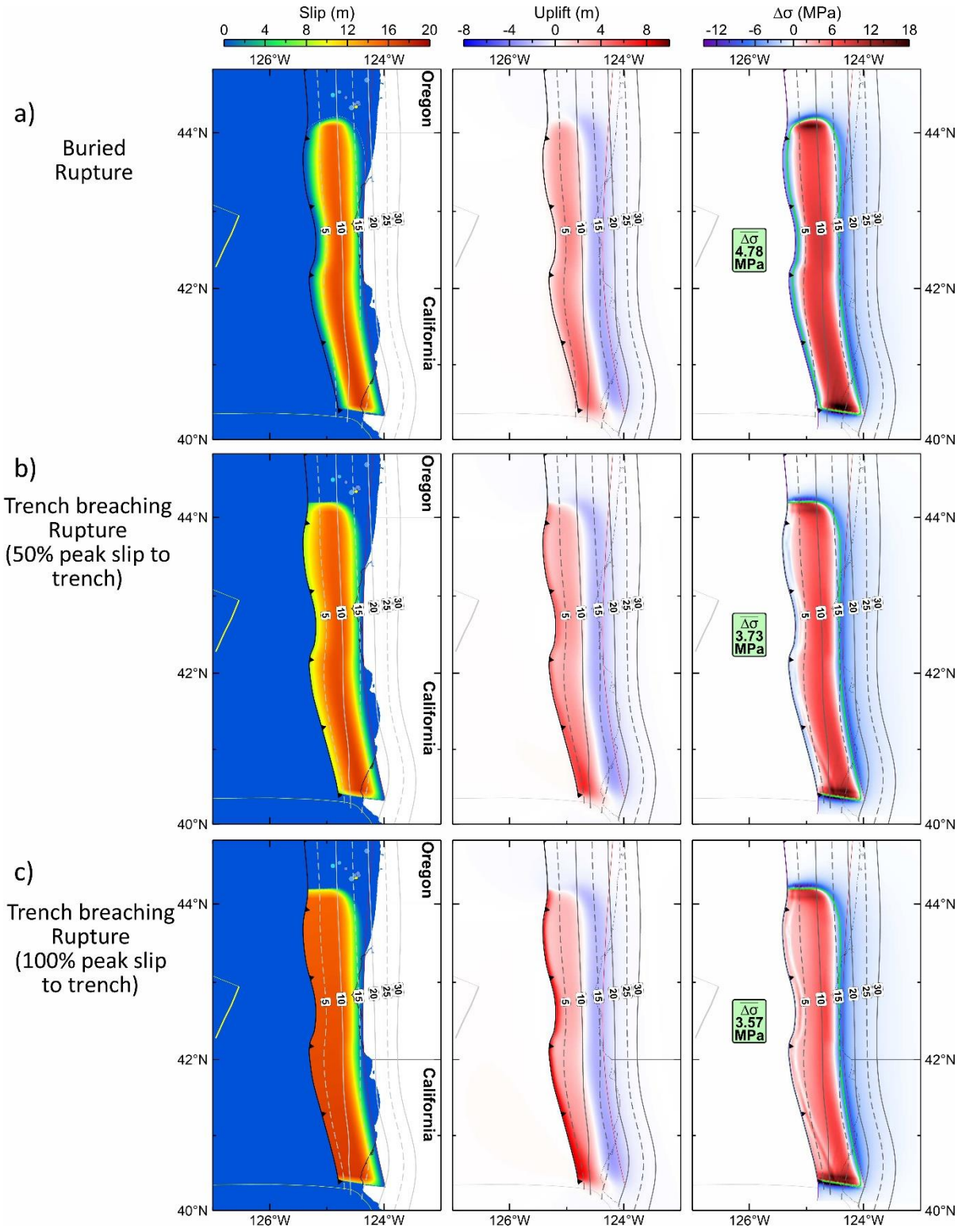

Figure 3.13. Southern Cascadia buried rupture (C-B-S) and trench-breaching rupture models (C-T50-S and C-T100-S) models. From left to right in each row: slip, uplift, and stress drop. Blue circles in slip figures: Earthquakes *Mw* > 3 from ANSS between 44°N and 45°N. Green line in stress drop figure is the contour of 10% peak slip within which $\overline{\Delta\sigma}$ is calculated.

3.4. Cascadia Stress Drop Comparison with Other Subduction Earthquakes

A comparison of stress drop results presented above with those determined for other well-recorded megathrust earthquakes shows that the paleoseismic and tsunami source models for Cascadia presented here are mechanically realistic. Global megathrust earthquakes exhibit $\overline{\Delta\sigma}$ of only a few MPa, with significant heterogeneity within the rupture zone (appendix). The discussed Cascadia models are smooth representations of actual ruptures, so it is reasonable to expect $\overline{\Delta\sigma}$ of a few MPa for full-margin rupture or for any large segment along the margin. The stress distribution results for both the tsunami source and paleoseismic scenarios are comparable in scale to the other megathrust earthquakes in the appendix. However, to fit a paleoseismic model to the new subsidence estimates, a relatively small area with large slip is required off Oregon (45°N patch), resulting in a large local $\Delta\sigma$.

As seen from equation 2.5 in section 2.5, $\overline{\Delta\sigma}$ increases with a decrease in characteristic length of rupture. This relationship is clearly seen when comparing the higher amplitude wavelength $\Delta\sigma$ distribution in the north and south (profiles 1 and 3 in Figures 3.8, 3.10, and 3.12) with the lower amplitude wavelength $\Delta\sigma$ distribution where the rupture width is wider (profile 2).

The $\Delta\sigma$ values and spatial distribution varies with rupture type and are affected by changes in fault geometry. Stress drop results indicate that frontal-thrust scenarios result in a lower $\overline{\Delta\sigma}$. This change can be attributed to the more uniform updip slip distribution for the shallow fault allowing the slip to breach the seafloor. As discussed in previous sections, distribution of $\Delta\sigma$ is noticeably affected by sudden changes in fault geometry as seen from where the splay and frontal thrust faults leave the buried décollement.

Chapter 4. Winona “Megathrust” Tsunami Source Models

4.1. End-member Winona Tectonic Models

For Winona there are two proposed tectonic models (Figure 4.1): (1) A coherent Winona block is underthrusting North America (Davis and Riddihough, 1982), and (2) the Winona Basin and underlying tilted block is part of a right lateral shear zone resulting from transpression (Rohr and Tryon, 2010). For assessing tsunami hazards, any plausible scenario that may give rise to tsunamigenic fault rupture should be modelled, even though some of these tsunami source scenarios may be considered low-probability scenarios in the eventual hazard assessment. It is beyond the scope of this thesis to resolve the ongoing scientific debate regarding regional tectonics, but it is necessary to highlight the main features of these models to provide proper context for our tsunami source modelling.

The two tectonic models are significantly different, and the difference cannot be reconciled by the currently limited data from this area. Gravity modelling can fit both models (Davis and Riddihough, 1982; Spence and Long, 1995; Rohr and Tryon, 2010). Seismic reflection images show evidence for a tilted block under Winona Basin, but it is unclear whether or not the block continues to greater depths under the continent. There are no reported receiver function results or ETS to indicate the presence of a deeper slab. Also, there has been a significant amount of compressional deformation in the Basin as evident by the presence of anticlines and folding in the seismic images (Rohr and Tryon, 2010). The planned 2020 seismic survey expedition will collect data across the Basin and improve our understanding of the tectonics in the Winona region. At present, neither model can be ruled out. In this work, I will explore potential thrust earthquake scenarios between the tilted Winona block and the accretionary prism (the first tectonic model outlined above). For convenience, I call this interface the “megathrust”.

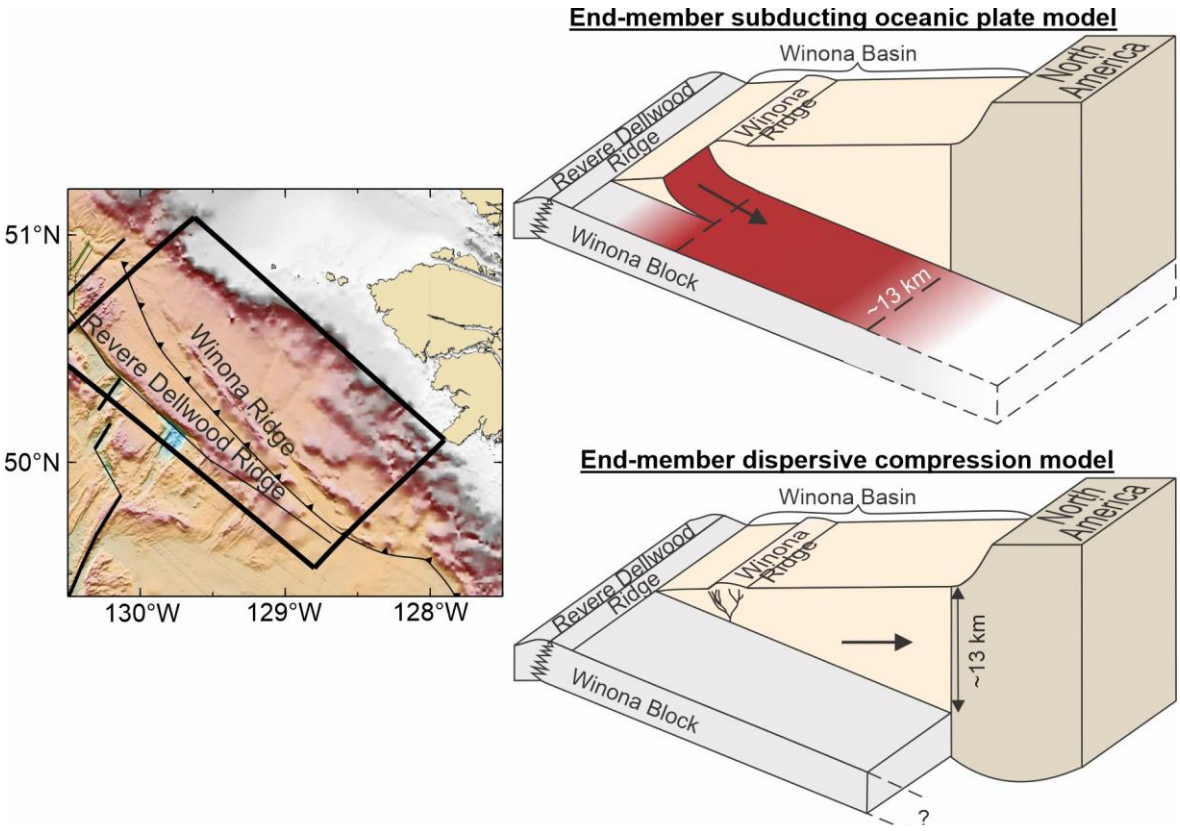

Figure 4.1. Two end-member tectonic models for Winona. Subduction model: There is the underthrusting of the Winona block. The Winona blocks spans from the northern bound of the Explorers plate subduction zone to just east of the Dellwood Knolls. Compressional model: Margin-normal convergence is accommodated by internal deformation of the Winona Basin. The faults beneath the Winona Ridge are based on Rohr and Tryon's (2010) interpretation of line 88-02 seismic reflection image (Figure 4.3).

4.2. Winona "Megathrust" Geometry

Previous researchers proposed the shallow geometry of the Winona block based on interpretation of seismic reflection images and its extrapolation to deeper depths. Just as for Cascadia, I assume the igneous crust basement to be the thrust fault interface. Building on the previous findings, I have constructed a more complete surface of the Winona block in this work. Details are explained as follows.

Various studies (e.g. Davis and Riddihough, 1982; Davis and Clowes, 1986; Rohr and Tryon, 2010; Riedel and Rohr, 2012; Ferguson et al., 2018) have interpreted igneous crust basement in Winona Basin seismic images. In this work, I compile a set of seismic images that

have the best basement resolution for Winona Basin. However, due to multiple layers of lava flow observed in seismic images near the Dellwood Knolls (Davis, 1982) the resolution of igneous crust basement is sometimes partially masked. All seismic reflection lines used in this study for determining the depth of igneous basement below the Winona Basin are given in Figure 4.2. Table 4.1 provides references for each profile, some of which already have the basement interpreted.

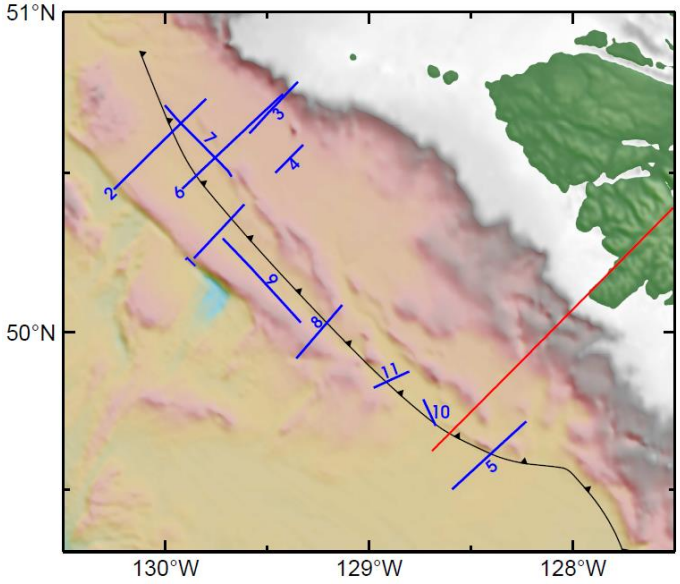

Figure 4.2. Locations of seismic reflection lines for Winona Basin used in this study. Grey lines: seismic reflection lines. Blue lines: profile images shown in Figure 4.3. Red line: line seperating Cascadia rupture scenarios from Winona rupture scenarios extending offshore of Brooks Peninsula.

Table 4.1. Summary of seismic reflection profiles used in this study.

Profile Number	Line ID	Figure	Image Reference (with Structural Interpretation)
1	77-06-1	4.3a	Davis and Seeman (1981); Davis and Riddihough (1982)
2	3[a]	4.3a	Davis and Clowes (1986)
3	4A[a]	4.3a	Davis and Riddihough (1982)
4	6A[a]	4.3a	Davis and Clowes (1986)
5	85-04	4.3b	Riedel and Rohr (2012)
6	88-02	4.3b	Rohr and Tryon (2010)
7	88-09	4.3b	Rohr and Tryon (2010)
8	94-36	4.3b	Ferguson et al. (2018)
9	94-39	4.3c	Rohr (2019, personal communication)
10	94-47	4.3c	Rohr (2019, personal communication)
11	94-48	4.3c	Rohr (2019, personal communication)

[a] Line IDs given are directly from Davis and Riddihough (1982) for these Chevron lines.

Davis and Riddihough (1981) and Davis and Clowes (1986) interpreted Chevron Canada Resource Ltd seismic reflection profiles 2, 3, and 4 to infer a landward dipping surface of the Winona block (Figure 4.4). Profile 1 in line with profile 4 shows the general tilted structure of the Winona block. Rohr and Tryon (2010) interpreted profiles 6 and 7 near the Dellwood Knolls to have a thick interbedded basalt and sedimentary package just above the igneous crust basement. For profiles 4, 5, 6, 7, and 8, I directly used the basement interpretations from their respective publications given in Table 4.1. The basement along profiles 3 and 4 is quite hard to determine due to the masking effect of the interbedded basalt and sedimentary layers. The deepest tilted reflector from profile 3 approximately matches the deepest depth of the interpreted basement of the immediately adjacent profile 6. Rohr and Tryon's (2010) interpretation of the top of the interbedded sediment and basalt layer for profile 6 is also corroborated by profile 3, as this depth (6.9 s above the deepest basement layer, Figure 4.3) is the depth at which the tilted horizons in profile 3 become much less resolved. This sudden change in resolution may be the result of the thick interbedded layer above the Winona block surface, similar to the interpreted interbedded layers in profiles 6 and 7. Courtesy of Kristin Rohr, I am able to use reflection images for profiles 9, 10, and 11 that are yet to be published (Figure 4.3c).

In this work, I calculate one to four igneous crust basement (assumed megathrust interface) depths along each profile. To calculate the approximate depth between the seafloor and the presumed megathrust from the seismic images, I use the two-way travel-time (TWT) to depth conversion curve from Davis and Clowes (1986) (Figure 4.5). The depth of the water column is calculated assuming the speed of sound in water is 1.5 km/s. For northwestern profiles near the Dellwood Knolls (2, 3, 6, and 7), the depths are adjusted for an interpreted zone of interbedded

basalt and sediment by assuming 50% basalt with a velocity of 5.5 km/s and 50% sediment with a velocity based on the Davis and Clowes (1986) velocity profile (Figure 4.3b).

When deriving the geometry shown in Figure 4.4, I assumed an approximately constant dip for the thrust fault. Unfortunately, seismic reflection images in this region do not penetrate deep

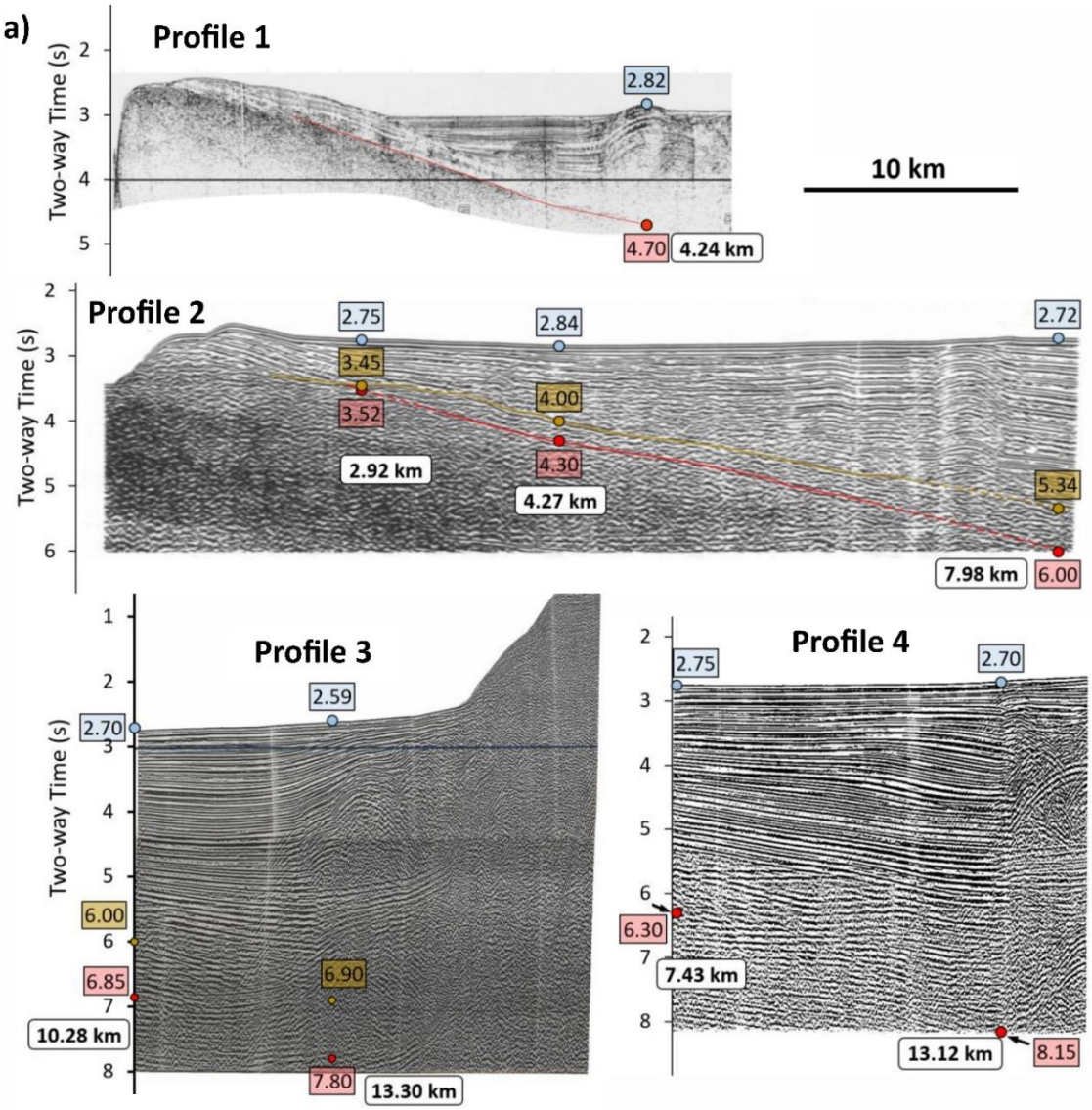

Figure 4.3. (a), (b), (c). Reflection profiles with interpreted Winona block surface depth values. Blue circles: TWT to seafloor. Brown circles: TWT to surface of interbedded basalt and sedimentary layer. Red circles: TWT to block surface. Profile 1 is from Davis and Seeman (1981). Profiles 2, 3, and 4 are from Chevron multibeam reflection lines studied in Davis and Riddihough (1982) and Davis and Clowes (1986). Profile 5 is from Riedel and Rohr (2012). Profiles 6 and 7 are from Rohr and Tryon (2010). Profile 8 is from Ferguson et al. (2018). Profiles 9, 10, and 11 are courtesy of Kristin Rohr (2019, personal communication).

enough through the sedimentary column to give a clear signal of the top of the block at deep depths. A major multichannel seismic survey project employing advanced survey technology is scheduled to take place in 2020, which might include either one or two lines for the Winona Basin.

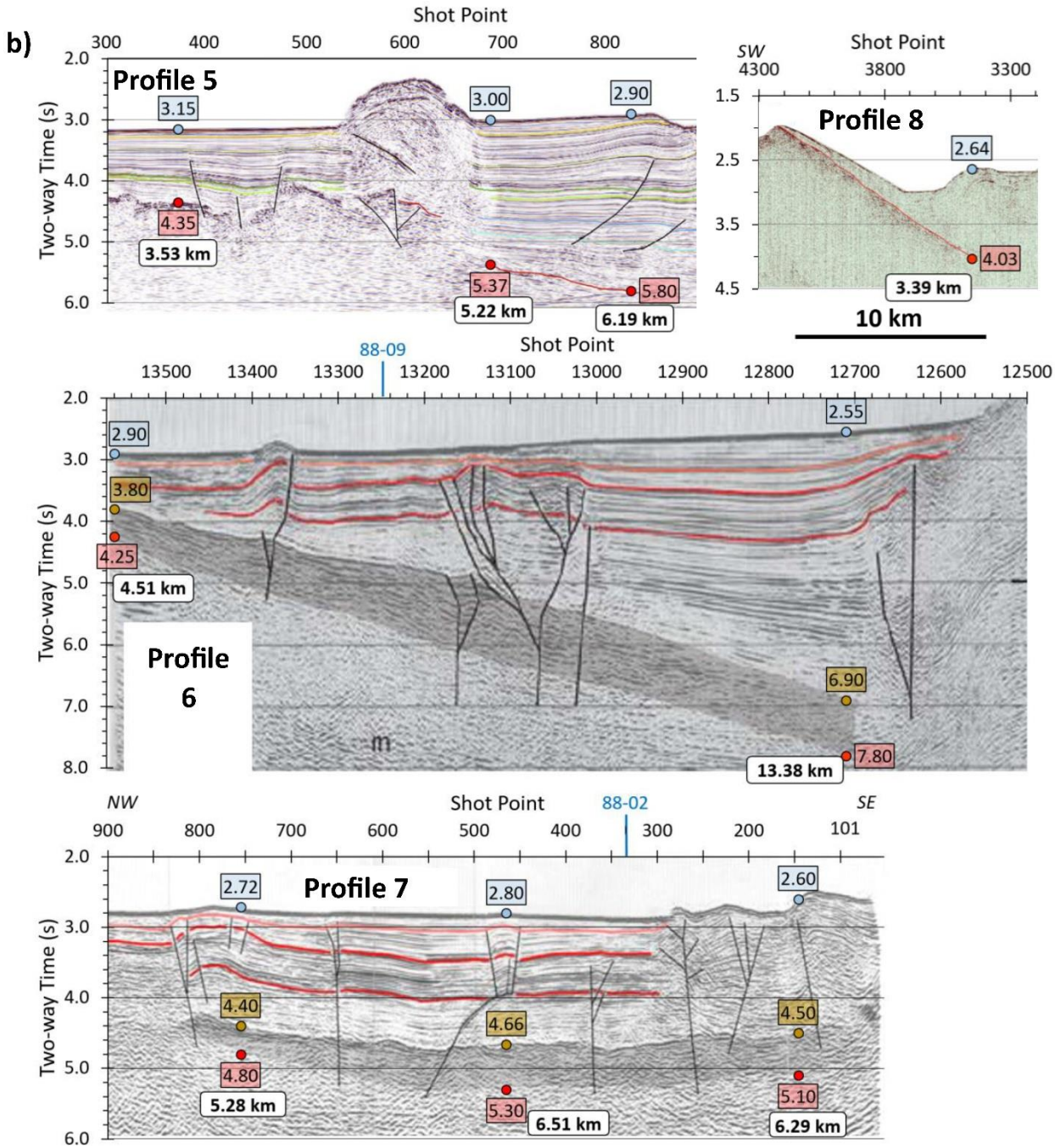

Figure 4.3. (Continued).

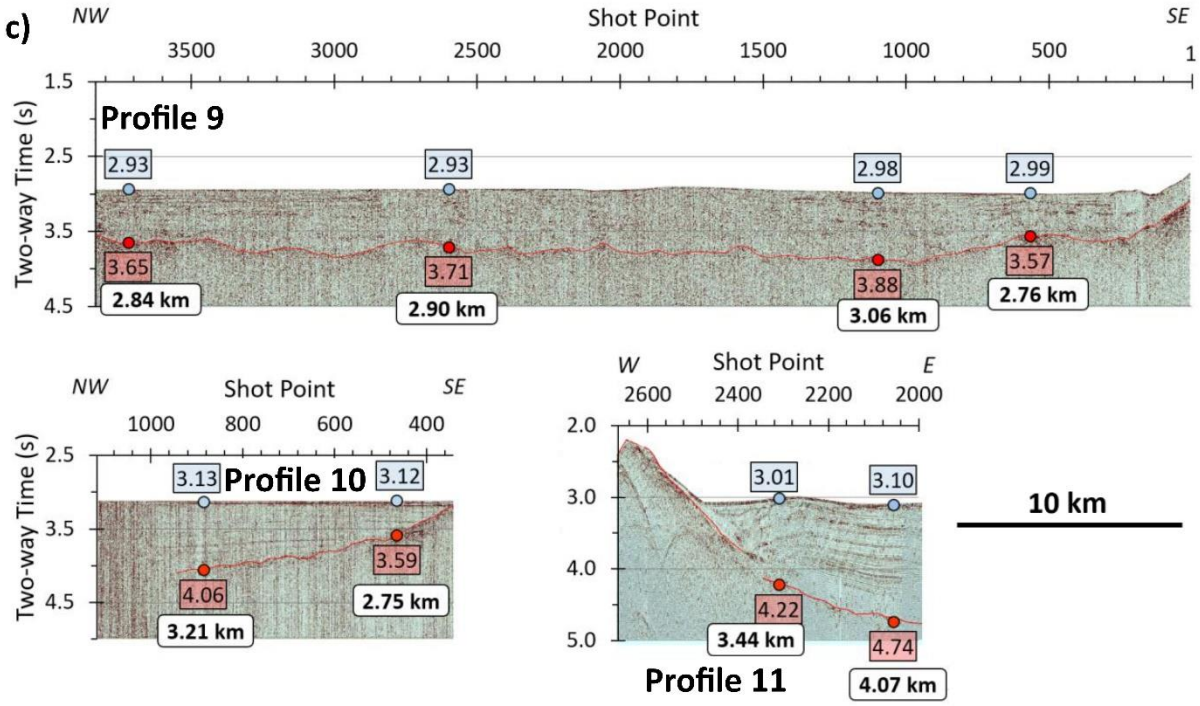

Figure 4.3. (Continued).

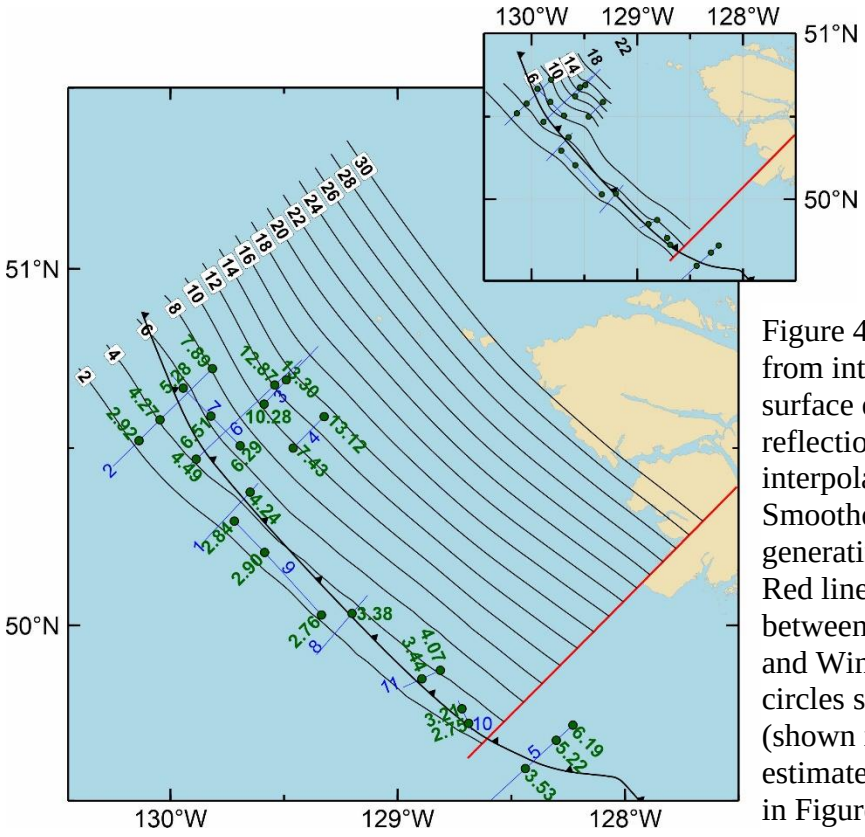

Figure 4.4. Winona block surface from interpolating depths of the surface estimated from seismic reflection images. Inset: Direct interpolation of surface. Main figure: Smoothed geometry used for generating tsunami source scenarios. Red line shows assigned boundary between Explorer plate subduction and Winona block subduction. Green circles show locations where depth (shown in km) of slab surface was estimated from seismic images found in Figure 4.3.

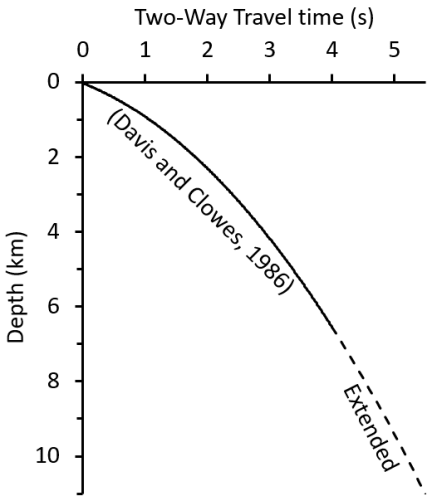

Figure 4.5. Relation between two-way travel-time (TWT) and depth for Winona Basin from Davis and Clowes (1986).

As explained in section 2.2, the dislocation model adopts an elastic half-space with a flat surface and therefore requires an adjustment of the megathrust geometry. After the adjustment, the décollement at the hypothesized Winona deformation front is still buried (Figure 4.6, red line). Also, as explained in section 2.2 (Figure 2.2), the trench-breaching geometry is created by

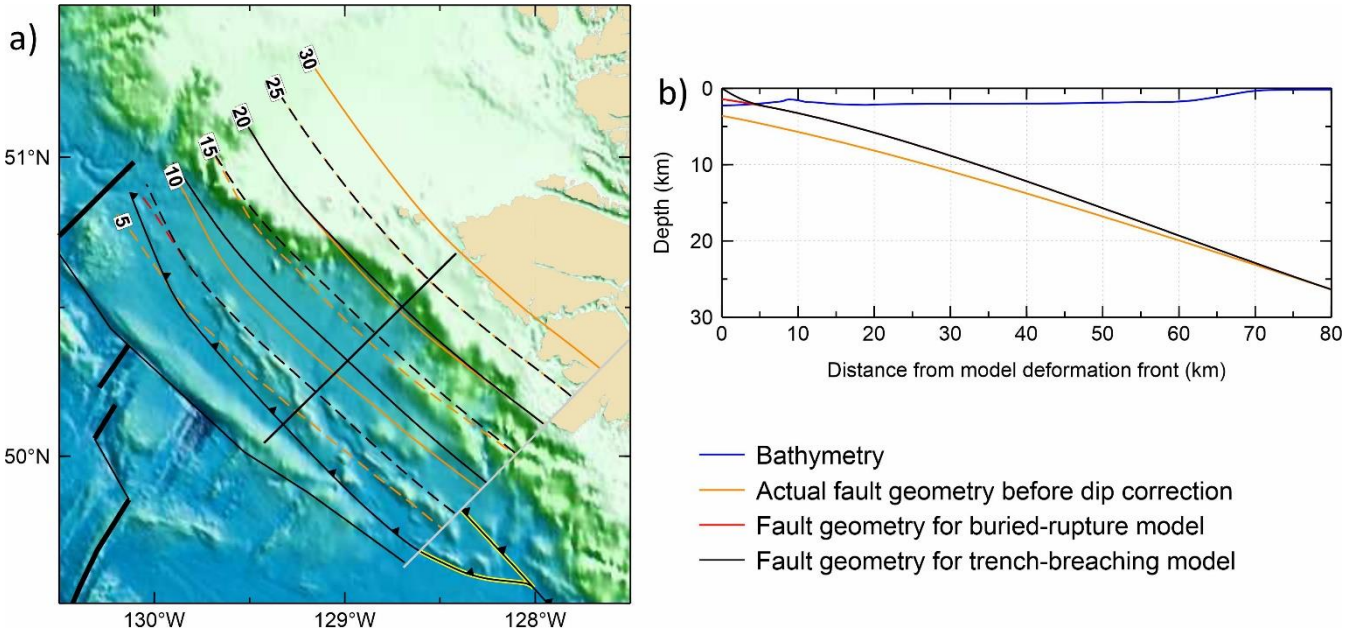

Figure 4.6. Winona megathrust geometry proposed in this work before the geometry adjustment described in section 2.2 (orange) and after the correction for both the buried (red) and the trench-breaching (black) rupture models. (a) The 5 km (dashed) and 10 km (solid) depth contours before and after the geometrical adjustment. (b) Profile shows how the megathrust geometry is adjusted. Profile location is shown on the map.

assuming a frontal thrust dipping at ~30° and smoothly soling into the buried décollement (Figure 4.6).

4.3. Winona Tsunami Source Scenarios

Types of tsunami sources considered for Winona include buried rupture and trench-breaching rupture (Figure 1.2). The six scenarios presented in this chapter (Table 4.2) are the first ever Winona block tsunami source scenarios. Two of them are buried rupture scenarios with different degrees of downdip rupture extent. The remaining four scenarios are for trench-breaching rupture where the downdip rupture extent and the magnitude of fault slip reaching the trench (as percentage of peak slip) are varied. Since there is a high degree of uncertainity on the tectonics of the Winona Basin region, as discussed in section 4.1, the presented Winona tsunami source scenarios may have to be given a lighter weight relative to the Cascadia and Haida Gwaii models when applied to hazard assessment.

When designing the Winona suite of scenarios, I must prescribe the strike and dip dimensions of the potential rupture zone and slip direction and amount. The downdip rupture limit for the Winona block thrust fault is not well constrained. Gao (2016) provides a rough idea of the shallow thermal condition (Figure 4.7), but the deeper thermal conditions are unknown due to a lack of both landward thermal data and knowledge of block interface geometry. To account for this knowledge gap, I create both narrow and wide rupture scenarios in which the rupture extends down to my interpolated 15 and 30 km depth contours, respectively. In the wide scenarios, the rupture terminates just east of the location of receiver function stations, which yielded no evidence for a subducted block. Along-strike rupture bounds are defined by the Dellwood Knolls area in the north and Brooks Peninsula in the south, abutting the modelled Explorer subduction.

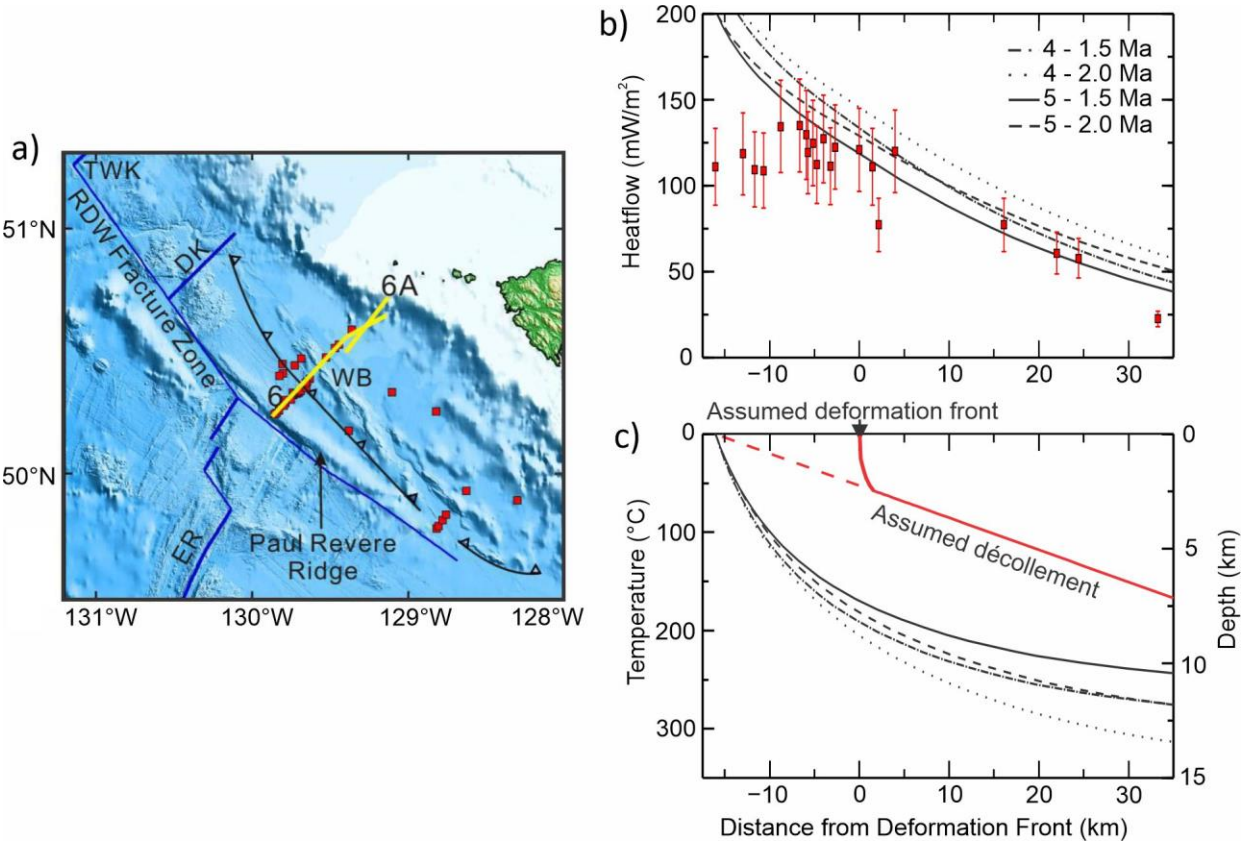

Figure 4.7. Winona block 1-D thermal model results from Gao (2016). (a) Winona region tectonic map. Heat flow measurements from Davis and Riddihough (1982) shown as red squares. Seismic reflection profiles 6 and 6A are shown with thick yellow lines. TWK, Tuzo Wilson Knolls; DK, Dellwood Knolls; WB, Winona Basin; ER, Explorer Ridge; RDW fracture zone, Revere-Dellwood-Wilson fracture zone. (b) Observed and modelled surface heat flows for a range of plate ages. (c) Model predicted temperatures of the assumed décollement. Figure from Gao (2016).

Table 4.2. Summary of Winona rupture scenarios for tsunami hazard assessment.

	Narrow	Wide
Buried Rupture	W-B-N (Figures 4.8a and 4.10a)	W-B-W (Figures 4.8b and 4.10a)
Trench-breaching Rupture 50%	W-T50-N (Figures 4.9a and 4.10b)	W-T50-W (Figures 4.9b and 4.10b)
Trench-breaching Rupture 100%	W-T100-N (Figures 4.9c and 4.10b)	W-T100-W (Figures 4.9d and 4.10b)

Even less is known about the slip deficit and potential slip direction. Given that Winona is next to the Explorer segment of the Cascadia subduction zone, I simply base the Winona slip

deficit and convergence on the Explorer parameterization (section 3.3). I assume a general margin-normal convergence rate of 20 mm/yr at direction 47° from north. For northern Winona, the assigned slip is tapered significantly, which reflects the possibility that closer to the Dellwood Knolls the magnitude of rupture diminishes. For the buried rupture scenarios, slip in the dip direction is assigned with the same bell-shaped function as described in section 2.4. For the trench-breaching scenarios, I construct models for the slip to decrease to 50% (W-T50-N and W-T50-W) or 100% (W-T100-N and W-T100-W) of the peak slip when breaching the seafloor, in exactly the same fashion as described in section 3.3.3. Instead of digging into the basically intractable problem of recurrence interval here, I simply use 500 years of slip deficit to assign the coseismic slip like for Cascadia, meaning the peak value of the bell-shaped slip distribution is 10 m. Since the calculated uplift is proportional to assigned fault slip, users of these results can easily scale them in accordance with their own understanding or assumption about how large the peak slip should be.

The uplift predicted by the buried rupture scenarios (Figure 4.8) shows a familiar pattern of uplift near the "trench" and subsidence farther landward. The margin-normal wavelength of the deformation variation shortens with the rupture width (Figure 4.10) as seen for Cascadia scenarios in section 3.3. The same coastal subsidence is observed for trench-breaching and buried rupture scenarios with the wide rupture width. The trench-breaching scenario, of course, produces a greater amount of near-trench uplift. However, just east of the area of the greater near-trench uplift, the uplift is actually less compared to the buried rupture scenarios (i.e. ~8-28 km and ~10-45 km from deformation front for narrow and wide ruptures, respectively), a phenomenon seen also in the Cascadia trench-breaching scenarios (Figure 3.12). With greater decrease in slip magnitude from the peak slip to the trench, the uplift increases in this location

due to greater shortening of the upper plate material.

Similar to the Cascadia models, stress drop ($\Delta\sigma$) for the Winona models shows a sensitivity to rupture type and fault geometry. The $\Delta\sigma$ is more dispersed and smaller for wide rupture (W-B-W, W-T50-W, and W-T100-W) due to the lower margin-normal slip gradient change and the greater rupture widths. The relatively sudden decrease in slip near the northwestern and southeastern slip patch termini results in high $\Delta\sigma$ peaks (Figures 4.8 and 4.9), but they are artefacts associated with how the slip is tapered in the strike direction and should not be taken seriously. Shallow fault geometry near the deformation front plays a significant role in the calculated $\Delta\sigma$ as discussed for the Cascadia seafloor breaching models (sections 3.3.2 and 3.3.3). The $\overline{\Delta\sigma}$ within the rupture area encompassed by the 1 m slip contour (10% of peak slip) is lower for the trench-breaching than for the buried-rupture scenarios. As discussed previously (section 3.4), the lower $\overline{\Delta\sigma}$ can be attributed to the more uniform updip slip distribution for the shallow fault where either 50% or 100% of peak slip breaches the seafloor. The overall $\Delta\sigma$ distribution and $\overline{\Delta\sigma}$ results for the Winona tsunami source scenarios are comparable in scale to the other observed megathrust earthquakes shown in the appendix.

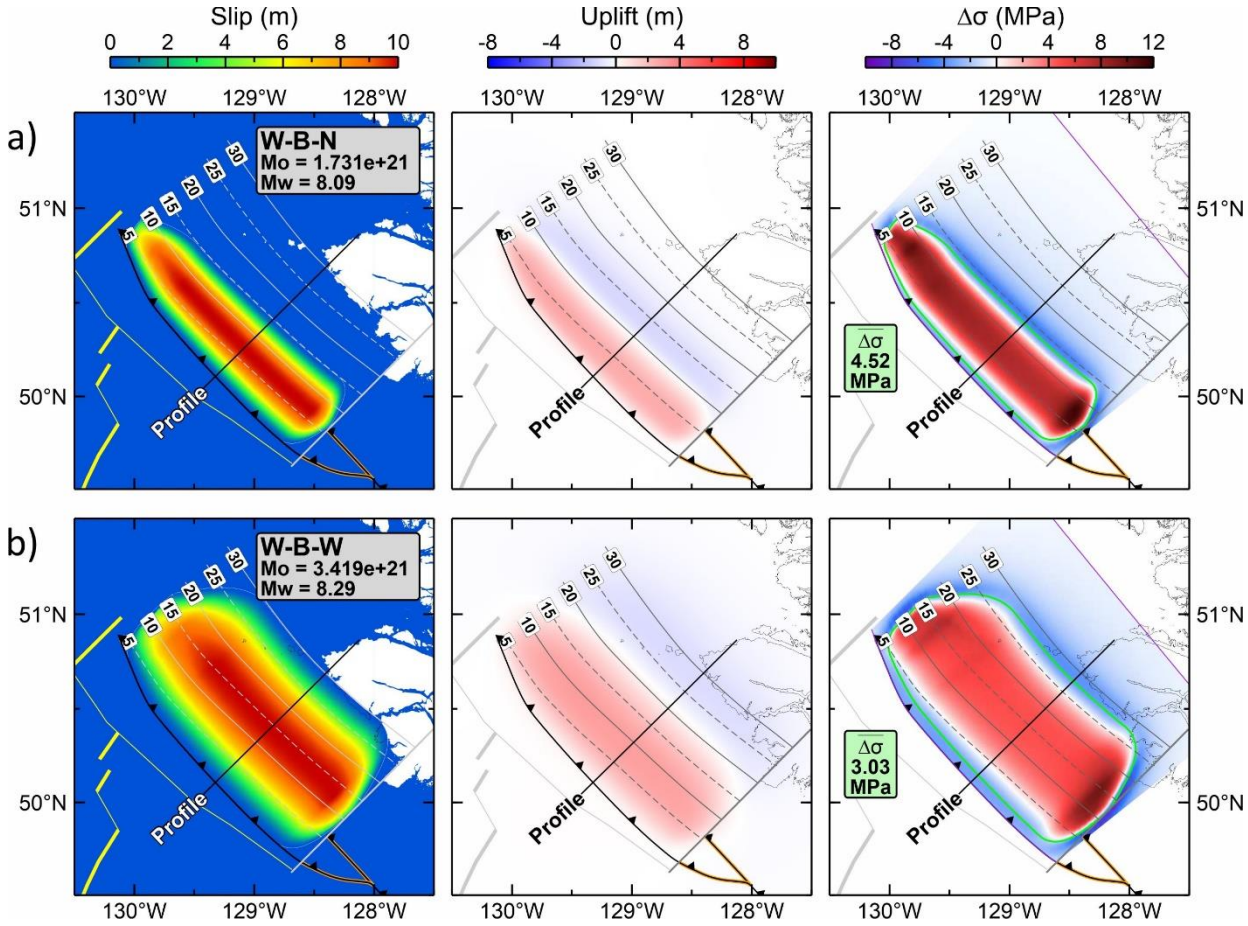

Figure 4.8. Buried-rupture models for the potential Winona thrust fault. From left to right in each row: slip, uplift, and stress drop. (a) Narrow rupture. Slip bounded by 15-km depth contour. (b) Wide rupture. Slip bounded by 30-km depth contour. Green line in the right panel is the contour of 10% peak slip within which $\overline{\Delta\sigma}$ is calculated.

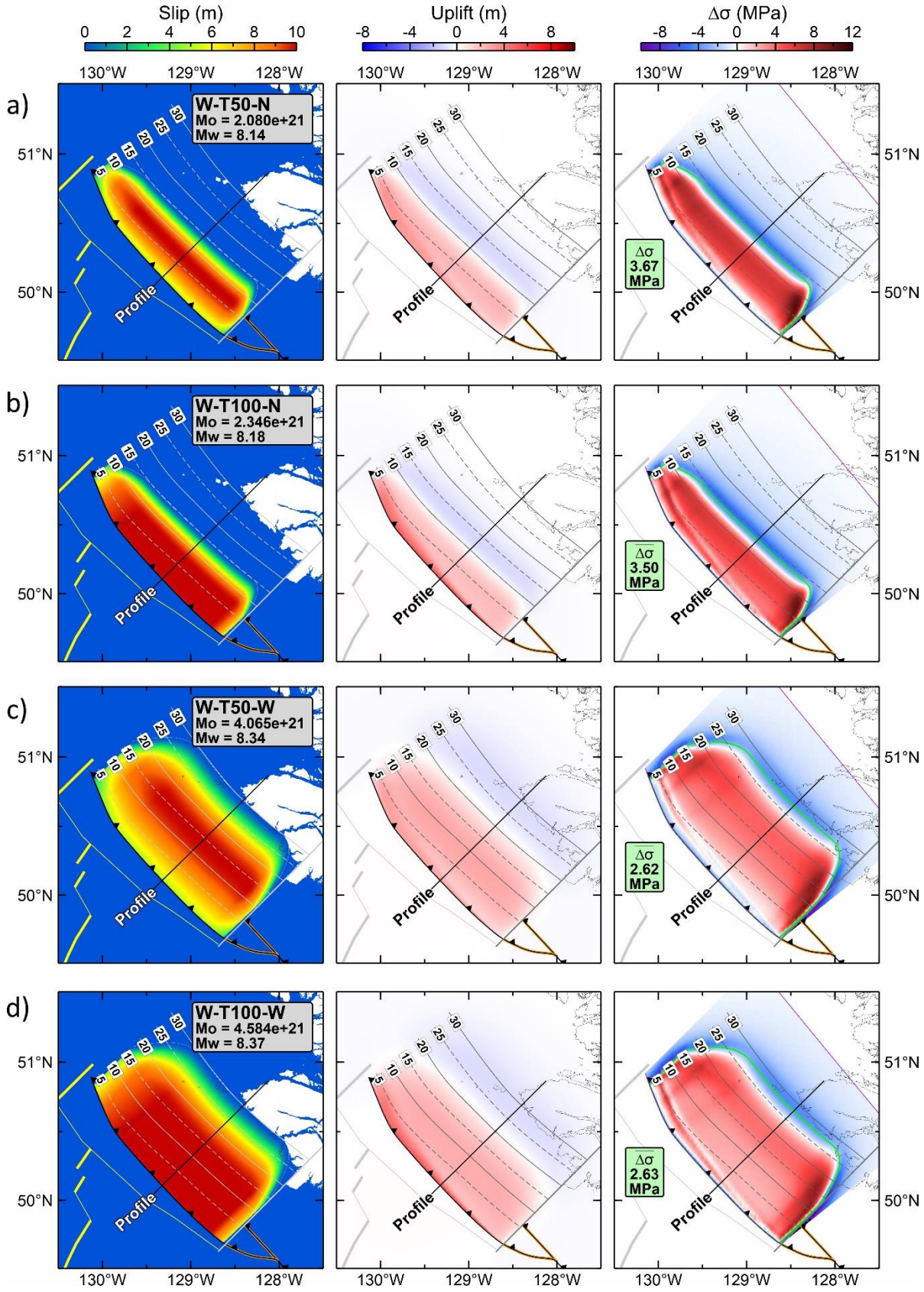

Figure 4.9. Trench-breaching rupture models for the potential Winona thrust fault. From left to right in each row: slip, uplift, and stress drop. (a) Narrow rupture. Slip bounded by 15-km depth contour. (b) Wide rupture. Slip bounded by 30-km depth contour. Green line in the right panel is the contour of 10% peak slip within which $\overline{\Delta\sigma}$ is calculated.

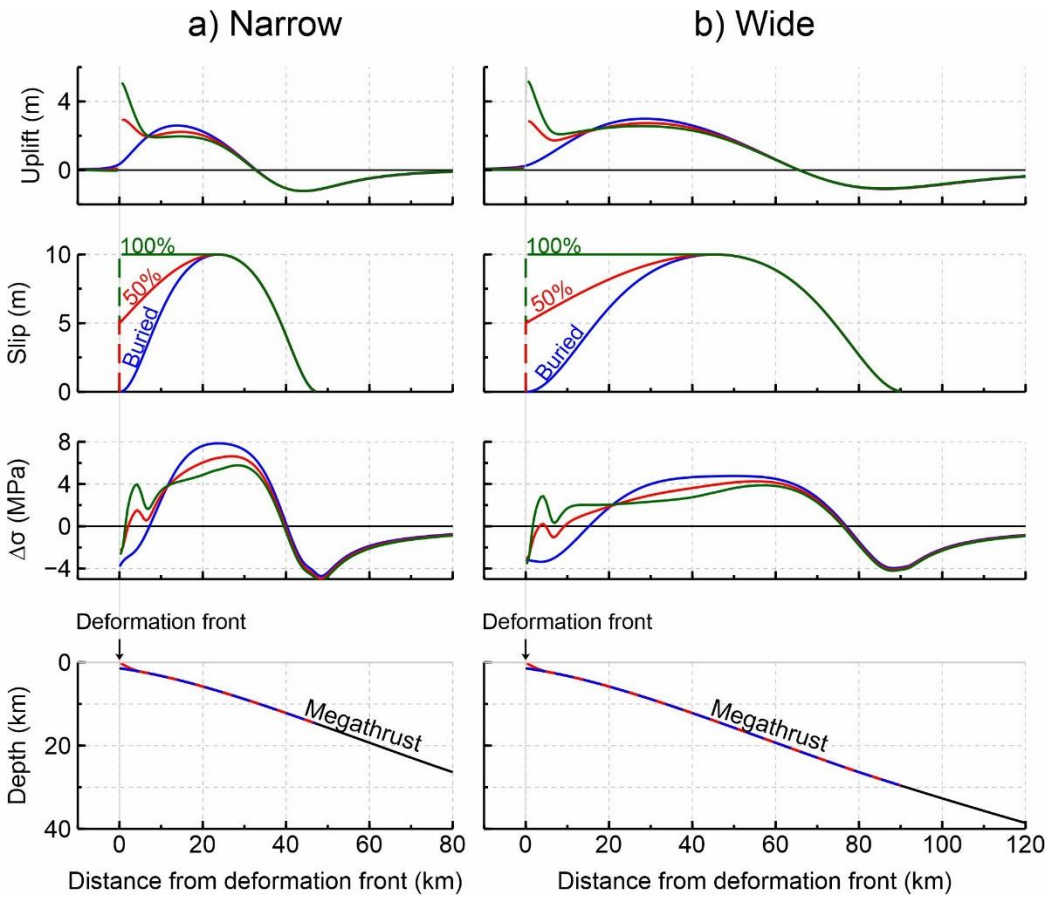

Figure 4.10. Fault slip, surface deformation, and stress drop for narrow (a) and wide (b) buried rupture and trench-breaching rupture models along the profile shown in Figures 4.8 and 4.9. Seafloor uplift, slip, stress drop on the fault, and fault geometry shown for each profile from top panels to bottom panels, respectively. Blue lines: Buried rupture models W-B-N and W-B-W. Trench-breaching models where 50% (W-T50-N and W-T50-W) and 100% (W-T100-N and W-T100-W) of the peak slip reaches the deformation front are shown with red and green lines, respectively. Red line in bottom panels shows the rupture zone for both trench-breaching scenarios, while the rupture zone for the buried rupture is a dashed green line here.

Chapter 5. Haida Gwaii Megathrust Tsunami Source Models

5.1. Competing Models of Regional Tectonics

Haida Gwaii is situated along the transpressional PA-NA plate boundary (Figure 5.1). There is no argument that the QCF accommodates the margin-parallel component of the relative motion between the plates, but models differ with regard to how the smaller margin-normal component is accommodated. The two main end-member tectonic models for accommodating the margin-normal component share some similarities with the two competing tectonic models for the Winona Basin outlined in section 4.1: (1) Oceanic plate underthrusting North America

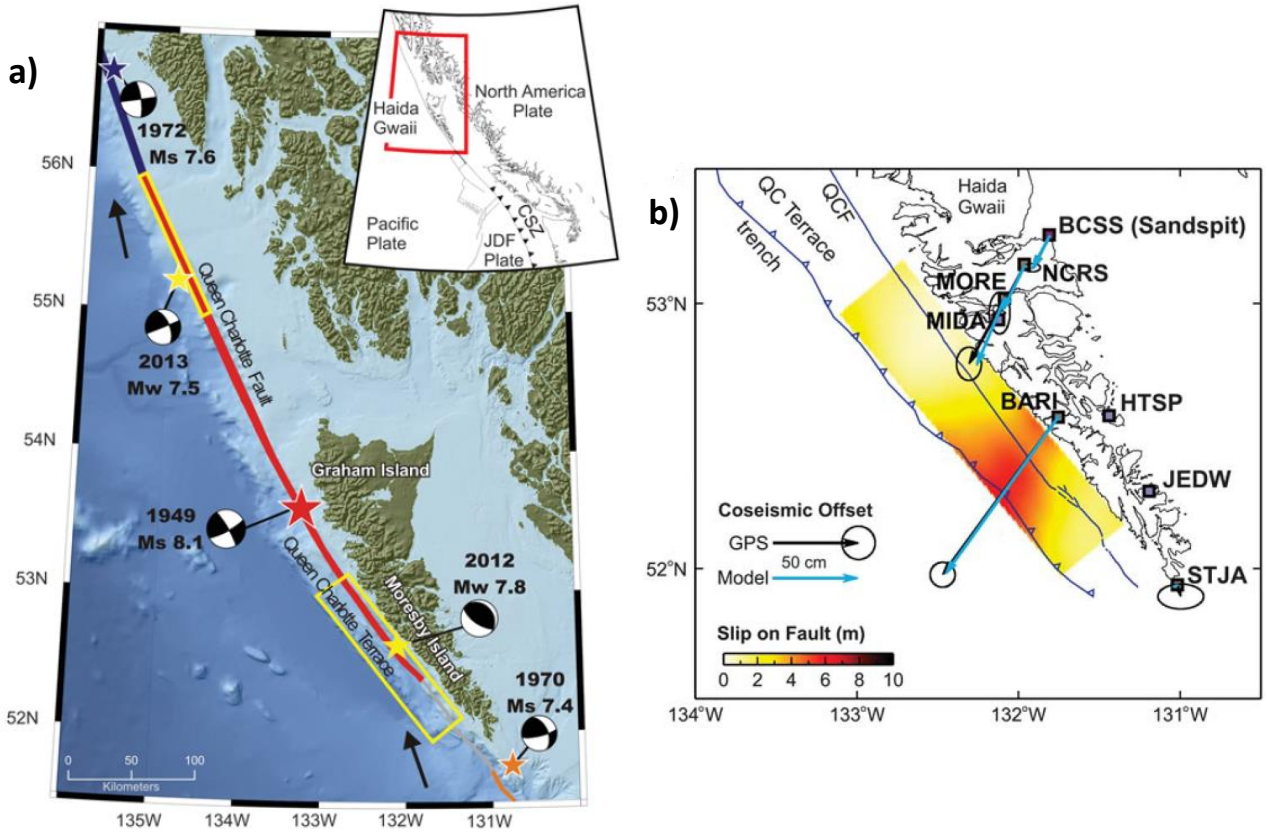

Figure 5.1. Tectonic setting and earthquake activity for the Queen Charlotte margin. (a) Locations of large earthquakes within the last 70 years (from James et al., 2015). Aftershock zones for the 1949 Queen Charlotte Islands, 1970 Cape St. James, and 1972 Sitka earthquakes are coloured red, orange, and blue, respectively. (b) Modelled rupture with GPS measured vectors for the *Mw* 7.8 2012 Haida Gwaii earthquake (from Nykolaishen et al., 2015).

(Hyndman and Ellis, 1981), and (2) transpression resulting in permanent shortening in the colliding plates around the plate boundary (Rohr et al., 2000; Rohr, 2015) (Figure 5.2).

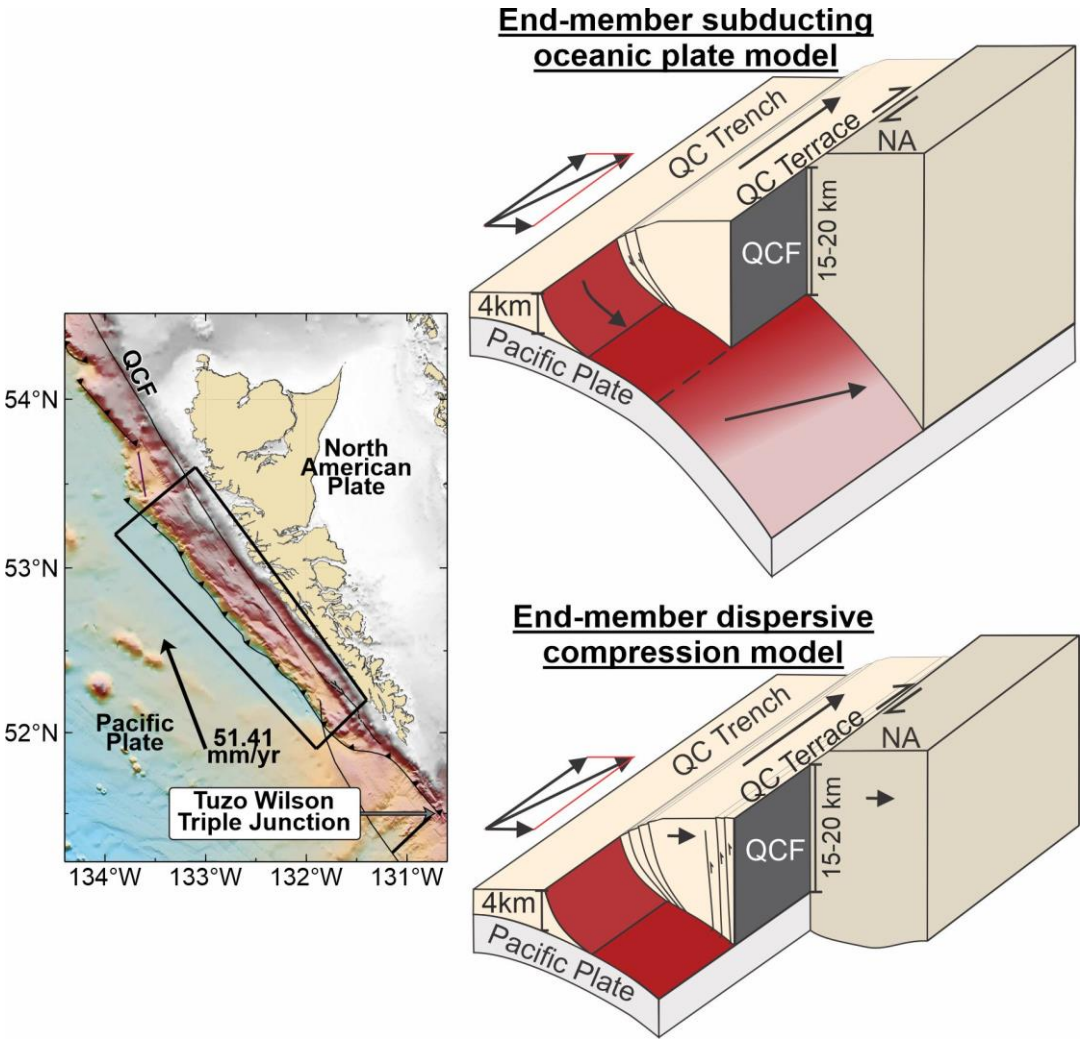

Figure 5.2. Two end-member tectonic models for Haida Gwaii. Subduction model: There is the underthrusting of the Pacific plate from the Tuzo Wilson triple junction to ~53.5°N where the deformation front and related thrust system start to become segmented. Compressional model: Margin-normal convergence with internal deformation of the plates and terrace.

Evidence supporting the underthrusting model includes receiver function analysis indicating the presence of a dipping low-velocity slab under Haida Gwaii (Smith et al., 2003; Bustin et al., 2007; Gosselin et al., 2015), and most compellingly, the occurrence of the *Mw* 7.8 2012 Haida Gwaii thrust earthquake that generated a large tsunami (Leonard and Bednarski,

2014) (Figure 5.1). Evidence supporting the model of internal deformation accommodating convergence includes an extensive amount of compressive structures on the continental shelf (Rohr, 2015), although it is less clear how much of the compressional deformation is on-going or took place in the recent past. A densely faulted submarine terrace is a characteristic feature of transpression and its presence is expected in both models. It is unknown how much convergence has been accommodated by the internal deformation of this terrace. For the underthrusting model the Queen Charlotte trough is proposed to be a partially filled trench, while for the internal deformation model it is proposed to be a flexural trough. It is most likely that the tectonic setting cannot simply be described solely as one of these scenarios but is a combination of the two models and has been changing through geological time as relative plate motions have shifted.

Steady change in the relative motion between the PA and NA plates is believed to have had a considerable effect on the tectonic evolution of the Haida Gwaii region. Reconstruction of relative plate motion indicates that the QCF was purely a strike-slip boundary up until 12.47 Ma when a convergence component began to develop (DeMets and Merkouriev, 2016). Along the plate boundary west of Haida Gwaii, the motion obliquity then steadily evolved from margin-parallel to the current value of 21° ± 1.2° (DeMets and Merkouriev, 2016), with the convergence rate being 13-20 mm/yr (Mazzotti et al., 2003; DeMets and Merkouriev, 2016; Atwater & Stock, 1998). On the basis of limited campaign GPS data with relatively large errors, Mazzotti et al. (2003) proposed that 5 ± 2 mm/yr of the convergence is accommodated through internal shortening of the NA plate and the rest by plate subduction. The present-day angular velocity of the NA plate relative to the PA plate has been found to be 0.760° Myr^{-1} by an Euler pole at 49.95°N 283.74°E (DeMets and Merkouriev, 2016). By applying the plate motion model of DeMets and Merkouriev (2016), ten Brinks et al. (2018) inferred how deep the PA slab might

extend today. They proposed that a motion obliquity of >14°-15° from margin-parallel and a shallowly dipping subducted slab that extends to depths below the east coast of most of Haida Gwaii could lead to the rise of the archipelago. Due to the along-strike curvature of the Queen Charlotte margin, the obliquity increases from North to South (Figure 5.1a).

In the preliminary tsunami hazard assessment by Leonard et al. (2012; 2014), it was proposed that a *Mw* 7.8-8.2 earthquake on the Queen Charlotte megathrust could result in a runup exceeding 3 m along the west coast of Haida Gwaii. The estimate was made by assuming a rectangular fault with uniform slip in the seimogenic zone (150-350°C) and linearly decreasing the slip to zero in a transition zone (350-450°C). The 2-D thermal model used in the assessment was from Smith et al. (2003), although more recent thermal modelling by Wang et al. (2015) after the Haida Gwaii earthquake shows revised depths for these temperatures. Leonard et al. (2012; 2014) used these parameters and empirical relationships to calculate moment magnitude, reoccurrence intervals, and the resulting maximum wave runup. The estimated runup from this preliminary study was later supported by field observations following the 2012 Haida Gwaii earthquake (Leonard and Bednarski, 2014). It was found that the runup caused by this earthquake exceeded 3 m at sites covering ~200 km of the coastline, with a maximum of 7-13 m at some sites. These studies give us a good idea of what to expect for our tsunami source models for Haida Gwaii.

5.2. Haida Gwaii Megathrust Geometry

Uncertainties in the geometry and, to some extent, the presence of the subducted slab at Haida Gwaii are large due to the scarcity of data. The most direct information that can constrain the slab depth includes low-velocity zones inferred from receiver functions. Here I use some of the receiver function results by Bustin et al. (2007) and Gosselin et al. (2015) to determine the

slab geometry (Figure 5.3). Only one receiver function station (HG4B) does not follow the interpolated slab geometry and this station recorded the fewest earthquakes to constrain the receiver function depth calculation, so it is weighted to be negligible in the geometry interpolation. For plate interface depth near the trench, I use depth interpretations from data along seismic reflection profiles below Ocean Bottom Seismometer stations deployed in December 2012 (Riedel et al., 2014a; Riedel et al., 2014b) offshore southern

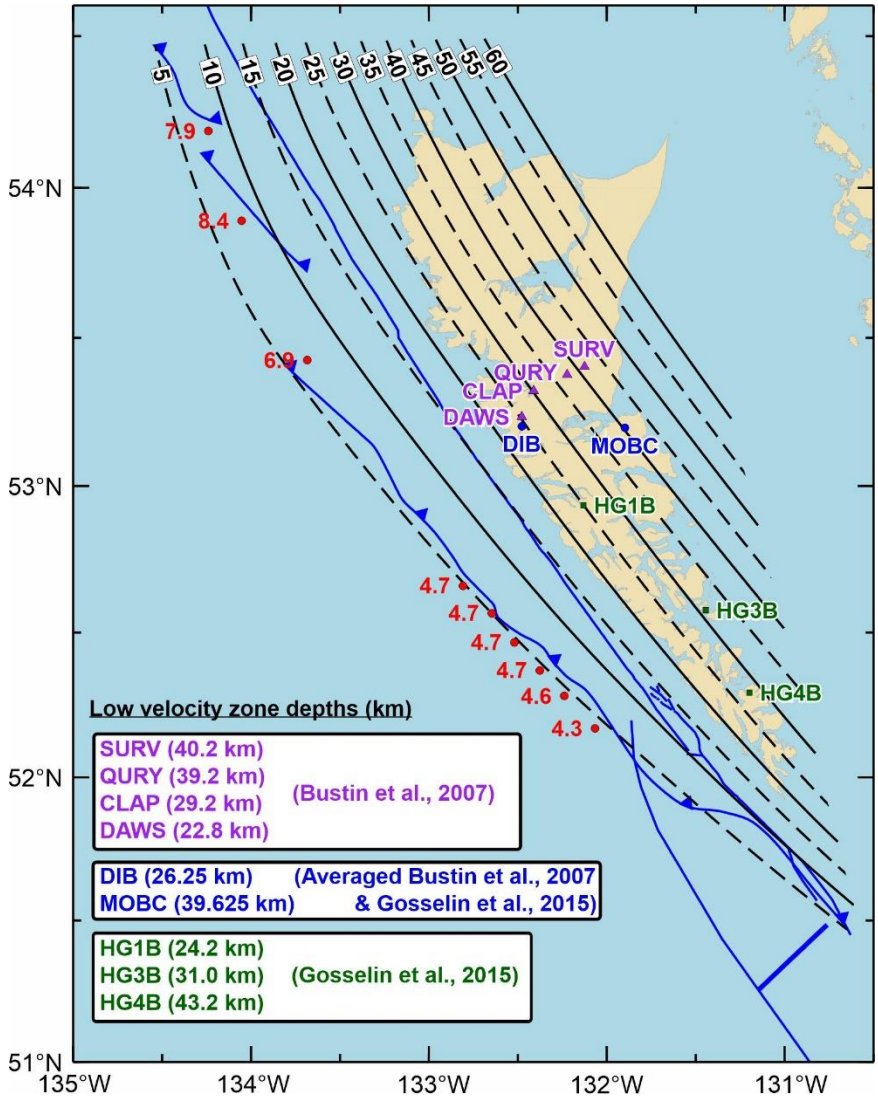

Figure 5.3. Haida Gwaii megathrust geometry by interpolating depths of the surface from seismic reflection interpretations near the trench (red circles) and deeper receiver function low-velocity zone depths (Bustin et al., 2007; Gosselin et al., 2015).

Haida Gwaii and depth interpretations from three USGS L-5-77-EG lines (L-5-77-1, L-5-77-2, and L-5-77-3). Six depths derived from seismic reflection profiles offshore southern Haida Gwaii assumed a water velocity of 1.5 km/s and an average sediment velocity of 2 km/s, which is appropriate for these sedimentary thicknesses where TWT between seafloor to igneous crust ranges from 1.3 to 1.8 s. The same was done for one depth calculation at the furthest east location where basement is visible along each of the three L-5-77-EG lines used offshore northern Haida Gwaii. However, due to the thicker sediment for these three depth interpretations (TWT ranging from 3.1 to 3.7 s) an average sediment velocity of 3 km/s was used. When

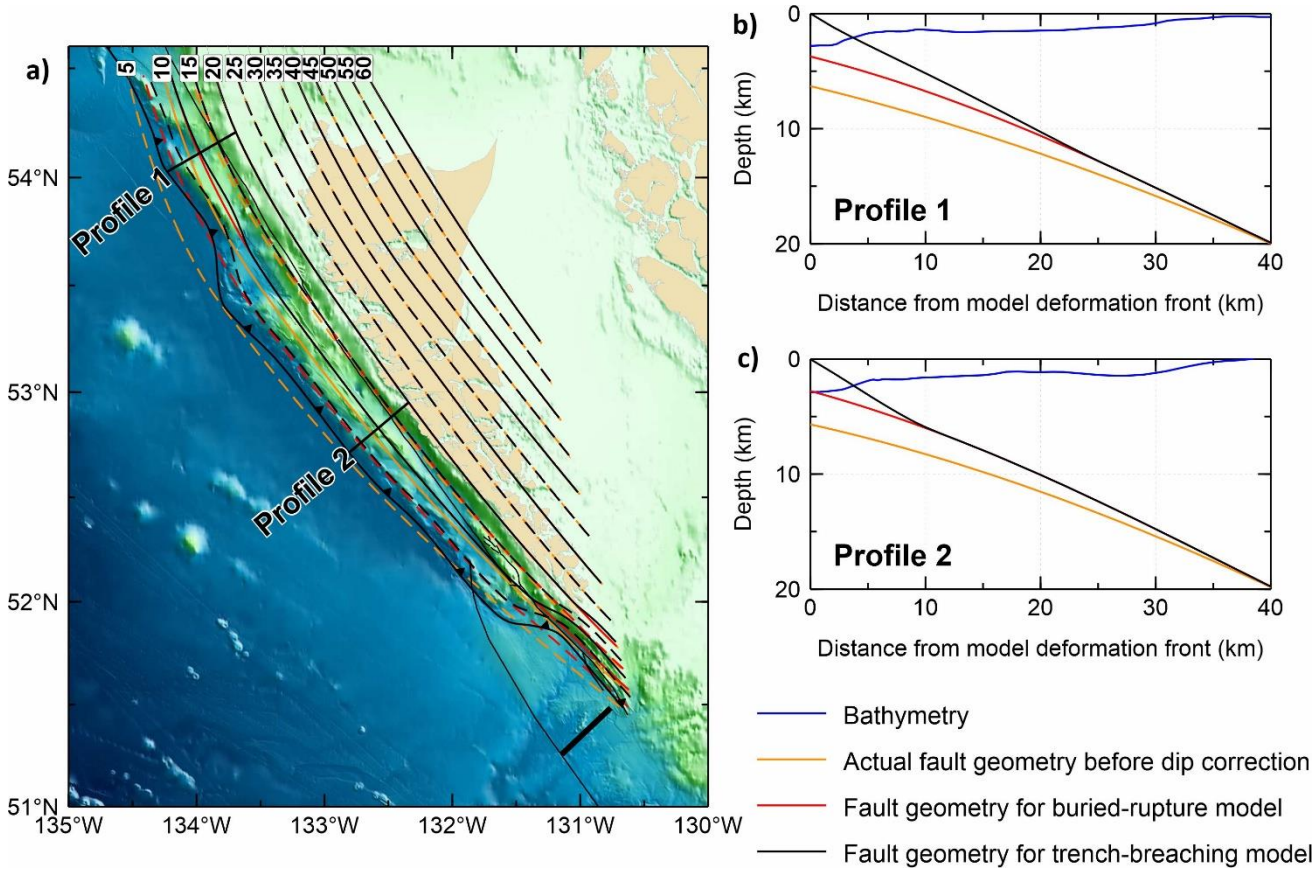

Figure 5.4. Haida Gwaii megathrust geometry proposed in this work before the geometry adjustment described in section 2.2 (orange) and after the correction for both the buried (red) and the trench-breaching (black) rupture models. (a) The 5 km (dashed) and 10 km (solid) depth contours before and after the geometrical adjustment. (b) Profiles show how the megathrust geometry is adjusted. Profile locations are shown on the map. Trench trace shown is a simplified smoothed version of the segmented trace seen in previous figures and is used in the modelling process.

constructing a 2-D megathrust geometry for their Haida Gwaii thermal model, Wang et al. (2015) had used similar data, although only along a single profile crossing the 2012 rupture zone.

As explained in section 2.2, the dislocation model adopts an elastic half-space with the surface being flat and therefore requires an adjustment of the megathrust geometry. The adjustment makes the fault depth at the trench shallower by the depth of the water column (Figure 5.4, red line). As explain in section 2.2 (Figure 2.2), the trench-breaching geometry is created by assuming a frontal thrust that dips at ~30° dip and smoothly soles into the megathrust (Figure 5.4, black line).

5.3. Haida Gwaii Tsunami Source Scenarios

The *Mw* 7.8 2012 Haida Gwaii thrust earthquake not only supports the subduction model but also raises awareness that adequate conditions may exist for the same fault to generate thrust earthquakes and tsunamis north and south of the 2012 rupture zone. Exploring potential rupture of adjacent regions is of great importance for tsunami hazard assessment of Haida Gwaii and nearby regions. In this work, I create nine rupture scenarios, which include both buried and frontal-thrust Haida Gwaii rupture scenarios (Table 5.1).

The downdip rupture limit used for the Haida Gwaii scenarios is constrained mainly by where the QCF may intersect the megathrust. This intersection is a major structural boundary that most likely plays an important role in controlling the megathrust rupture zone. For the *Mw* 7.8 2012 earthquake, Wang et al. (2015) show that the thermal boundary of 450°C along the subduction interface is at depths of 25-30 km. This thermal boundary is most likely deeper than what may be inferred by assuming a vertical QCF, but it is highly possible QCF dips east at large depths and hence intersecting the megathrust at a location east of its surface trace (Wang et al., 2015). Therefore, in this work the downdip rupture boundary used is a trace ~10 km east of the

QCF. However, to allow rupture to extend as far south as the Tuzo Wilson triple junction as done in the preliminary tsunami hazard assessment of the area (Leonard et al. 2012; 2014) I shift the downdip rupture trace slightly further landward for the southernmost rupture where the deformation front merges with the QCF.

Along-strike rupture boundaries are defined by zones of structural complexity and the thermal regime. In accordance with the interpretations of bathymetric and seismic reflection data

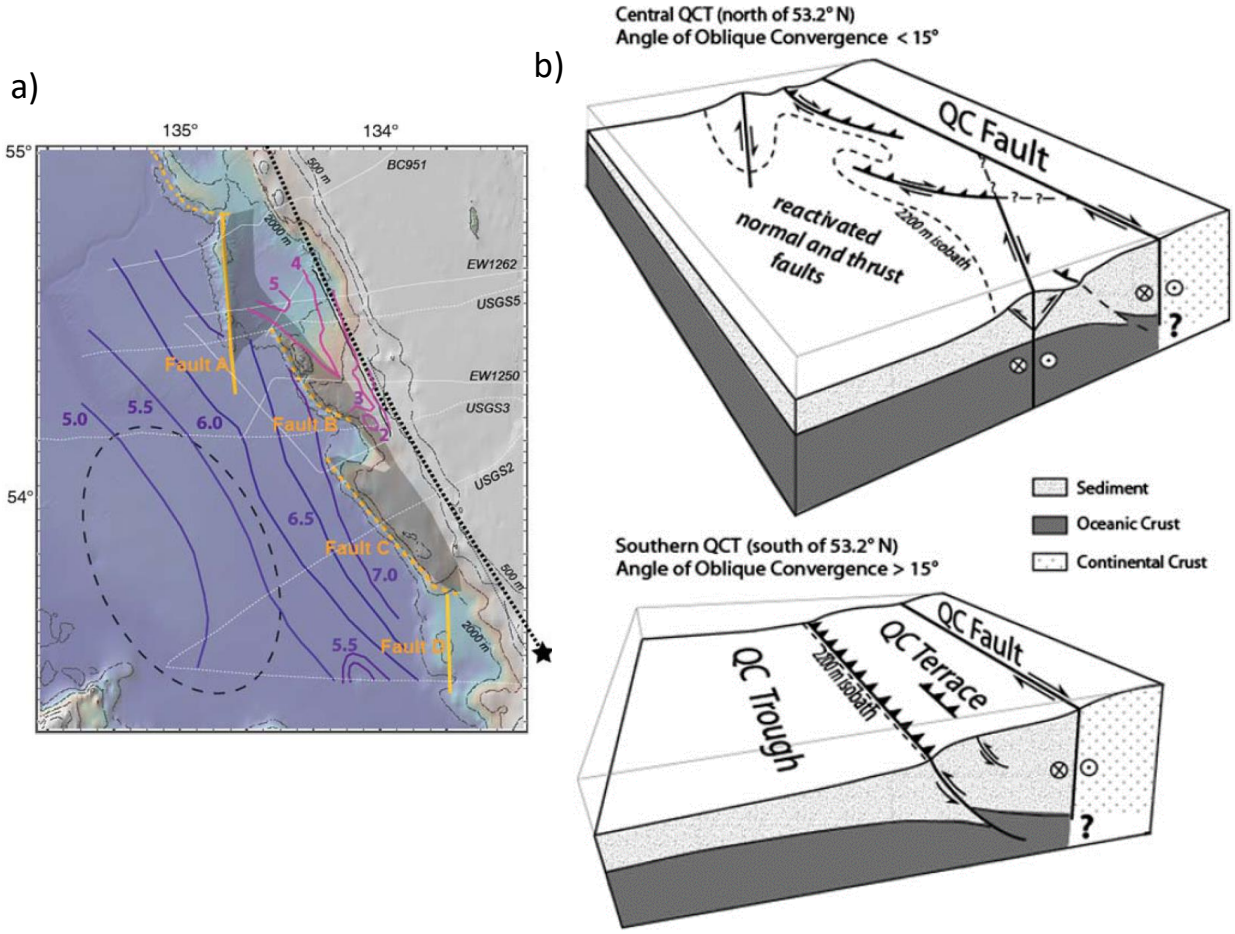

Figure 5.5. Structural summary of northern Haida Gwaii terrace by Tréhu et al. (2015). (a) Map view north of 53.2ºN. Faults B and C are interpreted relict thrust faults (dashed orange lines) associated with reactivated strike-slip fault zones. They appear to be segmented and offset from the main deformation front to the south and the northernmost relict thrust fault shown on the map (unlabeled) by wrench fault zones A and D (solid orange lines). (b) Diagram indicating the difference between deformation regimes north and south of 53.2°N where obliquity from margin parallel decreases from >15° to <15°.

by Tréhu et al. (2015), our assumed rupture may extend at least as far north as 53.2°N, beyond which a complex terrace structure is observed (Figure 5.5). If the rupture extends beyond this latitude, it most likely has a very complicated rupture sequence due to the structural complexity of the area. In this work, I allow the rupture to extend as far north as 54.5°N along relict thrust faults interpreted by Tréhu et al. (2015). I set the southern rupture boundary to be just north of the Tuzo Wilson triple junction (Figure 5.2) due to the anticipated hot thermal conditions that would impede seismic rupture.

Because the strike-slip component of the PA-NA motion along the margin is accommodated by the Queen Charlotte transform fault, only a small convergence component is responsible for tsunamigenic thrust faulting along the megathrust. As previously mentioned in section 5.1 studies indicate the convergence component of PA-NA plate motion west of Haida Gwaii is within the range of 13-20 mm/yr. In this work, I use the high-end number of 20 mm/yr (Atwater and Stock, 1998). Like for the other two regions discussed in preceding chapters, I define the peak slip using time-elapsed slip deficit rate. For Haida Gwaii, the average recurrence between large megathrust earthquakes is poorly known, so I simply used a slip deficit of 500 years. Again, these model results can be scaled linearly if other assumed slip deficit accumulation and/or convergence rate values are preferred.

A symmetric bell-shaped function (equations 2.1 and 2.2) from section 2.4 is used to assign buried rupture slip in the dip direction. With the convergence rate of 20 mm/yr and 500-year slip deficit as explained above, the peak slip of the bell-shaped function is 10 m. The slip is then tapered to zero at both termini of the rupture zone over a small distance range (5% of the strike length) using the method described in section 2.4. To account for the relatively abrupt change in obliquity at ~53.4°N and the consequent decrease in the convergent component of the plate

motion, the slip is decreased by ~8% north of that location.

Table 5.1. Summary of Haida Gwaii rupture scenarios for tsunami hazard assessment.

	Full	North	South
Buried Rupture	H-B-F (Figures 5.6a and 5.9)	H-B-N (Figure 5.6b)	H-B-S (Figure 5.6c)
Trench-breaching Rupture 50%	H-T50-F (Figures 5.7a and 5.9)	H-T50-N (Figure 5.7b)	H-T50-S (Figure 5.7c)
Trench-breaching Rupture 100%	H-T100-F (Figures 5.8a and 5.9)	H-T100-N (Figure 5.8b)	H-T100-S (Figure 5.8c)

A smooth distribution of coastal subsidence and seafloor uplift is observed for all the rupture scenarios except very near the trench (Figure 5.6). As seen for Cascadia and Winona scenarios, the wavelength of the margin-normal deformation scales with rupture width (Figure 5.9). Coastal subsidence appears to be unchanged between all models, but for the trench-breaching scenarios there is much larger uplift at the deformation front (Figures 5.7 and 5.8), as also seen in the Cascadia and Winona trench-breaching rupture scenarios.

There is a major difference between the Haida Gwaii trench-breaching scenario and similar scenarios for Cascadia and Winona: The decrease in uplift as compared to the buried rupture scenario just landward of the near-trench high uplift is much more subdued. As explained in previous sections, the reduced uplift in this area is due to less internal shortening of the hanging wall than caused by a buried rupture. The effect is smaller at Haida Gwaii because the megathrust dips more steeply here, such that the overlying upper-plate wedge is thicker given the same distance from the trench. As a result, the uplift difference due to different amounts of internal shortening between buried or trench-breaching ruptures is smaller. In addition, the Haida Gwaii rupture is narrower in the downdip direction, especially when compared to Cascadia, so that the width of the area of reduced uplift in the trench-breaching scenarios is smaller. The small decrease in uplift over a small area is not expected to be adequate to offset the effect of the larger

uplift near the trench in tsunami generation. Therefore, the trench-breaching rupture at Haida Gwaii is expected to be more potent than the buried rupture in generating tsunami waves on the nearby coast. Greater slip reaching the trench (e.g., 100% of peak slip) is expected to generate a greater tsunami than less slip reaching the trench (e.g., 50%). Many studies suggest that the 2012 Haida Gwaii event had trench-breaching rupture (e.g., Figure 5.1b), which explains why it generated such as large tsunami. Trench-breaching rupture is probably more common than buried rupture at Haida Gwaii, and I suggest that it be assigned greater weight in tsunami hazard assessment in this region.

Like for the Cascadia and Winona models, the stress drop ($\Delta\sigma$) predicted by the Haida Gwaii models shows a sensitivity to the rupture type and geometrical fault properties. The margin-normal $\Delta\sigma$ change occurs over a short distance as seen in Figure 5.9, which reflects the effect of the slip distribution tapering to zero within a narrow ~30 km corridor. Stress drop results show very little variation along-strike until approaching the patch edge because the width of the rupture zone is rather uniform along-strike. For the area south of the *Mw* 7.8 2012 earthquake rupture region, the rapid change in deformation front orientation results in an extremely narrow rupture patch. With such a narrow rupture patch comes a very high $\overline{\Delta\sigma}$. However, the structural complexity of this area leads me to believe that this southern region is less capable of hosting a megathrust earthquake. As seen in results for Cascadia and Winona the $\overline{\Delta\sigma}$ calculated within the 1 m slip contour (10% of 10 m peak slip) is less for trench-breaching scenarios compared to buried rupture scenarios due to less alteration in the updip portion of slip. The higher $\overline{\Delta\sigma}$ for H-B-S is due to both a very narrow rupture (see equation 2.5 and related discussion in section 2.5) and not allowing the peak slip to breach the trench. The overall $\Delta\sigma$ distribution and $\overline{\Delta\sigma}$ results for the Haida Gwaii tsunami source scenarios are comparable in scale

to the other recorded megathrust earthquakes presented in the appendix.

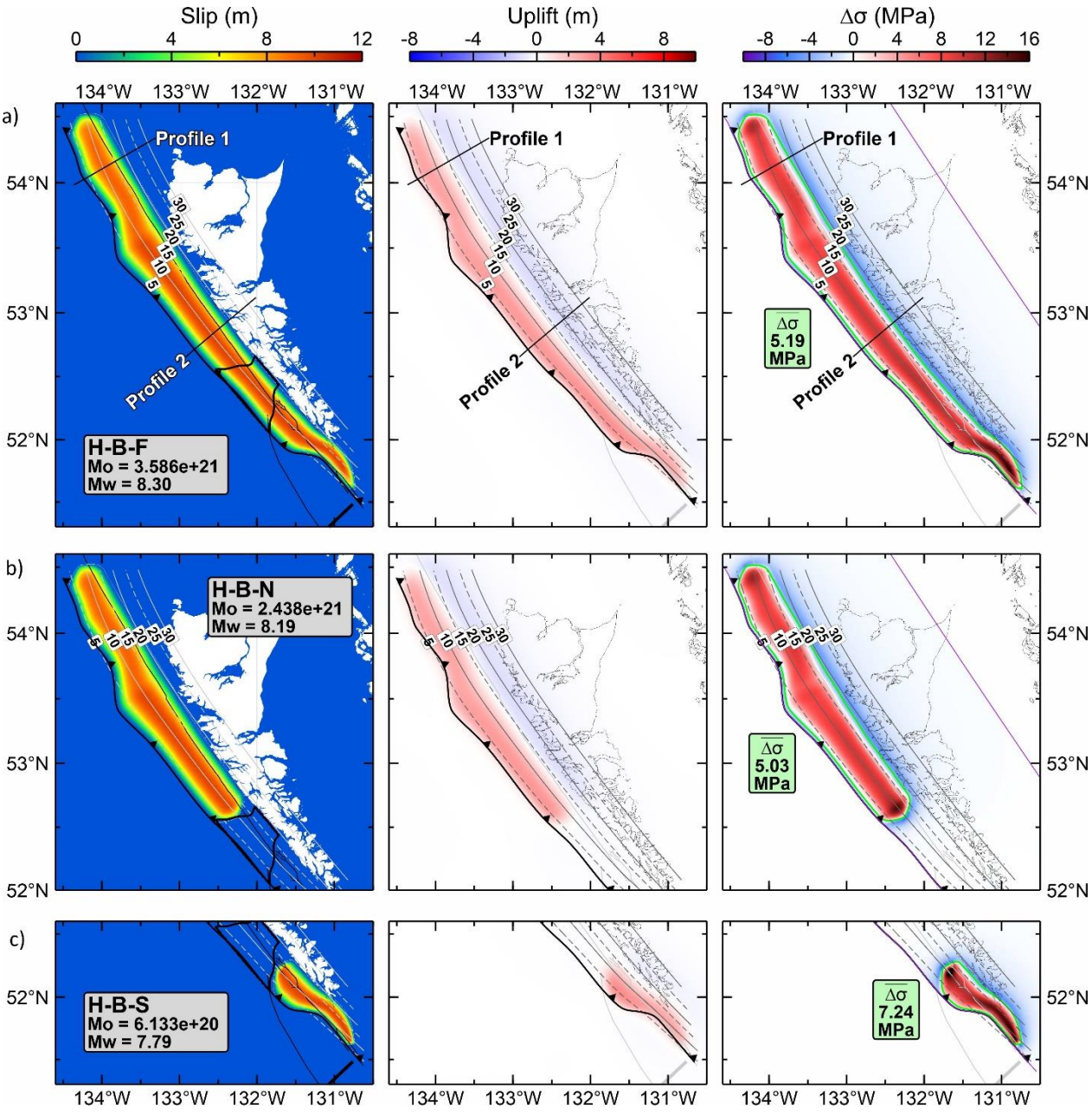

Figure 5.6. Buried rupture models for Haida Gwaii including a full-margin rupture (a) and scenarios where rupture occurs north (b) and south (c) of the *Mw* 7.8 2012 earthquake. From left to right in each row: slip, uplift, and stress drop. Thick black line in left panel is the 3 m slip contour of the *Mw* 7.8 2012 earthquake by Nykolaishen et al. (2015) (Figure 5.1). Green line in the right panel is the contour of 10% peak slip within which $\overline{\Delta\sigma}$ is calculated.

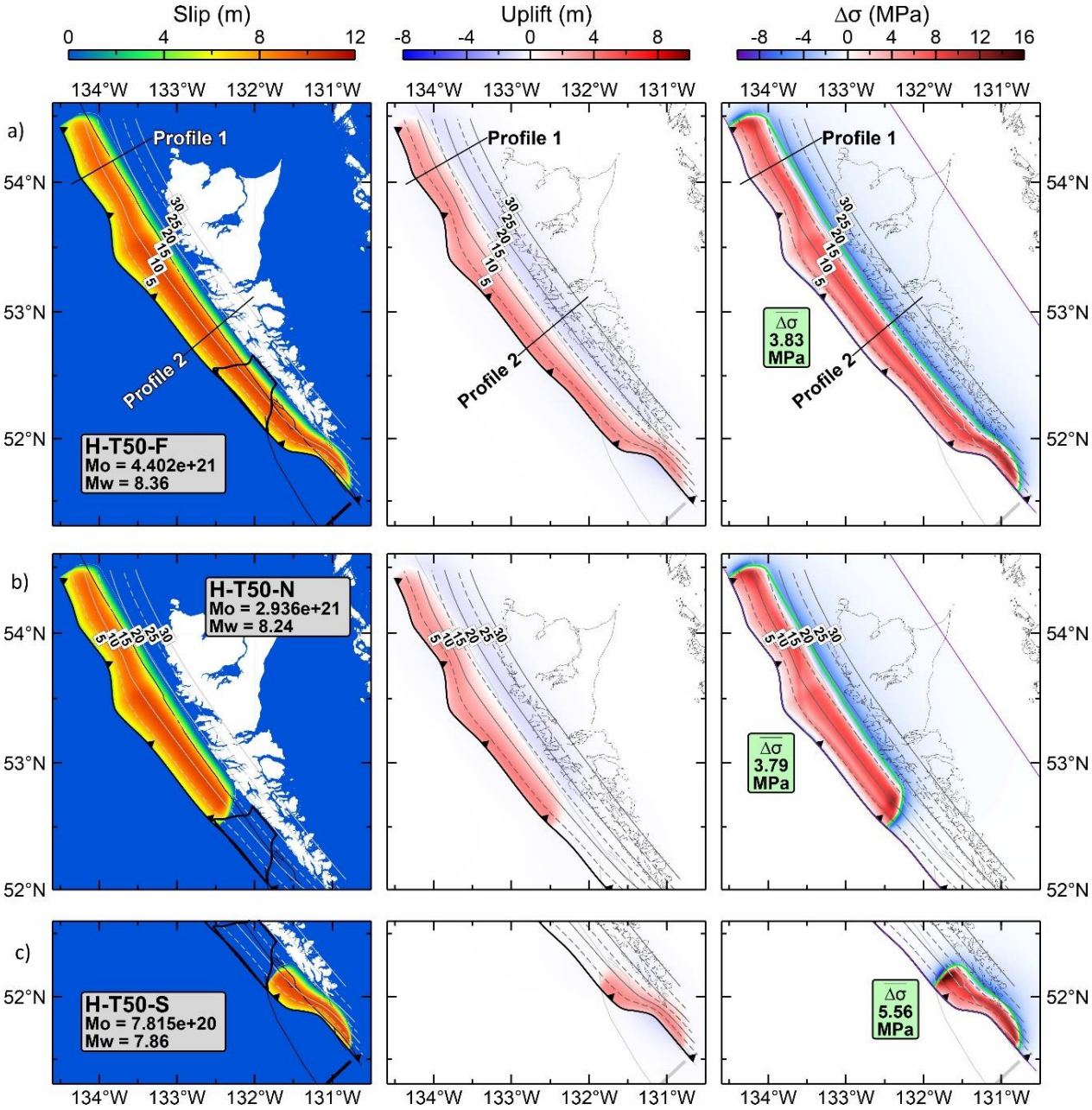

Figure 5.7. Trench-breaching rupture models for Haida Gwaii where 50% of peak slip reaches the trench. Models include full-margin rupture (a) and scenarios where rupture occurs north (b) and south (c) of the *Mw* 7.8 2012 earthquake. From left to right in each row: slip, uplift, and stress drop. Thick black line in left panel is the 3 m slip contour of the *Mw* 7.8 2012 earthquake by Nykolaishen et al. (2015) (Figure 5.1). Green line in the right panel is the contour of 10% peak slip within which $\overline{\Delta\sigma}$ is calculated.

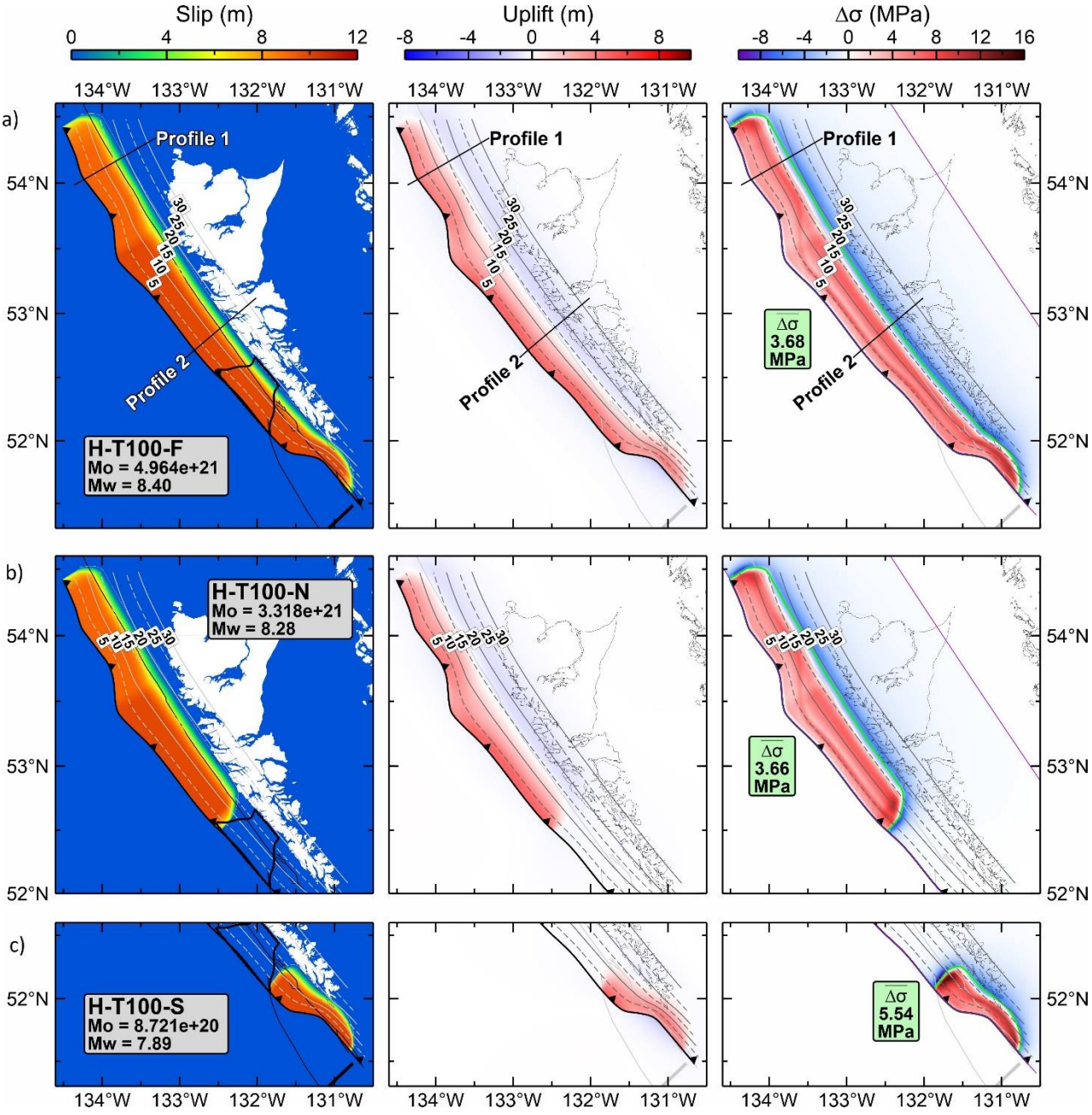

Figure 5.8. Trench-breaching rupture models for Haida Gwaii where 100% of peak slip reaches the trench. Models include full-margin rupture (a) and scenarios where rupture occurs north (b) and south (c) of the *Mw* 7.8 2012 earthquake. From left to right in each row: slip, uplift, and stress drop. Thick black line in left panel is the 3 m slip contour of the *Mw* 7.8 2012 earthquake by Nykolaishen et al. (2015) (Figure 5.1). Green line in the right panel is the contour of 10% peak slip within which $\overline{\Delta\sigma}$ is calculated.

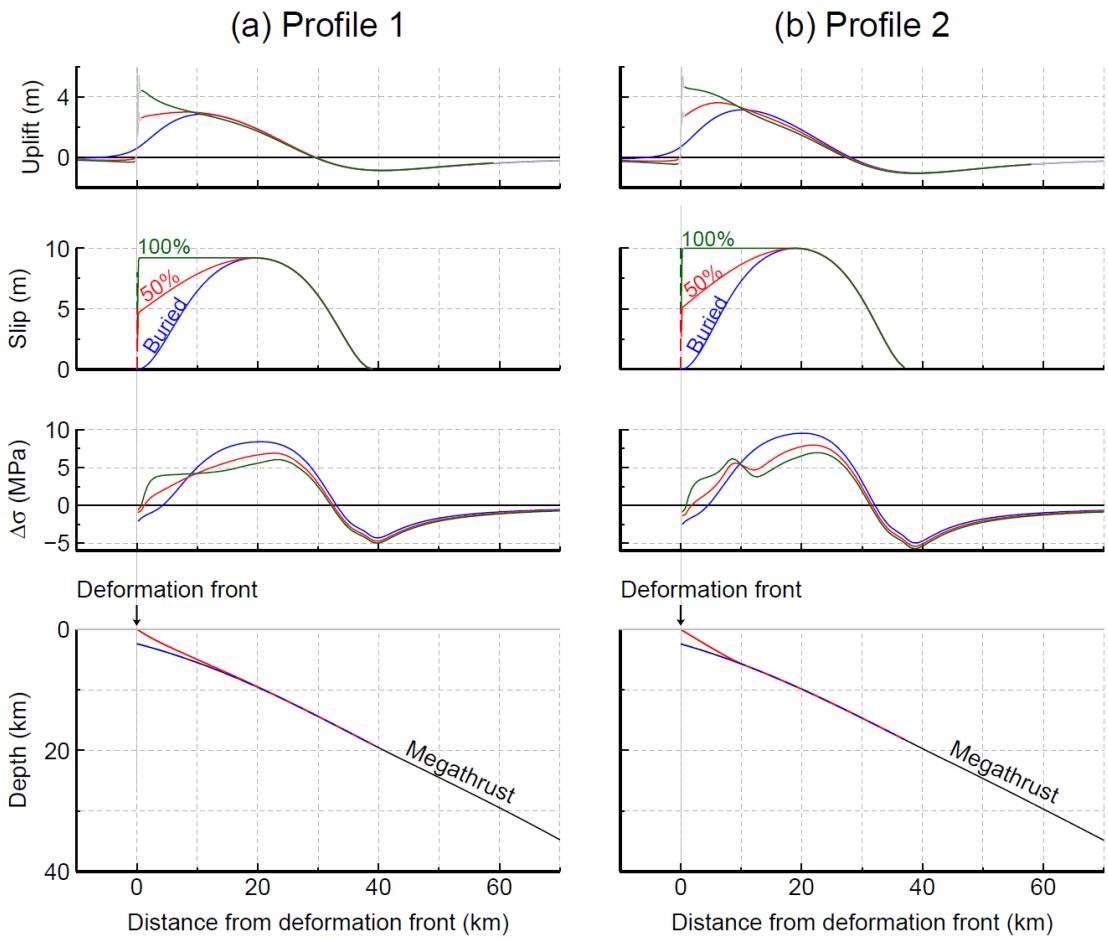

Figure 5.9. Fault slip, surface deformation, and stress drop of buried rupture and trench-breaching rupture models along profiles shown in Figures 5.6 and 5.7. Seafloor uplift, slip, stress drop on the fault, and fault geometry shown for each profile from top panels to bottom panels, respectively. Blue lines: Buried rupture model H-B-F. Trench-breaching models where 50% (H-T50-F) and 100% (H-T100-F) of the peak slip reaches the deformation front are shown with red and green lines, respectively. Red line in bottom panels shows the rupture zone for both trench-breaching scenarios, while the rupture zone for the buried rupture is a dashed green line here.

Chapter 6. Rupture Source Utilization for Tsunami Hazard Assessment

The rupture source improvements to Cascadia and Haida Gwaii scenarios and the addition of the Winona thrust as a potential source scenario will contribute to updating tsunami hazard assessment for the west coast of North America. There is a large range of possibilities in how the three study areas may experience tsunamigenic rupture. The tsunami sources given in this work still have a great deal of uncertainty. The tsunami sources provided are smoothed representations of different types of rupture seen for other subduction zones (Figure 1.2), but, in reality, future earthquake ruptures will most likely be much more complex. It is common practice that various scenarios are weighted by multi-disciplinary experts in hazard assessment. To systematically assess the tsunami source scenarios, logic trees are commonly used (Priest et al., 2009; Witter et al., 2011; Gao, 2016). Figures 6.1, 6.2, and 6.3 are examples to show how margin-normal slip distribution and rupture size may be used to construct simple logic trees for Cascadia, Winona, and Haida Gwaii, respectively, but there are also other ways to structure a logic tree.

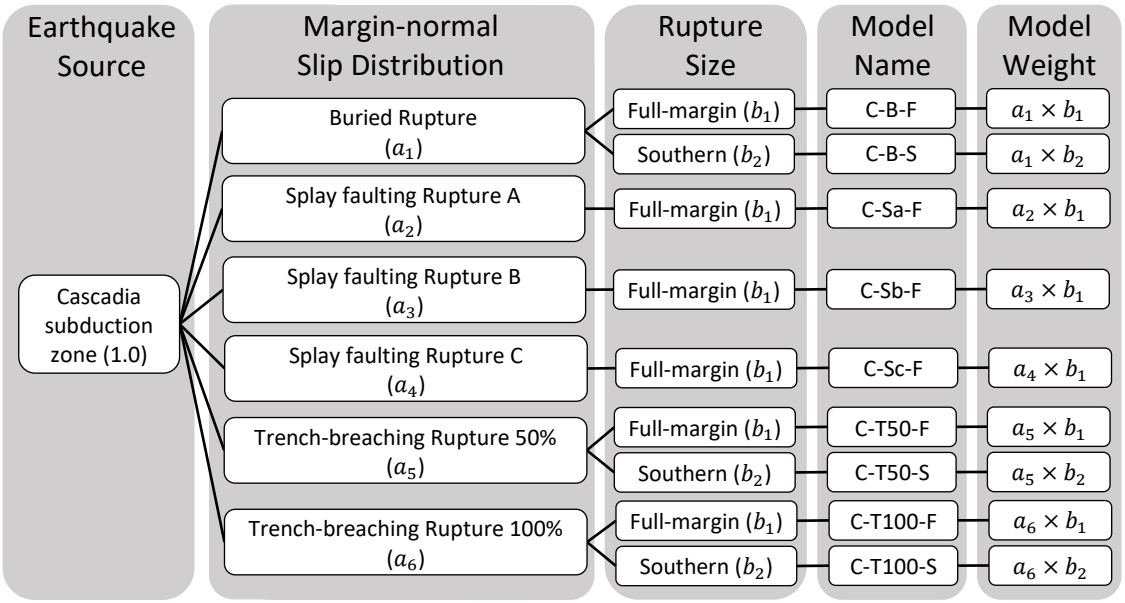

Figure 6.1. Logic tree to rank nine Cascadia rupture models. Weighting factors to be assigned by an expert committee.

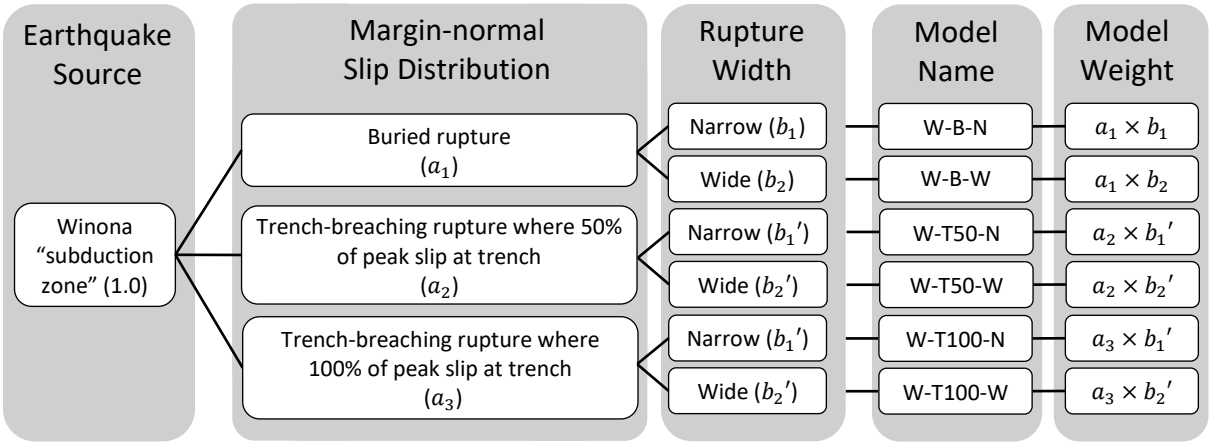

Figure 6.2. Logic tree to rank six Winona rupture models. Weighting factors to be assigned by an expert committee.

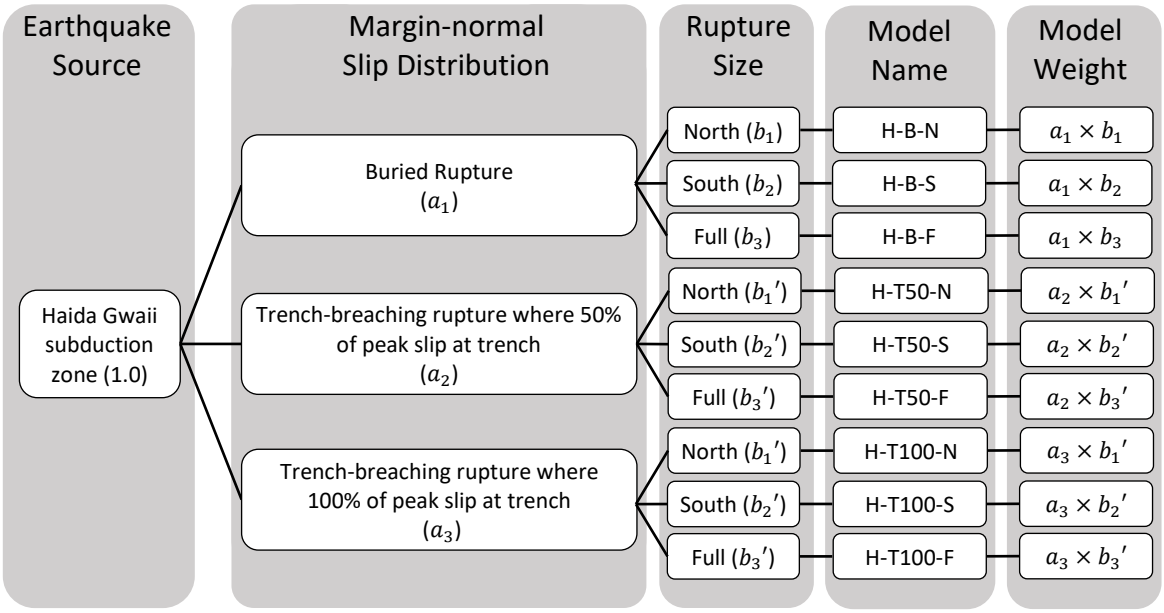

Figure 6.3. Logic tree to rank nine Haida Gwaii rupture models. Weighting factors to be assigned by an expert committee.

Gao et al. (2018) provided simulated water surface elevations for a full-margin buried rupture earthquake scenario and maximum sea surface elevations for a 10-hour period after the earthquake for full-margin buried, trench-breaching, and splay-faulting ruptures. The tsunami model results in that work were obtained by Dr. Tania L. Insua with modelling code FUNWAVE-TVD (Shi et al., 2012). For northern Cascadia the uplift calculated for each model

remains unchanged from Gao et al. (2018), and therefore the associated tsunami modelling results (Figures 6.4 and 6.5) in Gao et al. (2018) still apply. Dr. Yefei Bai of Zhejiang University, China, kindly reran the tsunami models based on the buried and splay-faulting rupture scenarios using modelling code NEOWAVE (Yamazaki et al., 2009; 2011). The results obtained with the two different codes are very similar (Figure 6.6).

A Cascadia full-margin buried rupture tsunami wave simulation time lapse given in Figure 6.4 demonstrates how the tsunami propagates towards and impacts the coast. Immediately after the earthquake the tsunami wave grows in size and spreads radially (Figure 6.4a). Over the course of 30 minutes, the tsunami wave front heading landward becomes irregular due to bathymetrical variations along the shelf and coast causing wave refraction, dispersion, and

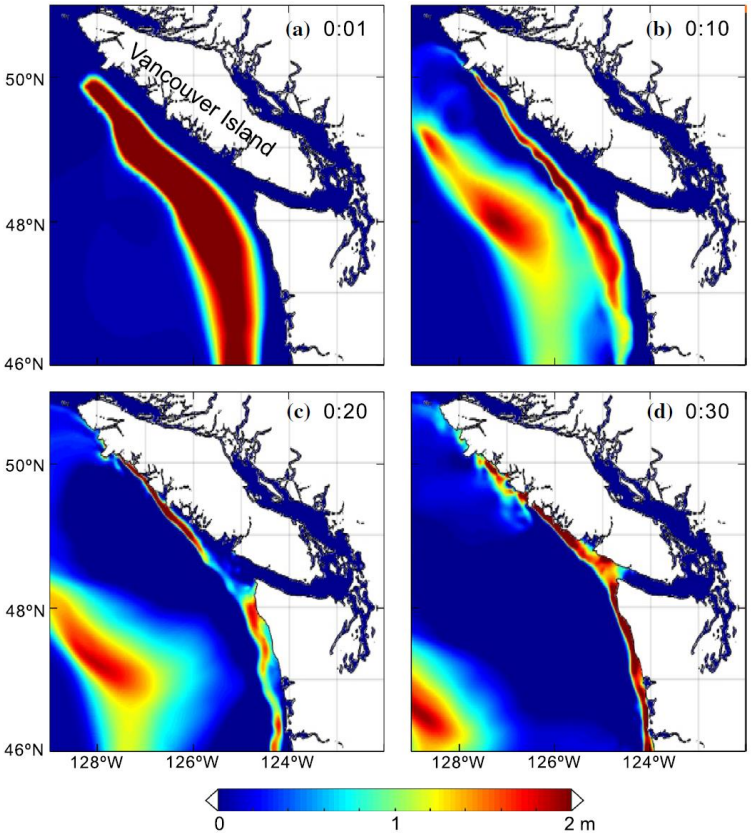

Figure 6.4. Time-lapse snap shots of tsunami wave propagation for a full-margin buried rupture scenario (figure from Gao et al., 2018). Panels show water surface elevation (m) at 1, 10, 20, and 30 minutes after the earthquake.

convergence (Figure 6.4). In the tsunami simulations presented by Gao et al. (2018) for the splay-faulting and trench-breaching scenarios, the wave behaved similarly to the buried rupture, but with sharper wave fronts due to a large amount of uplift near the splay or frontal thrust traces.

Gao et al. (2018) found that for most of northern Cascadia the maximum coastal wave height experienced over the course of a 10-hour period after the earthquake is largest for splay faulting rupture scenarios, followed by buried rupture, and lastly by trench breaching scenarios (Figure 6.5). The splay fault scenario they present shows significantly more uplift closer to shore compared to the buried rupture scenario, which is the reason why the maximum coastal wave heights for the splay faulting scenario are much larger. Even though the trench-breaching scenario has much more uplift immediately adjacent to the deformation front compared to the buried rupture scenario, its coastal wave height results are generally less due to the smaller uplift further landward of the deformation front (as discussed in section 3.3.4). However, for a small area of northern Vancouver Island where there is no assumed splay fault, their results show that the trench-breaching scenario yields greater coastal wave heights than does the buried rupture. In

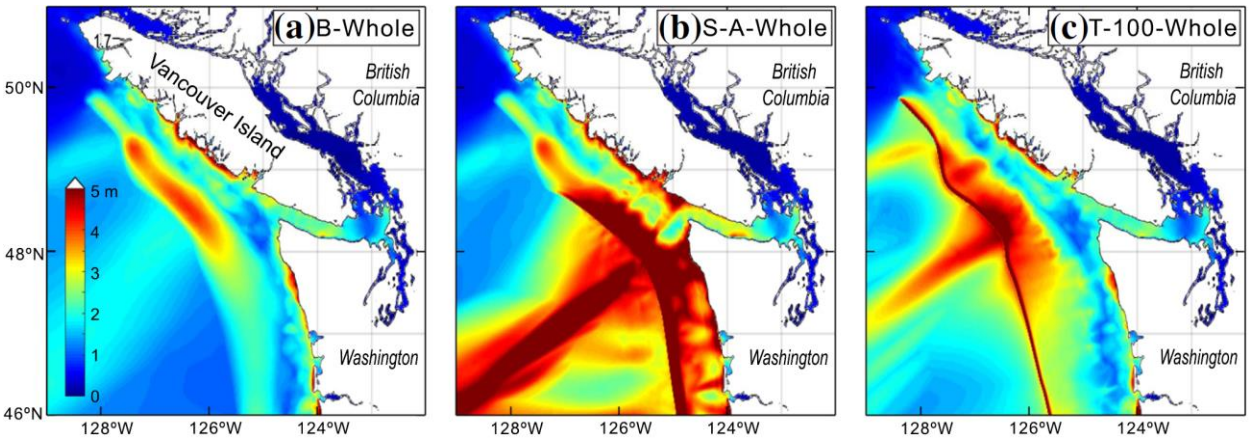

Figure 6.5. Maximum water surface elevation within 10 hours following the earthquake for full-margin buried rupture, splay faulting rupture and trench-breaching rupture scenarios (from Gao et al., 2018).

this area, the deformation front is closer to the coast allowing for the effects of the near trench peak in uplift out-weighing the slightly further landward small reduction in uplift compared to buried rupture.

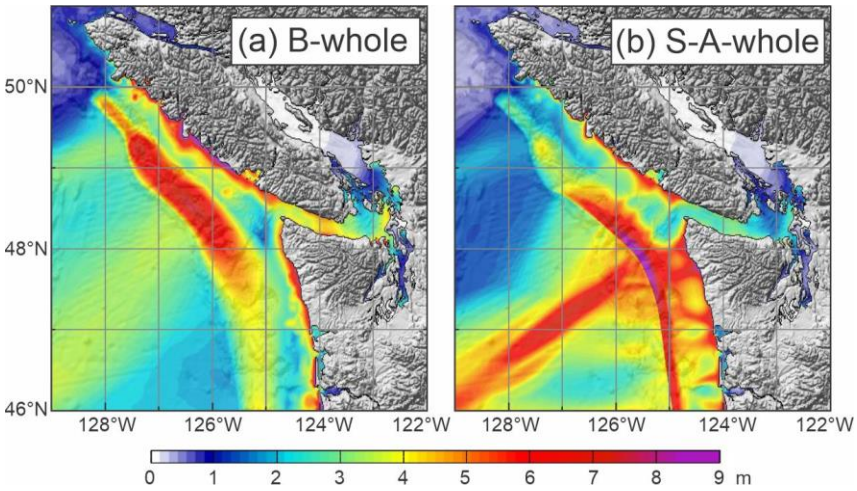

Figure 6.6. Maximum water surface elevation within 10 hours following the earthquake for the same full-margin buried rupture and splay faulting rupture scenarios used in Gao et al. (2018) calculated by Dr. Yefei Bai.

Chapter 7. Conclusions and Recommendations for Future Research

7.1. Conclusions

The main objectives of this thesis include developing tsunami source scenarios for Cascadia (Chapter 3), Winona (Chapter 4), and Haida Gwaii (Chapter 5) and new 1700 Cascadia megathrust earthquake rupture scenarios that fit updated coastal subsidence estimates (Chapter 3). To create these 3-D dislocation rupture models, I constructed or refined megathrust geometries, assessed and assigned potential rupture bound controls, and determined slip magnitude (in terms of slip deficit recovered by the rupture) and direction with a varying amount of information for each study area. The tsunami source and paleoseismic models throughout this work show that various types of megathrust rupture (buried rupture, splay-faulting rupture, and trench-breaching rupture) can produce large seafloor uplift and coastal subsidence, resulting in large destructive tsunamis that will impact the west coast of North America.

For Cascadia, I provide five rupture models that can fit updated microfossil-based paleoseismic coastal subsidence estimations for the 1700 Cascadia megathrust earthquake and nine tsunami source models that can be used in a tsunami hazard assessment of the west coast. Updated 1700 paleoseismic coastal subsidence estimations indicate greater along-strike variability than previously seen, which necessitates more rapid along-strike slip distribution changes and hence slightly more complex slip models. Five of the nine Cascadia tsunami source models presented in this work are very similar to some of the Gao et al. (2018) models, except for southern Cascadia where the fault geometry has been modified (section 3.1). Additionally, I constructed a new splay scenario on the grounds that seismic reflection images and bathymetric evidence indicate its possible presence between the two splay faults proposed by Gao et al. (2018). Tsunami modelling shows that of the three types of Cascadia rupture the splay-fault

models generate the largest tsunami waves. Buried and trench-breaching rupture models generate similar smaller waves that affect the coastline, with slightly higher waves for the buried rupture.

For Winona, the six scenarios presented in this work are the first tsunami source scenarios published for this part of the continental margin. Through examination of seismic images I was able to construct a Winona block surface geometry. Scenarios created include buried rupture and trench-breaching rupture. The latter breaches the west side of the Winona ridge via an assumed frontal thrust. There is great uncertainty in the dimensions of the possible rupture region on the "megathrust", and therefore I have provided both narrow and wide scenarios. It is highly debated whether the Winona block could host such an earthquake. Given the very limited supporting data, the weighting of its hazard should be low.

For Haida Gwaii the nine tsunami source scenarios presented in this work are the first tsunami source scenarios for this margin involving a curved 3-D fault geometry and different rupture types over the length of the margin where there is possible plate subduction. I created a fault geometry for Haida Gwaii by interpolating depth estimations sourced from receiver functions and seismic reflection images. I constructed both buried rupture and trench-breaching scenarios for areas north and south of the *Mw* 7.8 2012 Haida Gwaii earthquake, as well as for full-margin rupture propagation through the 2012 rupture zone. Due to the close proximity of the trench to the coastline, a larger tsunami wave along the coastline is expected from trench breaching models compared to buried rupture models. This an important difference from the Cascadia and Winona scenarios. Various studies indeed indicate that the 2012 earthquake ruptured to the trench.

In general, megathrust earthquakes exhibit an average stress drop ($\overline{\Delta\sigma}$) of a few MPa, as

demonstrated by the 11 recent examples found in the appendix. Various rupture scenarios presented throughout this work show a larger $\overline{\Delta\sigma}$, including some small rupture patches with high amount of slip required to fit the rapid changes in coastal subsidence for the 1700 Cascadia earthquake and some of the narrow tsunami source scenarios. Tsunami source scenarios in this work that show $\overline{\Delta\sigma}$ greater than 4 MPa include C-B-S, W-B-N, H-B-F, H-B-N, H-B-S, H-T50-S, H-T100-S, but they are all still within the same order of magnitude as real earthquakes and can still be deemed mechanically reasonable. Also, to arrive at this conclusion the general distribution and smoothness of $\Delta\sigma$ was also considered. Some of the commonalities and differences between the $\Delta\sigma$ results include: (1) Given similar slip magnitude, the $\overline{\Delta\sigma}$ of a rupture increases with the narrowing of the rupture region, consistent with equation 2.5. (2) The $\overline{\Delta\sigma}$ is lower for trench-breaching scenarios due to the lower margin-normal slip gradient between the trench and the peak slip. (3) In full-margin Cascadia tsunami source scenarios, $\overline{\Delta\sigma}$ is higher for the splay-faulting rupture than for the buried rupture, because the former has a smaller rupture dimension. However, for some of the smaller rupture patches used to fit the 1700 paleoseismic coastal subsidence estimations, the splay-faulting scenario $\overline{\Delta\sigma}$ is lower, because the effect of allowing the rupture to breach the seafloor reducing the $\overline{\Delta\sigma}$ outweighs the effect of the smaller rupture dimension.

7.2. Recommendations for Future Research

Paucity of observational constraints presents the greatest challenge to constructing slab/block surface geometry. Currently, there are no receiver function data available for the southwestern coast of Haida Gwaii, northern Haida Gwaii, and northwestern Vancouver Island. More receiver function data in these areas will help to define a more accurate fault surface and resolve whether a slab/block is even present in some areas such as north, south, or east of the

Haida Gwaii archipelago, under the northwestern tip of Vancouver Island, and below the continental shelf west of the Winona Basin. The furthest downdip extent of the tilted Winona block is unknown, but receiver-function monitoring on the small islands just northwest of Vancouver Island may help resolve this question.

As mentioned in section 3.3 the downdip rupture limit for most of Cascadia (except the Explorer segment) is set to be the halfway point of the ETZ defined by Wang et al. (2003). Thermal constraints used in their modelling include a 450°C isotherm interpolated from three 2-D thermal model profiles (Hyndman and Wang, 1993). More thermal modelling along strike to better contrain the Cascadia thermal model would better resolve the 450°C isotherm and resulting effective transition zone.

In seismic reflection lines 85-01 and 85-02 it appears as though there are minor offsets masked by the BSR at the locations where I propose the presence of a splay fault (C). A major seismic survey planned to happen in 2020 may resolve whether this is a northern extension of a major splay fault off the coast of Oregon proposed by Priest et al. (2010).

Assessing tsunami hazards along the west coast of North America requires multi-disciplinary expert evaluation of rupture scenarios such as those presented in this work. For example, the scenarios can be weighted in a logic tree by an expert committee. In chapter 6, I provide a simple logic tree example for each study area, where the scenarios are arranged based on their margin-normal slip distribution and rupture size/width. Other factors such as earthquake size variability should also be taken into consideration.

References

Atwater, T., & Stock, J. (1998). Pacific-North America Plate Tectonics of the Neogene Southwestern United States: An Update. *International Geology Review*, *40*(5), 375–402. doi:10.1080/00206819809465216

Baba, T., Cummins, P. R., Hori, T., & Kaneda, Y. (2006). High precision slip distribution of the 1944 Tonankai earthquake inferred from tsunami waveforms: Possible slip on a splay fault. *Tectonophysics*, *426*, 119–134. doi:10.1016/j.tecto.2006.02.015

Briggs, R. W., Sieh, K., Meltzner, A. J., Natawidjaja, D., Galetzka, J., Suwargadi, B., Hsu, Y. J., Simons, M., Hananto, N., Suprihanto, I., Prayudi, D., Avouac, J. P., Prawirodirdjo, L., & Bock, Y. (2006). Deformation and Slip Along the Sunda Megathrust in the Great 2005 Nias-Simeulue Earthquake. *Science*, *311*(5769), 1897–1901. doi:10.1126/science.1122602

Brown, L. (2015). *Strength of Megathrust Faults: Insights from the 2011 M=9 Tohoku-oki Earthquake* (Masters Thesis). Victoria, BC: University of Victoria. Retrieved from http://hdl.handle.net/1828/6581

Brown, L., Wang, K., & Sun, T. (2015). Static stress drop in the Mw 9 Tohoku-oki earthquake: Heterogeneous distribution and low average value. *Geophysical Research Letters*, *42*(24), 10595-10600. doi:10.1002/2015GL066361

Brudzinski, M. R., & Allen, R. M. (2007). Segmentation in episodic tremor and slip all along Cascadia. *Geology*, *35*(10), 907–910. doi:10.1130/G23740A.1

Bustin, A. M., Hyndman, R. D., Kao, H., & Cassidy, J. F. (2007). Evidence for underthrusting beneath the Queen Charlotte Margin, British Columbia, from teleseismic receiver function

analysis. *Geophysical Journal International, 171*(3), 1198–1211. doi:10.1111/j.1365-246X.2007.03583.x

Cárdenas-Jirón, L. A. (2013). *The Chilean Earthquake and Tsunami 2010: A multidisciplinary study of Mw8.8, Maule*. Southampton, UK: WIT Press.

Davis, E. E. (1982). Evidence for extensive basalt flows on the sea floor. *Geological Society of America Bulletin, 93*(10), 1023–1029. doi:10.1130/0016-7606(1982)93<1023:EFEBFO>2.0.CO;2

Davis, E. E., & Clowes, R. M. (1986). High velocities and seismic anisotropy in Pleistocene turbidites off Western Canada. *Geophysical Journal of the Royal Astronomical Society, 84*(2), 381–400. doi:10.1111/j.1365-246X.1986.tb04361.x

Davis, E. E., & Riddihough, R. P. (1982). The Winona Basin: structure and tectonic. *Canadian Journal of Earth Sciences, 19*(4), 767–788. doi:10.1139/e82-065

Davis, E. E., & Seemann, D. A. (1981). A compilation of seismic reflection profiles across the continental margin of western Canada. *Geological Survey of Canada, Open File 751*. doi:10.4095/129686

DeMets, C., & Merkouriev, S. (2016). High-resolution reconstructions of Pacific–North America plate motion: 20 Ma to present. *Geophysical Journal International, 207*(2), 741–773. doi:10.1093/gji/ggw305

Ferguson, R., King, H. M., Kublik, K., Rohr, K. M., Kung, L., Lister, C. J., Fustic, M., Hayward, N., Brent, T. A., & Jassim, Y. (2018). Petroleum, mineral, and other resource potential in the offshore Pacific, British Columbia, Canada. *Geological Survey of Canada, Open File 8390*, 82 p. doi:10.4095/308395

Fine, I. V., Cherniawsky, J. Y., Thomson, R. E., Rabinovich, A. B., & Krassovski, M. V. (2015). Observations and Numerical Modeling of the 2012 Haida Gwaii Tsunami off the Coast of British Columbia. *Pure and Applied Geophysics, 172*(3-4), 699–718. doi:10.1007/s00024-014-1012-7

Flück, P., Hyndman, R. D., & Wang, K. (1997). Three-dimensional dislocation model for great earthquakes of the Cascadia Subduction Zone. *Journal of Geophysical Research, 102*(B9), 20539–20550. doi:10.1029/97JB01642

Fujiwara, T., Kodaira, S., No, T., Kaiho, Y., Takahashi, N., & Kaneda, Y. (2011). The 2011 Tohoku-Oki Earthquake: Displacement Reaching the Trench Axis. *Science, 334*(6060), 1240. doi:10.1126/science.1211554

Gao, D. (2016). *Defining Megathrust Tsunami Sources at Northernmost Cascadia Using Thermal and Structural Information* (Masters Thesis). Victoria, BC: University of Victoria. Retrieved from http://hdl.handle.net/1828/7435

Gao, D., Wang, K., Davis, E. E., Jiang, Y., Insua, T. L., & He, J. (2017). Thermal state of the Explorer segment of the Cascadia subduction zone: Implications for seismic and tsunami hazards. *Geochemistry, Geophysics, Geosystems, 18*(4), 1569–1579. doi:10.1002/2017GC006821

Gao, D., Wang, K., Insua, T. L., Sypus, M., Riedel, M., & Sun, T. (2018). Defining megathrust tsunami source scenarios for northernmost Cascadia. *Natural Hazards, 94*(1). doi:10.1007/s11069-018-3397-6

Goldfinger, C., Galer, S., Beeson, J., Hamilton, T., Black, B., Romsos, C., Patton, J., Nelson, C. H., Hausmann, R., & Morey, A. (2017). The importance of site selection, sediment supply,

and hydrodynamics: A case study of submarine paleoseismology on the northern Cascadia margin, Washington USA. Marine *Geology, 384*, 4–46. doi:10.1016/j.margeo.2016.06.008

Goldfinger, C., Nelson, C., Morey, A., Johnson, J., Patton, J., Karabanov, E., Gutiérrez-Pastor, J., Eriksson, A. T., Gràcia, E., Dunhill, G., Enkin, R. J., Dallimore., A., & Vallier, T. (2012). Turbidite event history: Methods and implications for Holocene paleoseismicity of the Cascadia subduction zone. *U.S. Geological Survey Professional Paper 1661-F*, 184 p. doi:10.3133/pp1661F

Gosselin, J. M., Cassidy, J. F., & Dosso, S. E. (2015). Shear-Wave Velocity Structure in the Vicinity of the 2012 Mw 7.8 Haida Gwaii Earthquake from Receiver Function Inversion. *Bulletin of the Seismological Society of America*, *105*(2B), 1106–1113. doi:10.1785/0120140171

Hayes, G. P., Moore, G. L., Portner, D. E., Hearne, M., Flamme, H., Furtney, M., & Smoczyk, G. M. (2018). Slab2, a comprehensive subduction zone geometry model. *Science, 362*(6410), 58–61. doi:10.1126/science.aat4723

Hsu, Y.-J., Simons, M., Avouac, J.-P., Galetzka, J., Sieh, K., Chlieh, M., Natawidjaja, D., Prawirodirdjo, L., & Bock, Y. (2006). Frictional Afterslip Following the 2005 Nias-Simeulue Earthquake, Sumatra. *Science, 312*(5782), 1921–1926. doi:10.1126/science.1126960

Hyndman, R. D., & Ellis, R. M. (1981). Queen Charlotte fault zone: microearthquakes from a temporary array of land stations and ocean bottom seismograph. *Canadian Journal of Earth Sciences, 18*(4), 776–788. doi:10.1139/e81-071

Hyndman, R. D., & Wang, K. (1993). Thermal Constraints on the Zone of Major Thrust

Earthquake Failure: The Cascadia Subduction Zone. *Journal of Geophysical Research, 98*(B2), 2039–2060. doi:10.1029/92JB02279

Hyndman, R. D., & Wang, K. (1995). The rupture zone of Cascadia great earthquakes from current deformation and the thermal regime. *Journal of Geophysical Research, 100*(B11), 22133–22154. doi:10.1029/95JB01970

Iinuma, T., Hino, R., Kido, M., Inazu, D., Osada, Y., Ito, Y., Ohzono, M., Tsushima, H., Suzuki, S., Fujimoto, H., & Miura, S. (2012). Coseismic slip distribution of the 2011 off the Pacific Coast of Tohoku Earthquake (M9.0) refined by means of seafloor geodetic data. *Journal of Geophysical Research, 117*, B07409. doi:10.1029/2012JB009186

Kemp, A. C., Cahill, N., Engelhart, S. E., Hawkes, A. D., & Wang, K. (2018). Revising Estimates of Spatially Variable Subsidence during the A.D. 1700 Cascadia Earthquake Using a Bayesian Foraminiferal Transfer Function. *Bulletin of the Seismological Society of America, 108*(2), 654–673. doi:10.1785/0120170269

Konca, A. O., Hjorleifsdottir, V., Song, T.-R. A., Avouac, J.-P., Helmberger, D. V., Ji, C., Sieh, K., Briggs, R., & Meltzner, A. (2007). Rupture Kinematics of the 2005 Mw 8.6 Nias–Simeulue Earthquake from the Joint Inversion of Seismic and Geodetic Data. *Bulletin of the Seismological Society of America, 97*(1A), S307–S322. doi:10.1785/0120050632

Lay, T., Kanamori, H., Ammon, C. J., Nettles, M., Ward, S. N., Aster, R. C., Beck, S. L., Bilek, S. L., Brudzinski, M. R., Butler, R., DeShon, H. R., Ekström, G., Satake K., Sipkin, S. (2005). The Great Sumatra-Andaman Earthquake of 26 December 2004. *Science, 308*(5725), 1127–1133. doi:10.1126/science.1112250

Lay, T., Ye, L., Kanamori, H., Yamazaki, Y., Cheung, K. F., Kwong, K., & Koper, K. D. (2013).

The October 28, 2012 Mw 7.8 Haida Gwaii underthrusting earthquake and tsunami: Slip partitioning along the Queen Charlotte Fault transpressional plate boundary. *Earth and Planetary Science Letters, 375*, 57–70. doi:10.1016/j.epsl.2013.05.005

Leonard, L. J., & Bednarski, J. M. (2014). Field Survey Following the 28 October 2012 Haida Gwaii Tsunami. *Pure and Applied Geophysics, 171*(12), 3467–3482. doi:10.1007/s00024-014-0792-0

Leonard, L. J., Rogers, G. C., & Mazzotti, S. (2012). A Preliminary Tsunami Hazard Assessment of the Canadian Coastline. *Geological Survey of Canada, Open File 7201*, 126 p. doi:10.4095/292067

Leonard, L. J., Rogers, G. C., & Mazzotti, S. (2014). Tsunami hazard assessment of Canada. *Natural Hazards, 70*(1), 237–274. doi:10.1007/s11069-013-0809-5

Madariaga, R. (1979). On the Relation Between Seismic Moment and Stress Drop in the Presence of Stress and Strength Heterogeneity. *Journal of Geophysical Research: Solid Earth, 84*(B5), 2243–2250. doi:10.1029/JB084iB05p02243

Mann, D. M., & Snavely, P. D. (1984). Multichannel seismic reflection profiles collected in 1977 in the eastern Pacific Ocean off of the Washington/Oregon coast: *U.S. Geological Survey Open-File Report 84-5*. doi:10.3133/ofr845

Mazzotti, S., Hyndman, R. D., Flück, P., Smith, A. J., & Schmidt, M. (2003). Distribution of the Pacific/North America motion in the Queen Charlotte Islands-S. Alaska plate boundary zone. Geophysical Research Letters, 30(14), 1762. doi:10.1029/2003GL017586

McCrory, P. A., Blair, J. L., Oppenheimer, D. H., & Walter, S. R. (2004). Depth to the Juan De Fuca Slab Beneath the Cascadia Subduction Margin–A 3-D Model for Sorting

Earthquakes. US Geological Survey, US Department of Interior. doi:10.3133/ds91

McCrory, P. A., Blair, J. L., Waldhauser, F., & Oppenheimer, D. H. (2012). Juan de Fuca slab geometry and its relation to Wadati-Benioff zone seismicity. *Journal of Geophysical Research: Solid Earth, 117*(9), B09306. doi:10.1029/2012JB009407

Moreno, M., Melnick, D., Rosenau, M., Baez, J., Klotz, J., Oncken, O., A.Tassara, A., Chen, J., Bataille, K., Bevis, M., Socquet, A., Bolte, J., Vigny, C., Brooks, B., Ryder, I., Grund, V., Smalley, B., Carrizo, D., Bartsch, M., & Hase, H. (2012). Toward understanding tectonic control on the M_w 8.8 2010 Maule Chile earthquake. *Earth and Planetary Science Letters, 321*, 152–165. doi:10.1016/j.epsl.2012.01.006

Moreno, M., Melnick, D., Rosenau, M., Bolte, J., Klotz, J., Echtler, H., Baez, J., Bataille, K., Chen, J., Bevis, M., Hase, H., & Oncken, O. (2011). Heterogeneous plate locking in the South–Central Chile subduction zone: Building up the next great earthquake. *Earth and Planetary Science Letters, 305*, 412–424. doi:10.1016/j.epsl.2011.03.025

Noda, H., & Lapusta, N. (2013). Stable creeping fault segments can become destructive as a result of dynamic weakening. *Nature, 493*(7433), 518–521. doi:10.1038/nature11703

Noda, H., Lapusta, N., & Kanamori, H. (2013). Comparison of average stress drop measures for ruptures with heterogeneous stress change and implications for earthquake physics. *Geophysical Journal International, 193*(3), 1691–1712. doi:10.1093/gji/ggt074

Nykolaishen, L., Dragert, H., Wang, K., James, T. S., & Schmidt, M. (2015). GPS Observations of Crustal Deformation Associated with the 2012 Mw 7.8 Haida Gwaii Earthquake. *Bulletin of the Seismological Society of America, 105*(2B), 1241–1252. doi:10.1785/0120140177

Okada, Y. (1992). Internal deformation due to shear and tensile faults in a half-space. *Journal of Geophysical Research, 82*(2), 1018–1040. doi:10.1029/92JB00178

Priest, G. R., Goldfinger, C., Wang, K., Witter, R. C., Zhang, Y., & Baptista, A. M. (2009). Tsunami Hazard Assessment of the Northern Oregon Coast: A Multi-deterministic Approach Tested at Cannon Beach, Clatsop County, Oregon. *Oregon Department of Geology Mineral Industries Special Paper 41*, 87 p.

Priest, G. R., Goldfinger, C., Wang, K., Witter, R. C., Zhang, Y., & Baptista, A. M. (2010). Confidence levels for tsunami-inundation limits in northern Oregon inferred from a 10,000-year history of great earthquakes at the Cascadia subduction zone. *Natural Hazards, 54*(1), 27–73. doi:10.1007/s11069-009-9453-5

Pritchard, C. J. (2004). *Late Holocene relative sea-level changes, Arcata Bay, California: evaluation of freshwater syncline movement using coseismically buried soil horizons* (Masters Thesis). Arcata, California: Humboldt State University. Retrieved from http://humboldt-dspace.calstate.edu/handle/2148/883

Remy, D., Perfettini, H., Cotte, N., Avouac, J. P., Chlieh, M., Bondoux, F., Sladen, A., Tavera, H., & Socquet, A. (2016). Postseismic relocking of the subduction megathrust following the 2007 Pisco, Peru, earthquake. *Journal of Geophysical Research: Solid Earth, 121(*5), 3978–3995. doi:10.1002/2015JB012417

Riedel, M., & Rohr, K. M. (2012). Gas hydrate within the Winona Basin, offshore western Canada. *Marine and Petroleum Geology, 30*(1), 66–80. doi:10.1016/j.marpetgeo.2011.10.009

Riedel, M., Côté, M. M., & Neelands, P. J. (2014a). Cruise Report 2012005PGC - The Mw 7.7

Haida Gwaii Earthquake Ocean Bottom Seismometer Experiment - Instrument deployment, gas-plume acoustic imaging, and water sampling. *Geological Survey of Canada, Open File 7555*, 34 p. doi:10.4095/293918

Riedel, M., Côté, M. M., Neelands, P. J., Middleton, G., Standen, G., Iuliucci, R., Ulmi, M., Stacey, C. D., Murphy, R., Manning, D., Brillon, C., & Spence, G. D. (2014b). 2012 Haida Gwaii Mw 7.7 earthquake response-Ocean bottom seismometer relocation and geophone orientation analysis and quality control of wide-angle P-wave refraction data. *Geological Survey of Canada, Open File 7632*, 77 p. doi:10.4095/295551

Rohr, K. M. (2015). Plate Boundary Adjustments of the Southernmost Queen Charlotte Fault. *Bulletin of the Seismological Society of America, 105*(2B), 1076–1089. doi:10.1785/0120140162

Rohr, K. M., Scheidhauer, M., & Tréhu, A. M. (2000). Transpression between two warm mafic plates: The Queen Charlotte Fault revisited. *Journal of Geophysical Research, 105*(B4), 8147–8172. doi:10.1029/1999JB900403

Rohr, K. M., & Tryon, A. J. (2010). Pacific-North America plate boundary reorganization in response to a change in relative plate motion: Offshore Canada. *Geochemistry Geophysics Geosystems, 11*, Q06007. doi:10.1029/2009GC003019

Satake, K., Wang, K., & Atwater, B. F. (2003). Fault slip and seismic moment of the 1700 Cascadia earthquake inferred from Japanese tsunami descriptions. *Journal of Geophysical Research, 108*(B11), 2535. doi:10.1029/2003JB002521

Scholz, C. H. (2002). *The Mechanics of Earthquakes and Faulting* (2 ed.). Cambridge, UK: Cambridge University Press.

Scholz, C. H. (2014). Holocene Earthquake History of Cascadia: A Quantitative Test. *Bulletin of the Seismological Society of America, 104*(4), 2120–2124. doi:10.1785/0120140002

Shao, G., & Ji, C. (2013). Preliminary Result of the Oct 28, 2012 Mw 7.72 Canada Earthquake. Retrieved June 16, 2019, from University of California, Santa Barbara: http://www.geol.ucsb.edu/faculty/ji/big_earthquakes/2012/10/canada.html

Shennan, I., Long, A. J., Rutherford, M. M., Green, F. M., Innes, J. B., Lloyd, J. M., Zong, Y. Walker, K. J. (1996). Tidal marsh stratigraphy, sea-level change and large earthquakes, i: a 5000 year record in Washington, U.S.A. *Quaternary Science Reviews, 15*(10), 1023–1059. doi:10.1016/S0277-3791(96)00007-8

Shi, F., Kirby, J. T., Harris, J. C., Geiman, J. D., & Grilli, S. T. (2012). A high-order adaptive time-stepping TVD solver for Boussinesq modeling of breaking waves and coastal inundation. *Ocean Modelling, 43*, 36–51. doi:10.1016/j.ocemod.2011.12.004

Smith, A. J., Hyndman, R. D., Cassidy, J. F., & Wang, K. (2003). Structure, seismicity, and thermal regime of the Queen Charlotte Transform Margin. *Journal of Geophysical Research, 108*(B11), 2539. doi:10.1029/2002JB002247

Spence, G. D., & Long, D. T. (1995). Transition from oceanic to continental crustal structure: seismic and gravity models at the Queen Charlotte transform margin. *Canadian Journal of Earth Sciences, 32*(6), 699–717. doi:10.1139/e95-060

Sun, T., Davis, E. E., Wang, K., & Jiang, Y. (2017a). Trench-breaching afterslip following deeper coseismic slip of the 2012 Mw 7.6 Costa Rica earthquake constrained by near-trench pressure and land-based geodetic observations. *Earth and Planetary Science Letters, 479*, 263–272. doi:10.1016/j.epsl.2017.09.021

Sun, T., Wang, K., Fujiwara, T., Kodaira, S., & He, J. (2017b). Large fault slip peaking at trench in the 2011 Tohoku-oki earthquake. *Nature Communications, 8*, 14044. doi:10.1038/ncomms14044

Sun, T., Wang, K., & He, J. (2018). Crustal Deformation Following Great Subduction Earthquakes Controlled by Earthquake Size and Mantle Rheology. *Journal of Geophysical Research: Solid Earth, 123*(6), 5323–5345. doi:10.1029/2017JB015242

ten Brink, U. S., Miller, N. C., Andrews, B. D., Brothers, D. S., & Haeussler, P. J. (2018). Deformation of the Pacific/North America Plate Boundary Queen Charlotte Fault: The Possible Role of Rheology. *Journal of Geophysical Research: Solid Earth, 123*(5), 4223–4242. doi:10.1002/2017JB014770

Tréhu, A. M., Scheidhauer, M., Rohr, K. M., Tikoff, B., Walton, M. A., Gulick, S. P., & Roland, E. C. (2015). An Abrupt Transition in the Mechanical Response of the Upper Crust to Transpression along the Queen Charlotte Fault. *Bulletin of the Seismological Society of America, 105*(2B), 1114–1128. doi:10.1785/0120140159

Wang, K., & He, J. (2008). Effects of frictional behaviour and geometry of subduction. *Bulletin of the Seismological Society of America, 98*(2), 571–579. doi:10.1785/0120070097

Wang, K., He, J., Schulzeck, F., Hyndman, R. D., & Riedel, M. (2015). Thermal Condition of the 27 October 2012 Mw 7.8 Haida Gwaii Subduction Earthquake at the Obliquely Convergent Queen Charlotte Margin. *Bulletin of the Seismological Society of America, 105*(2B), 1290–1300. doi:10.1785/0120140183

Wang, K., Sun, T., Brown, L., Hino, R., Tomita, F., Kido, M., Iinuma, T., Kodaira, S., & Fujiwara, T. (2018). Learning from crustal deformation associated with the M9 2011

Tohoku-oki earthquake. *Geosphere, 14*(2), 552–571. doi:10.1130/GES01531.1

Wang, K., & Tréhu, A. M. (2016). Invited review paper: Some outstanding issues in the study of great megathrust earthquakes—The Cascadia example. *Journal of Geodynamics, 98*, 1–18. doi:10.1016/j.jog.2016.03.010

Wang, K., Wells, R., Mazzotti, S., Hyndman, R. D., & Sagiya, T. (2003). A revised dislocation model of interseismic deformation of the Cascadia subduction zone. *Journal of Geophysical Research: Solid Earth, 108*(B1), 1–13. doi:10.1029/2001JB001227

Wang, P.-L., Engelhart, S. E., Wang, K., Hawkes, A. D., Horton, B. P., Nelson, A. R., & Witter, R. C. (2013). Heterogeneous rupture in the great Cascadia earthquake of 1700 inferred from coastal subsidence estimates. *Journal of Geophysical Research: Solid Earth, 118*(5), 2460–2473. doi:10.1002/jgrb.50101

Wessel, P., & Smith, W. H. (1998). New, Improved Version of Generic Mapping Tools Released. *EOS, Transactions, American Geophysical Union, 79*(47), 579. doi:10.1029/98EO00426

Witter, R. C., Zhang, Y. J., Wang, K., Priest, G. R., Goldfinger, C., Stimely, L., English, J. T., & Ferro, P. A. (2013). Simulated tsunami inundation for a range of Cascadia megathrust earthquake scenarios at Bandon, Oregon, USA. *Geosphere, 9*(6), 1783–1803. doi:10.1130/GES00899.1

Witter, R. C., Zhang, Y. J., Wang, K., Goldfinger, C., & Priest, G. R. (2012). Coseismic slip on the southern Cascadia megathrust implied by tsunami deposits in an Oregon lake and earthquake-triggered marine turbidites. *Journal of Geophysical Research: Solid Earth, 117*, B10303. doi:10.1029/2012JB009404

Witter, R. C., Zhang, Y., Wang, K., Priest, G. R., Goldfinger, C., Stimely, L. L., English, J. T., & Ferro, P. A. (2011). Simulating Tsunami Inundation at Bandon, Coos County, Oregon, Using Hypothetical Cascadia and Alaska Earthquake Scenarios. *Oregon Department of Geology and Mineral Industries Special Paper 43, 117*(B10), 57 p. doi:10.1029/2012JB009404

Yamazaki, Y., Cheung, K. F., & Kowalik, Z. (2011). Depth-integrated, non-hydrostatic model with grid nesting for tsunami generation, propagation, and run-up. *International Journal for Numerical Methods in Fluids, 67(*12), 2081–2107. doi:10.1002/fld.2485

Yamazaki, Y., Kowalik, Z., & Cheung, K. F. (2009). Depth-integrated, non-hydrostatic model for wave breaking and run-up. *International Journal for Numerical Methods in Fluids, 61*(5), 473–497. doi:10.1002/fld.1952

Yorath, C. J., Clowes, R. M., MacDonald, R. D., Spencer, C., Davis, E. E., Hyndman, R. D., Rohr, K., Sweeney, J. F., Currie, R. G., Halpenny, J. F., & Seemann, D. A. (1988). Marine Multichannel Seismic Reflection, Gravity and Magnetic Profiles: Vancouver Island Continental Margin and Juan de Fuca Ridge. *Geological Survey of Canada, Open File 1661*, 26 p. doi:10.4095/122447

Appendix

The stress drop, $\Delta\sigma$, experienced over a fault surface during a megathrust earthquake provides important details on the fault rupture mechanics. Here I will compare the $\Delta\sigma$ results of the Cascadia, Winona and Haida Gwaii models as well as for 11 well-studied megathrust events (Table A.1; Figure A.1). Ten of these events were studied by Sun et al. (2018) for the post-seismic deformation, which helped verify coseismic slip distribution. The slab surface geometry used in these ten models is from Sun et al. (2017a; 2018). For all of the models, except Tohoku-oki, the geometry correction described in section 2.2 has not been done. The correction would not affect the $\Delta\sigma$ calculation results because slip tapers to zero or a negligible amount before reaching the updip limit.

Average stress drop is not always defined in the same manner for every earthquake. There are four main methods for determining $\overline{\Delta\sigma}$ of an earthquake. First, the simplest way to calculate $\overline{\Delta\sigma}$ is to average $\Delta\sigma$ over the entire fault, which results in a low $\overline{\Delta\sigma}$ due to the region with a negigible amount of slip undergoing stress increase on average. Secondly, many studies simply calculate $\overline{\Delta\sigma}$ within a slip contour that defines the main rupture region. Thirdly, $\overline{\Delta\sigma}$ can be found by averaging $\Delta\sigma$ with slip distribution with a uniform $\Delta\sigma$ as a weighting function (Madariaga, 1979). Fourthly, $\overline{\Delta\sigma}$ can be calculated by averaging $\Delta\sigma$ with the actual final slip at each point on the fault as the weighting function (Noda et al., 2013). For our global comparison I find $\overline{\Delta\sigma}$ with the second unweighted method and define the main rupture area to be the region within the 10% of peak slip contour.

Average stress drop of these 11 studied events fall within the range of a few MPa (Table A.1), however there are many other slip distributions calculated by groups for these earthquakes

that could range in slip complexity. With smooth bell-shaped patches as seen in many of these discussed models, the method of calculating $\overline{\Delta\sigma}$ within 10% of peak slip generally finds a well representative average value, however for more complex slip distributions such as for the slip distribution used for the *Mw* 8.6 2005 Nias model, areas of high and/or low slip could be localized within the 10% of peak slip contour.

Table A.1. Average stress for well-constrained known megathrust earthquakes.

Event	*Mw*	Slip distribution source	Peak Slip (m)	Average stress drop within 10% of peak slip contour (MPa)[#]
2011 Tohoku	9.0	Iinuma et al. (2012); Sun et al. (2018)	~50	2.3±1.3*
1960 Chile	9.5	Moreno et al. (2011)	42.6	3.75
1964 Alaska	9.2	Sun et al. (2018)	25.0	1.95
2010 Maule	8.8	Moreno et al. (2012)	15.7	1.53
2005 Nias	8.6	Konca et al. (2007)	17.9	1.59
2001 Peru	8.4	Sun et al. (2018)	9.0	1.53
2003 Tokachi	8.1	Sun et al. (2018)	6.0	1.25
2007 Pisco	8.0	Remy et al. (2016)	9.3	1.55
1995 Antofagasta	8.0	Sun et al. (2018)	5.0	1.19
1995 Jalisco	8.0	Sun et al. (2018)	4.9	1.44
2012 Costa Rica	7.6	Sun et al. (2017a)	6.1	0.95

*Average stress drop from Brown et al. (2015).
[#] Shear modulus used in stress drop calculation is 40 GPa.

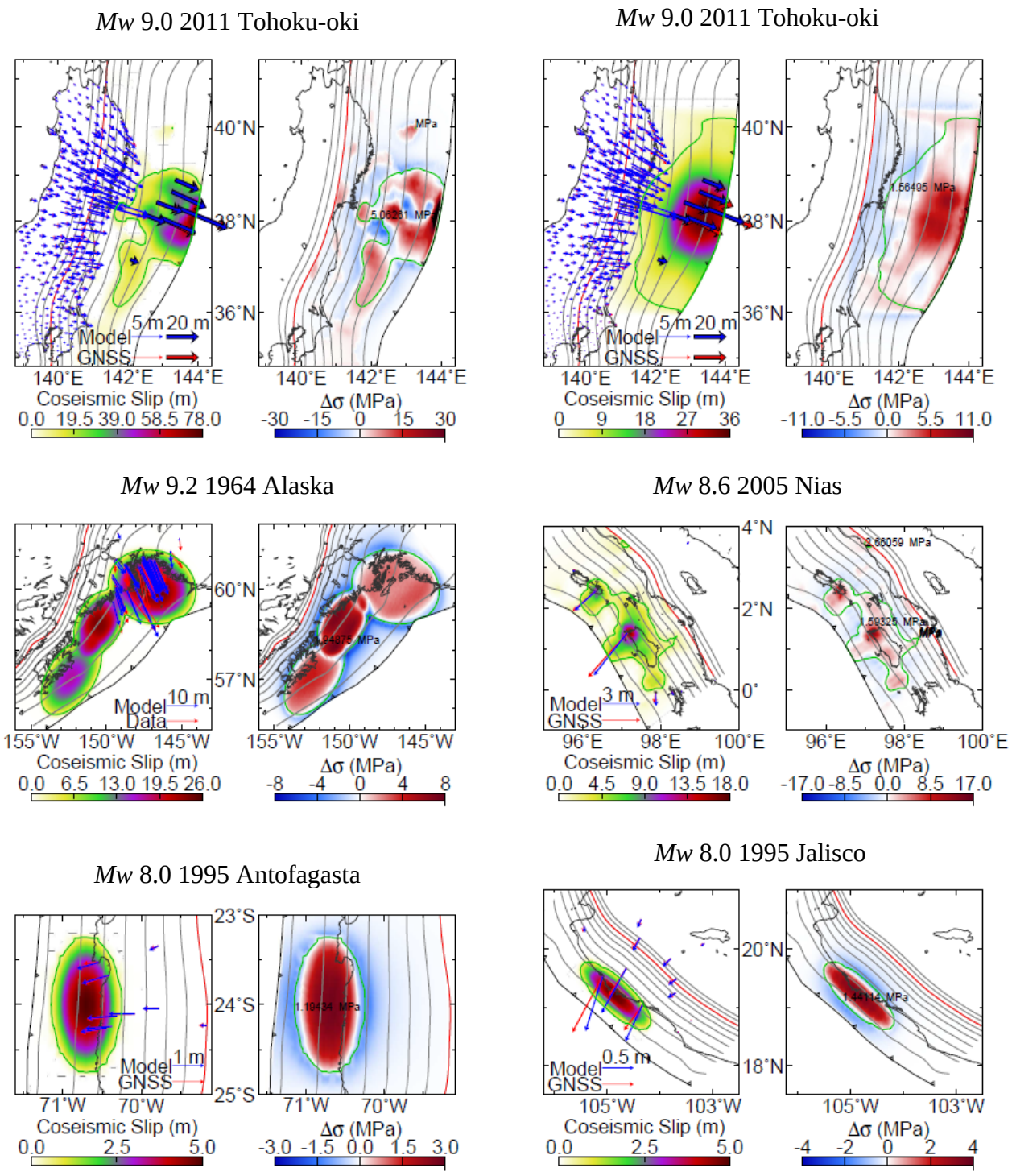

Figure A.1. Stress drop results from recent megathrust earthquakes that have a well-constrained slip distribution.

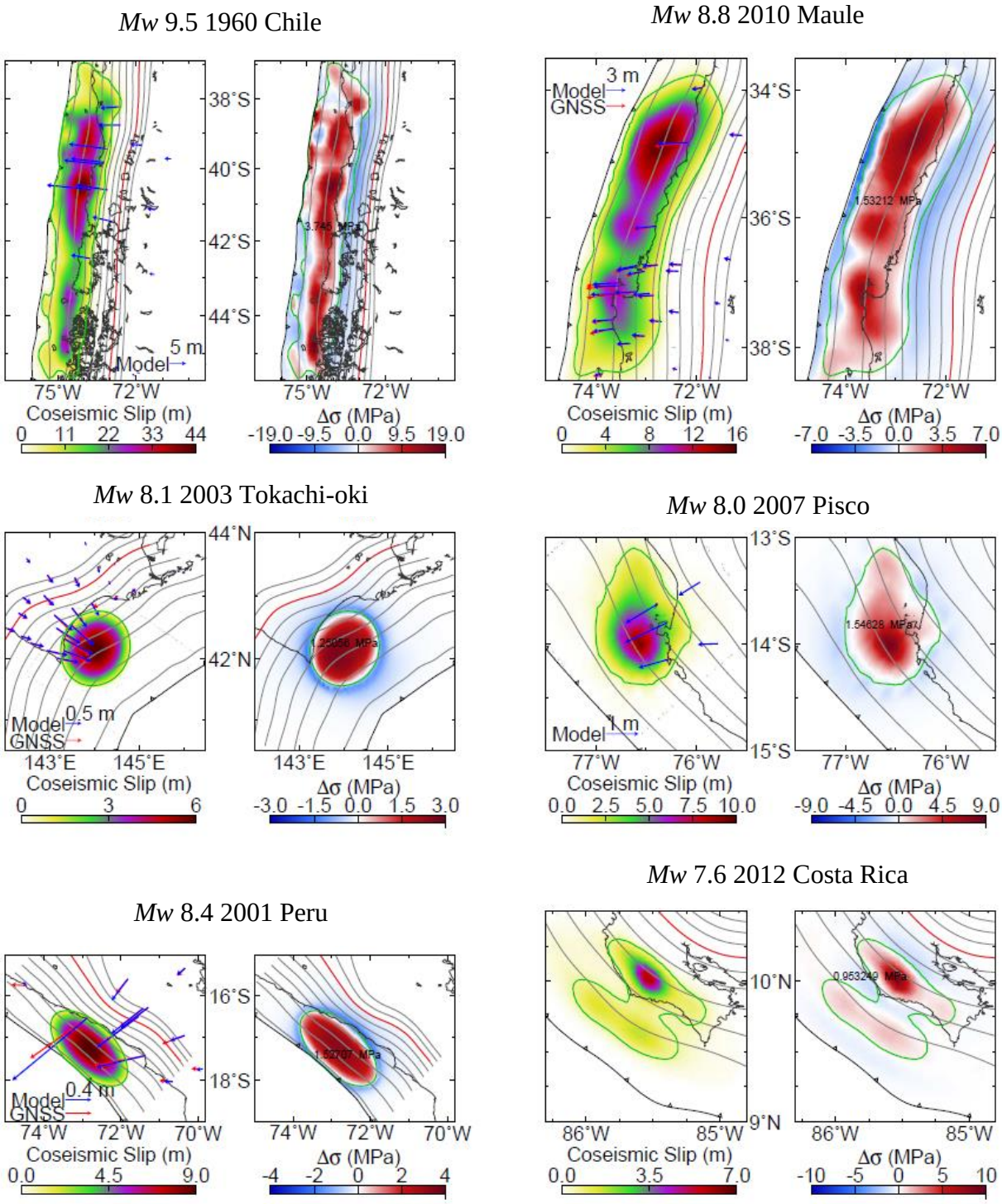

Figure A.1. Continued.